Julius Frederik Rauh, BSc.

Improvement of an Ejector for an SOFC Application using CFD

Master's Thesis

to achieve the university degree of

Diplom-Ingenieur

Master's degree programme: Mechanical Engineering

submitted to

Graz University of Technology

University Supervisor

Assoc.Prof. Dipl.-Ing. Dr.techn. Wolfgang Sanz
Institute of Thermal Turbomachinery and Machine Dynamics

Company Supervisor AVL List GmbH

Dipl.-Ing. Nikolaus Soukup

Graz, Dezember 2018

Institute of Thermal Turbomachinery and Machine Dynamics
Head: Univ.-Prof. Dr.-Ing. Franz Heitmeir

Eidesstattliche Erklärung

Ich erkläre an Eides statt, dass ich die vorliegende Arbeit selbstständig verfasst, andere als die angegebenen Quellen/Hilfsmittel nicht benutzt, und die den benutzten Quellen wörtlich und inhaltlich entnommenen Stellen als solche kenntlich gemacht habe.

Statutory Declaration

I declare that I have authored this thesis independently, that I have not used other than the declared sources/resources, and that I have explicitly indicated all material which has been quoted either literally or by content from the sources used.

Kurzfassung

Die in dieser Arbeit betrachtete Festoxidbrennstoffzelle (SOFC) wird mit Erdgas betrieben und verwendet eine externe Dampfreformierung, um einen Teil davon vor der Brennstoffzelle in Wasserstoff und Kohlenmonoxid umzuwandeln. Um eine externe Dampferzeugung zu vermeiden und den Brennstoffausnutzungsgrad zu erhöhen, wird das Anodenabgas rezirkuliert. Für diesen Kreislauf wird aktuell ein Gebläse verwendet, dessen Einsatz jedoch mit mehreren Nachteilen verbunden ist. Das Gebläse weist einen relativ geringen Wirkungsgrad auf, benötigt regelmäßige Wartungsintervalle und ist aufgrund der anspruchsvollen Betriebsbedingungen mit hohen Herstellungskosten verbunden. Es ist daher das Ziel dieser Arbeit zu evaluieren, ob das Gebläse durch einen Ejektor, ein robustes, günstiges und wartungsarmes Bauteil, ersetzt werden kann.

Die Leistung von Ejektoren wird mit dem Entrainment Ratio und dem Saugdruck gemessen, die voneinander abhängig sind. Diese Werte werden für eine gegebene Geometrie und definierte Eingangsgrößen anhand von CFD-Simulationen in AVL Fire^{TM} bestimmt. Dafür wird eine der beiden Größen konstant gehalten, während die andere berechnet wird. Nach einer experimentellen Validation der CFD-Simulationen wurde der Einfluss verschiedener Parameter auf diese Leistungsparameter evaluiert. Verluste in einzelnen Abschnitten wurden anhand der Änderung des Totaldruckes bewertet.

Die Auswertungen zeigten einen stark positiven Einfluss bei Erhöhung der Primärgastemperatur und des Primärdruckes auf die Leistung des Ejektors. Mit den gegebenen Einschränkungen für diese Werte konnte aber auch nach der Geometrieoptimierung der geforderte Betriebspunkt nicht erreicht werden. Eine mögliche Alternative sind aber noch Betriebspunkte bei geringeren Entrainment Ratios. Bei diesen reduziert sich auch der Druckverlust im Anodenpfad und dadurch der benötigte Saugdruck. Anhand dieser Arbeit ist es mit geringem Aufwand möglich, für so einen alternativen Betriebspunkt die optimale Ejektorgeometrie zu finden, da der Einfluss aller Parameter evaluiert wurde und der Aufwand der CFD-Simulationen durch ein im Zuge dieser Arbeit erstelltes Preprocessing-Tool in MATLAB stark reduziert wurde.

Abstract

The solid-oxide fuel cell (SOFC) by AVL discussed in this work is powered by natural gas and uses external steam reforming to produce hydrogen and carbon monoxide for the fuel cell. To avoid the energy losses of an external steam production, the anode off-gas is recirculated. Currently, this stream is transported by a blower that has a low efficiency, requires regular maintenance and is high in manufacturing costs. The goal of this work is to evaluate if an ejector, a relatively cheap and robust low-maintenance component, can replace the blower.

The performance of an ejector is measured by its entrainment ratio and suction pressure, which are dependent on each other. They are found for a given set of input parameters by CFD simulations in AVL Fire$^{\text{TM}}$. This is done by setting one of the performance parameters and calculating the other one. After validating the simulation setup, the influence of geometric and thermodynamic input parameter on the ejector performance was evaluated. Losses in various sections of the ejector were evaluated by a total pressure analysis.

The final results showed a positive influence of the primary pressure and temperature on the ejector performance. Considering the restrictions for these parameters, the optimized ejector still could not reach the necessary performance for the desired operating point. But lower entrainment ratios than required for the initial operation point are able to avoid carbon deposition in the reformer. For these alternative operating points, the required suction pressure is also reduced, as the total volume flow through the SOFC is lower. This thesis enables a fast evaluation of different operating points, as the influence of each parameter is now known. Additionally, the simulation effort was vastly reduced through the generation of a preprocessing tool written in MATLAB.

Contents

List of Figures

List of Tables

Symbols and Abbreviations

Latin Symbols

a	m/s^2	Acceleration
a	m/s	Sonic velocity
A	m^2	Area, surface, crosssection
c	m/s	Sonic velocity
c_p	J/(kg K)	Mass specific heat capacity for $p =$ const.
c_v	J/(kg K)	Mass specific heat capacity for $v =$ const.
$C_{\mathrm{m}p}$	J/(mol K)	Molar heat capacity for $p =$ konst.
$C_{\mathrm{m}v}$	J/(mol K)	Molar heat capacity for $v =$ konst.
d	m	Diameter
e	J/kg	Specific internal energy
$\hat{e}$	J/kg	Specific total energy
$\vec{f}_n$	m	Face normal vector
F	N	Force
h	J/kg	Mass specific enthalpy
H	J	Enthalpy
H_m	J/mol	Molar enthalpy
l	m	Length
m	kg	Mass
$\dot{m}$	kg/s	Mass flow
M	kg/mol	Molar mass
M	−	Mach number (=$\|v\|/a$)
n	mol	Amount of substance
$\dot{n}$	mol/s	Substance per time
p	bar	Pressure
Δp	bar	Suction pressure
p_i	bar	Partial pressure
P	W	Power
q	J/kg	Specific heat
$\dot{q}$	W/kg	Specific heat flux
Q	J	Heat
R	m	Radius
R	J/(kg K)	Specific gas constant

Re	–	Reynolds number ($= c \cdot l/\nu$)
s	J/(kg K)	Mass specific entropy
S	J/K	Entropy
S_{m}	J/(mol K)	Molar entropy
t	mm	Carbon layer thickness
t	s	Time
T	K	Temperature
v	m/s	Velocity
V	m^3	Volume
$\dot{V}$	m^3/s	Volume flow
w	J/kg	Specific work
W	J	Work
x	m	Coordinate

Greek Symbols

α	°	Mach cone angle
β_D	-	Diameter ratio
β_P	-	Pressure ratio
γ	–	Heat capacity ratio
η	–	Efficiency
η_{N}	–	Nozzle efficiency
η_{D}	–	Diffuser efficiency
μ_{i}	–	Mass fraction of component i
ν_{i}	–	Molar fraction of component i
ρ	$\mathrm{kg/m^3}$	Density
ω	–	Entrainment ratio

Constants

e	2.7183	–	Euler's number
π	3.1416	–	Archimedes' constant
R_{m}	8314.5	J/(kmol K)	Molar gas constant

Indices and Abbreviations

0	Stagnation condition, ejector inlet
1	Nozzle exit
2	Mixing chamber inlet
3	Diffuser inlet
4	Diffuser exit
AGR	Anode gas recirculation
b	Back
BC	Boundary condition
c	Critical
C	Carbon
CAD	Computer aided design
CFD	Computational fluid dynamics
CHP	Combined heat and power
CPU	Central processing unit
CR	Compression ratio
e	Exit
ER	Entrainment ratio
g	Arbitrary gas composition
i	Inner
(l)	Liquid
m	Molar, mixed flow
max	Maximum
min	Minimum
MC	Mixing chamber
NIST	National Institut of Standards and Technology
NE	Nozzle exit
NT	Nozzle throat
o	Outer
OP	Outlet pipe
p	Primary flow
PEM	Polymer electrolyte membrane
r	Radial coordinate
RR	Recirculation ratio
RNG	Re-normalization group
rev	Reversible
s	Secondary flow
s	Isentropic
SC	Suction chamber
Sim	Simulation
SOFC	Solid oxide fuel cell
SST	Shear stress transport
STCR	Steam to carbon ratio
TVD	Total variation diminishing

Operators

d	Total differential
δ	Functional differential
∂	Partial differential
$\int$	Integral
$\sum$	Sum
Δ	Difference

SI-Prefixes

G	10^9	Giga
M	10^6	Mega
k	10^3	Kilo
c	10^{-2}	Centi
m	10^{-3}	Milli
μ	10^{-6}	Micro

1 Introduction

Fuel cell systems provide a low-emission way to supply electricity at the highest efficiencies. If the fuel cell produces useful heat at the same time, it is a combined heat and power (CHP) system. Fuel cells are usually characterized by their electrolyte material, which defines some of its key properties. The solid-oxide fuel cell (SOFC) has the advantage that it can use multiple kinds of fuel because its high operating temperature enables the use of reforming processes to convert normally unusable types of fuel into usable ones. In the case of the AVL SOFC CHP system, a steam reforming process prior to the fuel cell is used to convert natural gas and steam into hydrogen, carbon monoxide and carbon dioxide. On the anode of the stack the hydrogen and carbon monoxide are converted into steam and carbon dioxide in a chemical reaction that enables the fuel cell to produce electric energy.

To avoid the energy losses of an external steam production, it is desirable to use the anode off-gas of the fuel cell as a steam source for the reformer. A common problem in this process is the deposition of carbon on the reformer surface in the form of graphite, which reduces the reactive area until the catalyst is fully deactivated. The amount of carbon which is deposited depends on the thermodynamic equilibrium of the anode off-gas and the natural gas in the reformer. This means that for each operating point of the fuel cell the amount of anode off-gas that has to recirculated to avoid carbon deposition is different.

1.1 Initial situation

Currently, the AVL SOFC CHP system uses a blower to move the recirculation stream, but this system has multiple disadvantages. The blower uses electric power, provided by the SOFC, at a low efficiency, lowering the total electric efficiency of the fuel cell. Because of the highly corrosive nature of the steam and hydrogen atmosphere, and the high temperatures, common engineering materials can not be used, resulting in high manufacturing costs [4] [10]. The blower also needs to be cooled, which requires a cooling stream that needs additional regular maintenance and increases the complexity of the system. An ejector pump in comparison is relatively cheap to manufacture, has no movable parts and requires no maintenance.

At AVL, a first design of an ejector for this SOFC system was created within the thesis of M. Rossi [31] and its performance simulated with computational fluid dynamics (CFD). Subsequently, the thesis of D. Bischof [3] tried to validate the CFD results of Rossi with a prototype on a testing rig. As the simulation results did not agree with the empirical results, M. Tkaucic tried to further improve the simulation setup in his thesis [26] and found better agreement with the empirical results. M. Schwager improved the simulation setup again and investigated the influence of parameter changes on the ejector performance in a fourth thesis [32]. In his final results Schwager found an ejector geometry that could satisfy the requirements set by the Fuel Cell Department at an alternative operating point. However, further research concluded that the amount of recirculated anode off-gas is too low at this alternative operating point to avoid carbon deposition, making it invalid to use.

1.2 Task formulation

The goal of this thesis is to either find an ejector geometry that reaches the required performance or prove that no ejector geometry exists that can satisfy them. To disprove the existence of a functioning ejector geometry for a certain operating point, the key parameters that influence the ejector performance have to be found and their significance on the overall performance has to be understood. Only when each parameter is at an optimum and the overall pressure increase provided by the ejector is still lower than required, an ejector solution can be excluded.

The performance of the ejector is measured by the amount of pressure increase at the outlet at a given entrainment ratio or vice versa. The influence of certain parameters on this performance has to be found through CFD simulations with the AVL Fire$^{\text{TM}}$ software.

Previous CFD simulations done with ejectors went through multiple changes in the geometry, mesh generation technique and computational settings to increase the quality of the results and reduce calculation time. The latest computational settings and techniques used for mesh generation have to be validated by the testbed results of D. Bischof [3].

As the thermodynamic state variables at the primary and secondary input are also modifiable through the use of heat exchangers and compressors, their influence on the ejector performance and their achievable upper thresholds have to be found to define clear boundary conditions in the simulations.

There is also concern that carbon deposition might clog the thin ejector nozzle. An assessment of whether carbon deposition occurs at a critical rate, at the prevalent conditions inside the nozzle, is therefore required.

1.3 The stationary AVL SOFC CHP system

A basic flow sheet of the AVL SOFC CHP system can be seen in fig. 1.1. Air (blue) enters (1), is preheated by a heat exchanger (2) and enters the cathode side of the fuel cell stack (3). Here the oxygen atoms take on two electrons each and travel through the electrolyte to the anode (6). The rest of the air combines with fresh air and the anode off-gas (4) and then performs a catalytic combustion in the afterburner, also known as oxicat (5). The hot exhaust gas (yellow) then travels through the heat exchanger (2) and the pre-reformer (10), before being used for cogenerative purposes (e.g. heating water in a heat exchanger) in (7).

In (8) the natural gas (red) enters, is mixed with part of the anode off-gas and enters the blower (9). The gas mixture then travels through the pre-reformer (10), where it undergoes a steam reforming process. Here part of the methane and steam is transformed to carbon monoxide, hydrogen and carbon dioxide. In (11) the gas mixture is preheated by the anode off-gas before entering the anode of the fuel cell stack (6). Here the carbon monoxide and the hydrogen react with the oxygen anions to form carbon dioxide and steam. As described before, part of the anode off-gas is then mixed with air and processed in the oxicat (5).

When the blower (9) is exchanged by an ejector, the energy required for its performance is no longer provided by electricity which drives a motor, but by an increased pressure level of the natural gas. For this reason an external compressor which increases the pressure of the natural gas is necessary in an ejector application. The anode flow path for such a case is shown in fig. 1.2. Here the natural gas enters (1) and its pressure is increased in a compressor (2). The high pressure natural gas and the recirculated anode off-gas are combined in the ejector (3) before entering the pre-reformer (4). The gas mixture is then preheated (5) before entering the anode side of the SOFC. In (7) the anode off-gas that is not recirculated moves on to the oxicat as described previously. For more information on the AVL SOFC CHP system, see the thesis of D. Bischof [3] and M. Schwager [32].

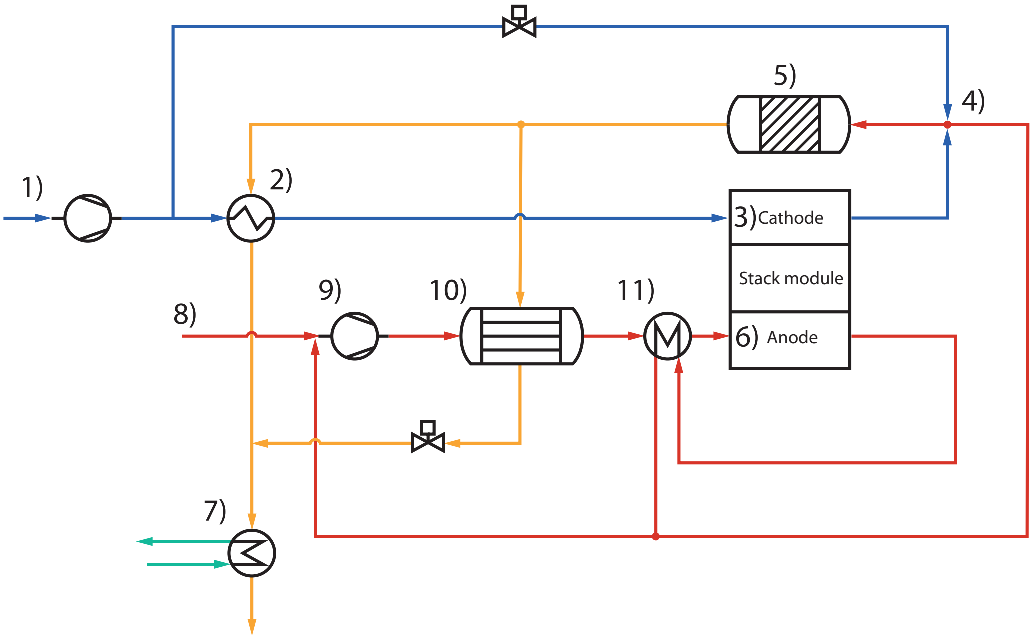

Figure 1.1: Simplified flow sheet of the AVL SOFC system.

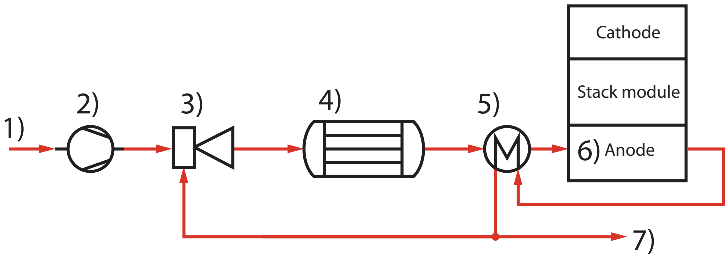

Figure 1.2: Anode flow path of the AVL SOFC system with an ejector instead of a blower.

2 Fundamentals

In this chapter the most important basic concepts of fuel cells, gas dynamics and gas ejectors are discussed.

2.1 Fuel cells

To produce electrical energy with a combustion engine, the chemical energy first has to be converted to heat energy, then mechanical energy and finally to electrical energy in a generator. Going through all these steps is complex and inefficient. Fuel cells are superior in this regard, as they convert the chemical energy of a fuel to electrical energy without these additional steps. [28]

To give a better understanding of the fuel cell process, the combustion of hydrogen is used as an example:

$$H_2 + \frac{1}{2} O_2 \rightleftharpoons H_2O \tag{2.1}$$

In this reaction hydrogen-hydrogen bonds and oxygen-oxygen bonds are broken while hydrogen-oxygen bonds are formed. The bonds are broken and formed by the transport of electrons, as the electrons want to move to a lower energy state (see fig. 2.2). In this case the potential energy of the hydrogen-oxygen bonds is lower than that of the initial hydrogen and oxygen gases. To harness the electrons moving from one state to another as electrical current, the reactants have to be spatially separated, so that the bonding reconfiguration occurs over a greatly extended length scale. [28]

2.1.1 Principle of the SOFC

The solid-oxide fuel cell (SOFC) can not only use hydrogen but also carbon monoxide in a redox reaction to produce electricity. In each case, the reaction is separated

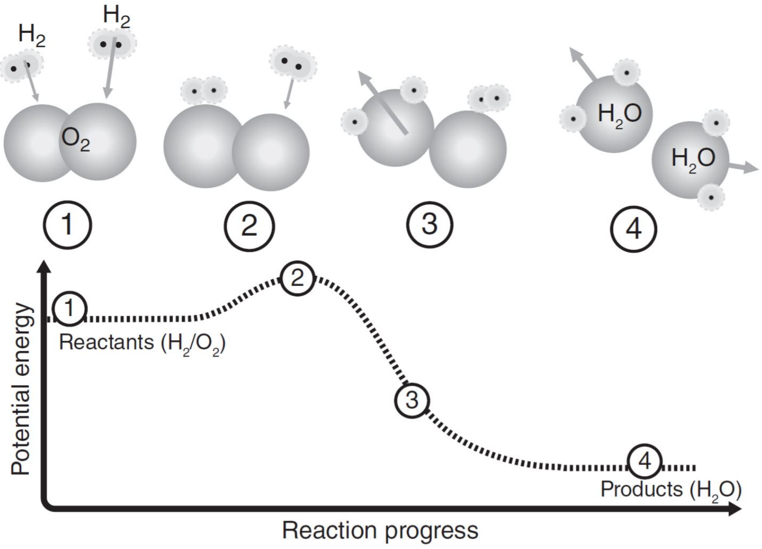

Figure 2.1: The H_2-O_2 combustion reaction. Hydrogen and oxygen bonds (1) must first be broken, requiring the activation energy (2), before the hydrogen-oxygen bonds are formed at a lower energy state, releasing energy (3, 4). Figure taken from p. 4 in [28].

into two half reactions:

$$\frac{1}{2}O_2 + 2e^- \rightleftharpoons O^{2-} \tag{2.2}$$

$$H_2 + O^{2-} \rightleftharpoons H_2O + 2e^- \tag{2.3}$$

$$CO + O^{2-} \rightleftharpoons CO_2 + 2e^- \tag{2.4}$$

These reactions are spatially separated by a ceramic electrolyte. The electrolyte is a barrier for electrons and only lets O^{2-} ions pass, forcing the electrons to flow through an external circuit as electric current. The reduction of oxygen (eq. 2.2) occurs at the cathode, while the oxidation reactions of hydrogen (eq. 2.3) and carbon monoxide (eq. 2.4) occur at the anode of the fuel cell. (see fig. 2.2)

2.1.2 The steam reforming process

Due to the high temperatures in the SOFC it is possible to use hydrocarbons as fuel and reform them inside the stack (internal reforming) or prior in an external

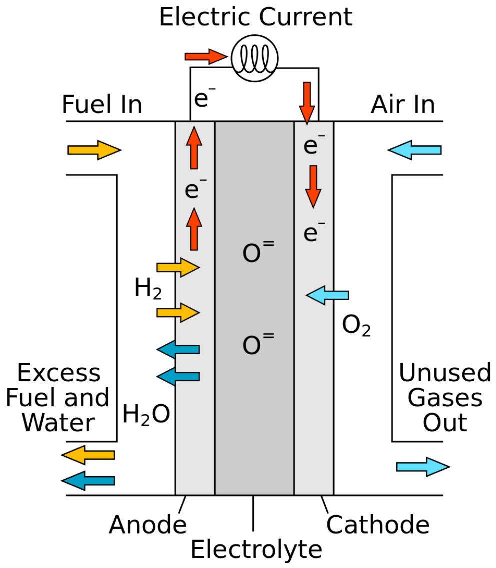

Figure 2.2: Scheme of a SOFC from [34].

gas processing unit (external reforming). While the internal reforming process reduces system complexity and the total cost by elimination of the external reformer it has major problems that make it disadvantageous. One is the problem of carbon deposition due to hydrocarbon pyrolysis (eq. 2.5), where the deposited carbon deactivates the catalyst and reduces cell performance. [33, p. 338-339]

$$C_nH_{2n+2} \rightleftharpoons nC + (n+1)\,H_2 \tag{2.5}$$

By adding steam to the fuel gas before the reforming process, this reaction can be inhibited to a certain extent and instead the steam reforming reaction occurs:

$$C_nH_{2n+2} + nH_2O \rightleftharpoons nCO + (2n+1)\,H_2 \tag{2.6}$$

Equation 2.6 is a strongly endothermic reaction (for methane $\Delta H = +206\,\mathrm{kJ/mol}$), while eq. 2.3 and eq. 2.4 are exothermic reactions. This can lead to potential instabilities when using internal reforming. The CO produced by steam reforming can produce additional hydrogen through the water gas shift reaction:

$$CO + H_2O \rightleftharpoons CO_2 + H_2 \tag{2.7}$$

This reaction is advantageous not only because it increases the amount of hydrogen but also because it inhibits another reaction that can occur with CO which leads to carbon deposition,

$$2\,CO \rightleftharpoons C + CO_2, \tag{2.8}$$

which is called the Boudouard reaction. [28]

The ratio of steam to carbon (STCR) is an important variable when designing a reformer. In steam reforming catalysis it is usually a value around $2.5 - 3.0$ [28] [38]. This is a higher amount than required by eq. 2.6 but is necessary so that the equilibrium for eq. 2.7 lies to the right so that eq. 2.5, eq. 2.8 and thus carbon deposition can be avoided. However, due to the increased complexity of the thermochemical system when using anode off-gas recirculation, the STCR is not a sufficient criterion to avoid carbon deposition. The thermodynamic equilibrium at a certain temperature in the reformer has to be calculated to avoid carbon deposition with certainty. This defines a required recirculation ratio RR or anode gas recirculation ratio

$$AGR = \frac{\dot{n}_{anode,rec}}{\dot{n}_{anode,out}}, \tag{2.9}$$

as seen in [37]. It is simply the ratio of the amount of recirculated anode off-gas $\dot{n}_{anode,rec}$ to the total amount of anode off-gas $\dot{n}_{anode,out}$ which leaves the fuel cell.

2.2 Gas dynamics

Incompressible fluid mechanics deals with pressure and kinetic energy changes which are so small that their influence on the density and temperature is negligible. This differs from gas dynamics, which is the study of compressible flow, where these changes in density and temperature have a significant influence on the flow. [29, p. 1]

In this section, the most important basic concepts and equations of compressible flow are explained. When not explicitly cited, the material follows the explanations used in *Introduction to Compressible Fluid Flow* [29] by P. Oosthuizen and *Fundamentals of Gasdynamics* [46] by R. Zucker.

2.2.1 Sonic velocity and Mach number

For compressibility effects to become relevant it is not the velocity that is important, but rather the ratio of velocity to the speed of sound. The speed of sound or sonic velocity is the velocity at which *small* disturbances travel through a medium. *Large* disturbances are able to travel faster and are called shock waves (see section 2.2.5). For an ideal gas the sonic velocity a is only dependent of the temperature T, the specific heat ratio γ and the gas constant R. [29, p. 39][46, p. 88]

$$a = \sqrt{\gamma R T} \tag{2.10}$$

As mentioned before, the ratio of the local velocity $\vec{v}$ to the speed of sound a is considered when evaluating the compressibility of a flow. This ratio is termed the Mach number M and is dimensionless.

$$M = \frac{||\vec{v}||}{a} \tag{2.11}$$

Depending on the Mach number a flow is said to be

- subsonic for $M < 1$;
- sonic or transonic for $M = 1$;
- supersonic for $M > 1$;
- hypersonic for $M > 5$. [29, p. 39][46, p. 89]

2.2.2 Mach cone

When a body moves through gas, infinitesimal pressure pulses are continually emitted. Since they are very weak, they travel through the medium at sonic velocity. Considering a body moving at a supersonic velocity u as seen in fig. 2.3 in a fixed time interval t this body moves the distance $u \cdot t$, while every disturbance propagates as a spherical wave front from its point of origin at the speed of sound a. All disturbances lie within the indicated cone, known as *Mach cone* or *Mach wave* which has its vertex at the body on point d. The region inside the cone is called *zone of action*, while the region outside of it is the *zone of silence*. The vertex angle α is given as

$$\sin\alpha = \frac{a}{||u||} = \frac{1}{M}. \tag{2.12}$$

If the body is not moving and gas is flowing at supersonic velocity around it, the same Mach cone can be observed. In this case the cone indicates when the state variables of the supersonic flow change due to the disturbance of the body. [29, p. 51-52][46, p. 89-91]

2.2.3 Conservation laws for compressible flow

The analysis of compressible flow is based on the principles of conservation of mass, momentum and energy [29, p. 10]. The basic conservation laws of continuum mechanics in differential form will be given for the special case of compressible flow of a perfect gas, where chemical changes, electric and magnetic effects, viscosity, gravity, and heat conduction are neglected.

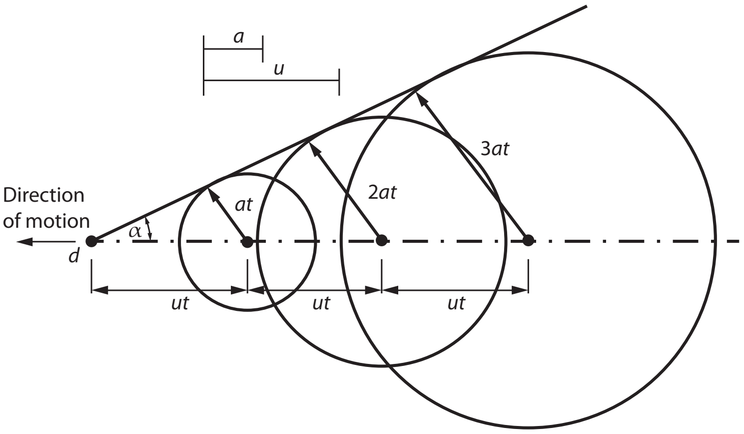

Figure 2.3: Mach cone formed by a body moving at supersonic speed u. [29, fig. 3.8]

Conservation of mass

Conservation of mass in continuum mechanics states that mass can neither be produced nor destroyed. This is shown by the continuity equation for a control volume:

$$\frac{\partial \rho}{\partial t} + \left(\vec{\nabla} \cdot \rho \vec{v}\right) = 0 \tag{2.13}$$

In words it states that the change of mass inside the control volume is equal to the net mass flow over its boundaries. [2, p. 49-55]

When considering a steady flow of velocity v through a duct of varying area A, the conservation of mass requires that

$$\rho v A = constant. \tag{2.14}$$

Conservation of momentum

Newton's second law states the conservation of momentum for a constant-mass system by the formula

$$F = m \cdot a, \tag{2.15}$$

where F is the force applied to a body, m is its mass and a the acceleration. When applying this law to the flow through a control volume, multiple different forces have to be considered, but as stated before, some of them can be neglected. Forces can be separated into body forces and surface forces, depending on their occurrence. For the body forces, forces due to gravity and forces due to electromagnetism are distinguished. Electromagnetism can be neglected, as it is only of importance in ionized gases. The forces due to gravity can also be neglected, as the inertia of the flow is much higher than gravity (=high Froude number) in compressible flow. For the surface forces, pressure forces and viscous forces are distinguished. Due to the high Reynolds numbers in compressible flows, the viscous forces can also be neglected. Forces due to pressure can not be neglected, which leaves the balance of momentum over the control volume as

$$\rho \left[\frac{\partial \vec{v}}{\partial t} + \left(\vec{v} \cdot \vec{\nabla} \right) \vec{v} \right] = -\vec{\nabla} p. \tag{2.16}$$

This states that the temporal change of the total momentum must be equal to the pressure forces. [2, p. 60-66]

Conservation of energy

The first law of thermodynamics states that energy can neither be produced nor destroyed. This also has to be true for any flow of energy over the boundaries of a control volume. As in section 2.2.3, the influence of gravity, body forces and viscous forces is neglected. Additionally, energy transport due to heat conduction is ignored. Considering this, the *total* mass specific energy

$$e_0 = e + \frac{\vec{v}^2}{2} \tag{2.17}$$

of any fluid element is the sum of two different kinds of energy: the internal energy e due to random molecular motion and the kinetic energy $\frac{\vec{v}^2}{2}$ due to translational motion. The temporal change of this total energy inside the control volume has to be equal to the rate of work done by pressure forces and energy transferred as heat flux:

$$\rho \frac{d}{dt} \left(e_0 \right) = - \left(\vec{\nabla} \cdot p\vec{v} \right) + \rho \dot{q} \tag{2.18}$$

By neglecting conductive heat transfer, the heat flux is only represented through volumetric heating $\dot{q}$ such as absorption and emission of radiation. [2, p. 66-74]

A different form of eq. 2.18 is found by introducing the enthalpy

$$dh = de + d \left(\frac{p}{\rho} \right). \tag{2.19}$$

With eq. 2.19 and eq. 2.13, eq. 2.18 can be transformed to

$$\rho \frac{dh}{dt} = \frac{dp}{dt} + \rho \dot{q}. \tag{2.20}$$

By introducing the *total* enthalpy as

$$h_0 = h + \frac{\vec{v}^2}{2} = e + \frac{p}{\rho} + \frac{\vec{v}^2}{2} = e_0 + \frac{p}{\rho} \tag{2.21}$$

eq. 2.20 is transformed to

$$\rho\frac{dh_0}{dt} = \frac{dp}{dt} + \rho\dot{q}. \tag{2.22}$$

In a stationary, adiabatic flow where viscosity and body forces can be neglected, eq. 2.22 requires that

$$h_0 = constant. \tag{2.23}$$

This results in the following equation for a streamline from point 1 to 2:

$$c_p T_1 + \frac{\vec{v}_1^2}{2} = c_p T_2 + \frac{\vec{v}_2^2}{2} \tag{2.24}$$

2.2.4 State variables at stagnation

When decelerating a flow isentropically until its velocity is zero, the state variables are said to be at *stagnation* condition or at their *total* value. The energy equation as written in eq. 2.24 for this case is

$$c_p T_1 + \frac{\vec{v}_1^2}{2} = c_p T_0 \tag{2.25}$$

where the state at "0" is in stagnation. This equation can be transformed to a form where the stagnation temperature is only a function of the Mach number. First, eq. 2.25 is rewritten as

$$\frac{T_0}{T_1} = 1 + \frac{v^2}{c_p 2 T_1}. \tag{2.26}$$

By substituting $c_p = \frac{\gamma}{\gamma-1}R$ and then $a = \sqrt{\gamma R T_1}$ in eq. 2.26, the Mach number $M = \frac{||v||}{a}$ can be substituted:

$$\frac{T_0}{T_1} = 1 + (\gamma - 1)\frac{v^2}{2\gamma R T_1} = 1 + (\gamma - 1)\frac{v^2}{2a^2} = 1 + \frac{\gamma - 1}{2}M^2 \tag{2.27}$$

The state with index "1" can be any state, which gives the final form for the ratio of stagnation temperature to the temperature at any state:

$$\frac{T_0}{T} = 1 + \frac{\gamma - 1}{2}M^2 \tag{2.28}$$

Using the isentropic relations

$$\frac{T_2}{T_1} = \left(\frac{p_2}{p_1}\right)^{\frac{\gamma-1}{\gamma}} = \left(\frac{\rho_2}{\rho_1}\right)^{\gamma-1} \tag{2.29}$$

eq. 2.28 can be rewritten for pressure and density:

$$\frac{p_0}{p} = \left(1 + \frac{\gamma-1}{2}M^2\right)^{\frac{\gamma}{\gamma-1}} \tag{2.30}$$

$$\frac{\rho_0}{\rho} = \left(1 + \frac{\gamma-1}{2}M^2\right)^{\frac{1}{\gamma-1}} \tag{2.31}$$

2.2.5 Shock waves

When a fluid or an object moves at supersonic speed, *finite* pressure disturbances are frequently encountered. Even though they incorporate large changes in fluid properties, the thickness over which these changes occur is so small that they appear as discontinuities in the flow and are called *shock waves*. The shock wave can stand still relative to its surrounding or be moving through a medium. If it is moving, the area ahead of it is termed *upstream* and the area behind it *downstream*. If it is a standing wave, the supersonic flow moving towards the shock wave is upstream and the flow moving away from it is downstream. If the shape of the shock wave is straight (i.e. not curved) and it is at a right angle to the upstream flow, it is called a *normal shock wave*. If it were at an angle to the upstream it would be termed an *oblique shock wave* (see fig. 2.4). [29, p. 87]

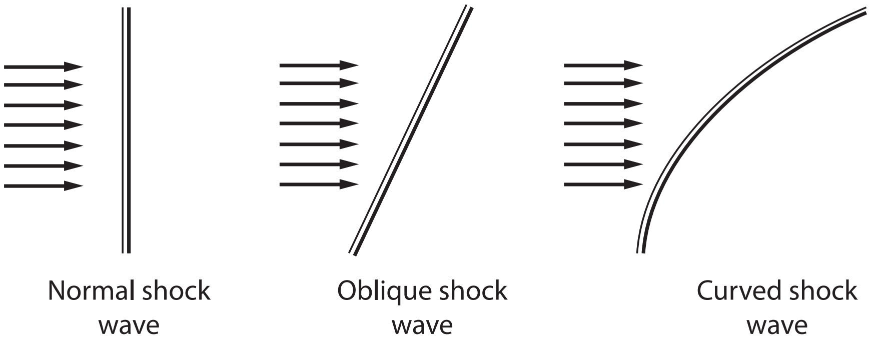

Figure 2.4: A normal, oblique and curved shock wave. [29, fig. 5.4]

Applying the conservation equations from section 2.2.3 on a control volume around a standing normal shock wave, as seen in fig. 2.5, the Hugoniot normal

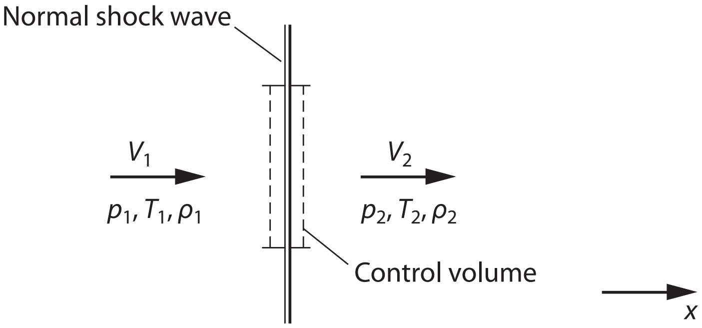

Figure 2.5: Control volume around a standing shock wave. [29, fig. 5.4]

shock wave relations can be obtained:

$$\frac{\rho_2}{\rho_1} = \frac{\left[\left(\frac{\gamma+1}{\gamma-1}\right)\frac{p_2}{p_1} + 1\right]}{\left[\left(\frac{\gamma+1}{\gamma-1}\right) + \frac{p_2}{p_1}\right]} \tag{2.32}$$

$$\frac{V_1}{V_2} = \frac{\left[\left(\frac{\gamma+1}{\gamma-1}\right)\frac{p_2}{p_1} + 1\right]}{\left[\left(\frac{\gamma+1}{\gamma-1}\right) + \frac{p_2}{p_1}\right]} \tag{2.33}$$

$$\frac{T_2}{T_1} = \frac{\left[\left(\frac{\gamma+1}{\gamma-1}\right) + \frac{p_2}{p_1}\right]}{\left[\left(\frac{\gamma+1}{\gamma-1}\right) + \frac{p_1}{p_2}\right]} \tag{2.34}$$

This set of equations gives relations of state variables before and after the shock wave in terms of the strength of the shock wave $\frac{p_2}{p_1}$. To discern whether a shock wave is compressive ($\frac{p_2}{p_1} > 1$) or expansive ($\frac{p_2}{p_1} < 1$), the entropy change over the shock wave

$$s_2 - s_1 = c_p \ln\left(\frac{T_2}{T_1}\right) - R\ln\left(\frac{p_2}{p_1}\right) \tag{2.35}$$

is observed. Rewriting eq. 2.35 as a function of $\frac{p_2}{p_1}$ gives

$$\frac{s_2 - s_1}{R} = \ln\left\{\left(\frac{p_2}{p_1}\right)^{\frac{1}{\gamma-1}}\left[\frac{(\gamma+1)\frac{p_2}{p_1} + (\gamma+1)}{(\gamma+1) + (\gamma-1)\frac{p_2}{p_1}}\right]^{\frac{-\gamma}{\gamma-1}}\right\}. \tag{2.36}$$

The second law of thermodynamics requires that

$$\frac{s_2 - s_1}{R} \geq 0 \tag{2.37}$$

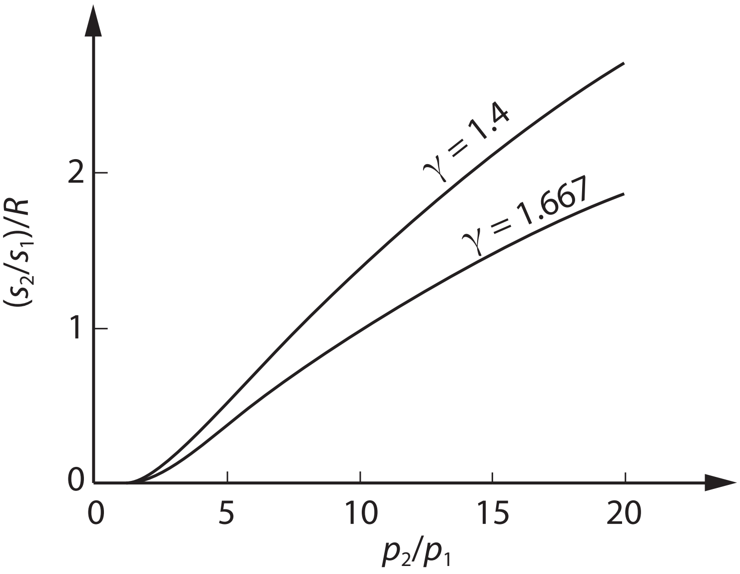

Figure 2.6: Relation between entropy change and pressure ratio across a normal shock wave. [29, fig. 5.10]

which gives the relation shown in fig. 2.6. As can be seen from this, a shock wave must always be compressive ($\frac{p_2}{p_1} > 1$) and is, opposed to a weak wave, highly irreversible. Even though the stagnation temperature T_0 does not change across the shock wave, the stagnation pressure p_0 always has to decrease.

It is often more convenient to have the relations $\frac{\rho_2}{\rho_1}, \frac{p_2}{p_1}, \frac{T_2}{T_1}$ and also the downstream Mach number M_2 in terms of the upstream Mach number M_1:

$$\frac{p_2}{p_1} = \frac{2\gamma M_1^2 - (\gamma - 1)}{(\gamma + 1)} \tag{2.38}$$

$$\frac{\rho_2}{\rho_1} = \frac{(\gamma + 1) M_1^2}{2 + (\gamma - 1) M_1^2} \tag{2.39}$$

$$\frac{T_2}{T_1} = \frac{\left[2\gamma M_1^2 - (\gamma - 1)\right]\left[2 + (\gamma - 1) M_1^2\right]}{(\gamma + 1)^2 M_1^2} \tag{2.40}$$

$$M_2^2 = \frac{M_1^2 + \frac{2}{\gamma - 1}}{\frac{2\gamma}{\gamma - 1} M_1^2 - 1} \tag{2.41}$$

2.2.6 Flow through a convergent nozzle

When considering an isentropic flow through a duct of varying area, the conservation of mass in eq. 2.14, energy in eq. 2.24 and the isentropic relations in eq. 2.29

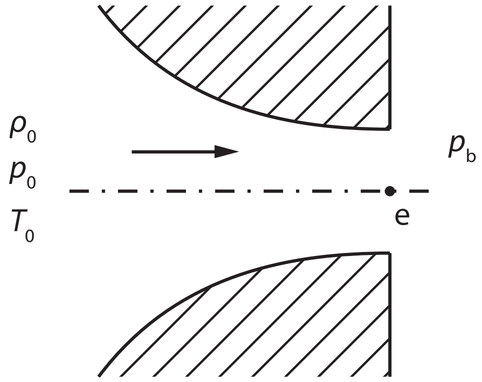

Figure 2.7: Converging nozzle with fixed inlet conditions ρ_0, p_0, T_0 and varying back pressure p_b. (recreation of [29, fig. 8.8])

give the relation between the area and the pressure between two points 1 and 2:

$$\frac{A_2}{A_1} = \left(\frac{p_1}{p_2}\right)^{\frac{1}{\gamma}} \left[\frac{1-\left(\frac{p_1}{p_0}\right)^{\frac{\gamma-1}{\gamma}}}{1-\left(\frac{p_2}{p_0}\right)^{\frac{\gamma-1}{\gamma}}}\right]^{\frac{1}{2}} \tag{2.42}$$

The stagnation pressure p_0 in eq. 2.42 has to be calculated from eq. 2.30.

For the converging nozzle shown in fig. 2.7, flow on the left hand side starts from a reservoir where it is in stagnation condition. On the exit of the nozzle the *back pressure* p_b can be varied. The lower the ratio of $\frac{p_b}{p_0}$ is, the higher the mass flow through the nozzle, until the ratio reaches the *critical* value at

$$\frac{p_e}{p_0} = \frac{p*}{p_0} = \left(\frac{2}{\gamma+1}\right)^{\frac{\gamma}{\gamma-1}} . \tag{2.43}$$

At this point the flow at the exit reaches $M = 1$ and the mass flow no longer increases. The pressure p_e at the exit of the nozzle remains at this critical value $p*$ even if p_b is lowered further. The flow through the nozzle at this condition is said to be *choked*. At values of $p_b < p*$, the flow is termed *underexpanded* and the remaining pressure difference results in shock structure, whose shape depends on the degree of underexpansion [8]. An example for a highly-underexpanded flow is shown in fig. 2.8. Here a barrel shock structure, a series of axisymmetric curved shocks due to the merging of expansion waves, is formed [41].

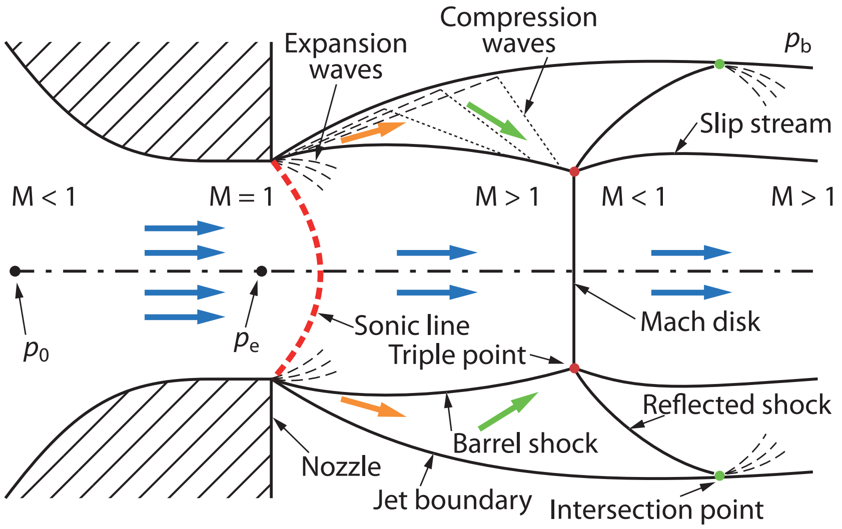

Figure 2.8: Example for a barrel shock structure in a highly-underexpanded jet. Orange arrows show outward expansion, green arrows show inward compression and blue arrows show parallel flow. [41]

2.2.7 De Laval nozzle

The de Laval nozzle is a convergent-divergent nozzle, as seen in fig. 2.9, which enables it to expand a high pressure gas to supersonic conditions. The relation between area ratio and pressure ratio in eq. 2.42 can also be rewritten as a function of the Mach number:

$$\frac{A_2}{A_1} = \left(\frac{M_1}{M_2}\right) \left\{ \frac{1 + \left(\frac{\gamma-1}{2}\right) M_2^2}{1 + \left(\frac{\gamma-1}{2}\right) M_1^2} \right\}^{\frac{\gamma+1}{2(\gamma-1)}} \tag{2.44}$$

If instead of integrating the energy conservation equation the differential form is used, then instead of eq. 2.44 the following equation is obtained:

$$\frac{dA}{A} = \frac{\left(M^2 - 1\right)}{1 + \left(\frac{\gamma-1}{2}\right) M^2} \frac{dM}{M} \tag{2.45}$$

Here the influence of a change in area ratio depending on the current Mach number can be seen. If $M < 1$ the numerator $\left(M^2 - 1\right)$ in eq. 2.45 is negative, so dM has the opposite sign of dA. In this case a decrease in area induces an increase in the Mach number. If $M > 1$, the opposite is true and the Mach number only increases if the area increases too.

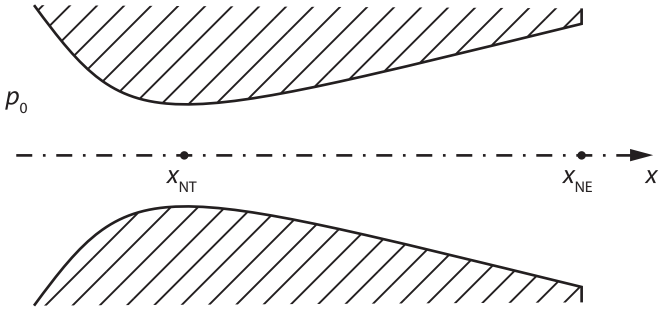

Figure 2.9: Schematic of a de Laval nozzle with the throat area section at x_{NT} and the nozzle exit at x_{NE}.

In fig. 2.10, the Mach number throughout the nozzle, depending on the back pressure at the exit plane p_e, is shown. Multiple distinct cases can be observed for $p_e < p_0$.

- $p_0 > p_e > p_1$: The flow does not reach $M = 1$ in the throat and is thus fully subsonic. It can be considered isentropic, as no shocks occur.
- $p_e = p_1$: In this borderline case the flow reaches sonic conditions in the throat, but decelerates to subsonic conditions in the diverging section.
- $p_1 > p_e > p_2$: The flow reaches sonic conditions in the throat and accelerates further in the diverging section, until a normal shock inside the nozzle decelerates the flow to subsonic conditions.
- $p_e = p_2$: In this borderline case the flow decompresses to the design pressure p_3, but gets compressed by a normal shock at the nozzle exit.
- $p_2 > p_e > p_3$: At an exit pressure lower than p_2 the shock can no longer occur at the nozzle exit. The flow exits at supersonic conditions, but gets compressed by oblique shocks outside of the nozzle. The flow in this case is said to be *overdeveloped*. The state variables at the exit can be calculated as if the flow was isentropic, as the shocks occur outside.
- $p_e = p_3$: This is the design case of the nozzle. The static pressure of the flow at the exit is the same as in the exit chamber.
- $p_e < p_3$: If the back pressure is lower than the design pressure of the nozzle, the flow is considered *underdeveloped* and expands further after exiting the nozzle.

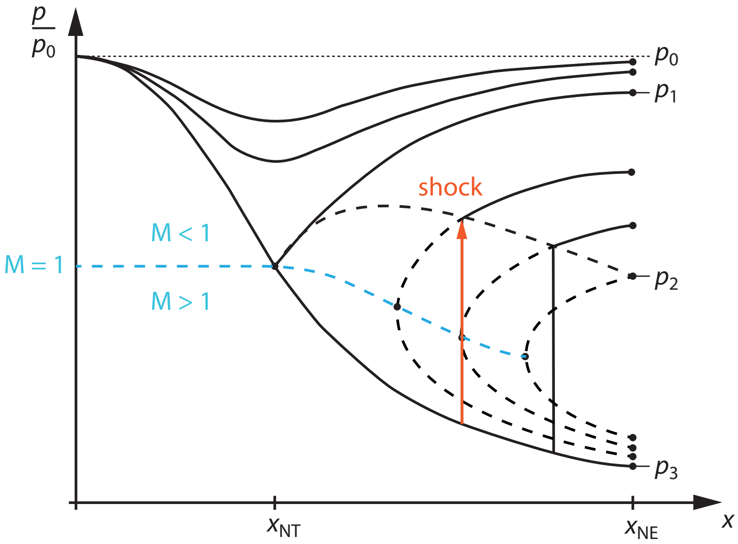

Figure 2.10: Pressure in a de Laval nozzle relative to the inlet stagnation pressure p_0 depending on the pressure on the exit plane.

2.2.8 Subsonic diffusers

Equation 2.45 states that an increase in area available to a subsonic flow results in a decrease of the Mach number, as discussed in section 2.2.7. This also leads to an increase in static pressure according to eq. 2.30 if the flow is isentropic. Components whose sole purpose is to recover static pressure by decelerating a flow are named diffusers. An ideal diffuser would be able to decelerate the flow without increasing its entropy. As any actual application has losses, diffusers won't reach the pressure calculated through isentropic relations.

An example for an actual pressure recovery in a diffuser is shown in fig. 2.11. The static pressure at the inlet of the diffuser is p_1 and its total pressure is p_{10}. An ideal diffuser would not change the total pressure, it would remain at $p_{10} = p_{20s}$. The actual diffuser increases the pressure to p_2 by also increasing the entropy and thus reducing the total pressure to p_{20}.

The efficiency with which the diffuser recovers the static pressure can be defined in multiple ways. The *total-pressure recovery factor* η_r is one possibility to define such an efficiency, and it is widely used in the propulsion industry [46, p. 133].

$$\eta_r = \frac{p_{20}}{p_{10}} \tag{2.46}$$

Another common factor is the *diffuser efficiency*, where the actual pressure rise is

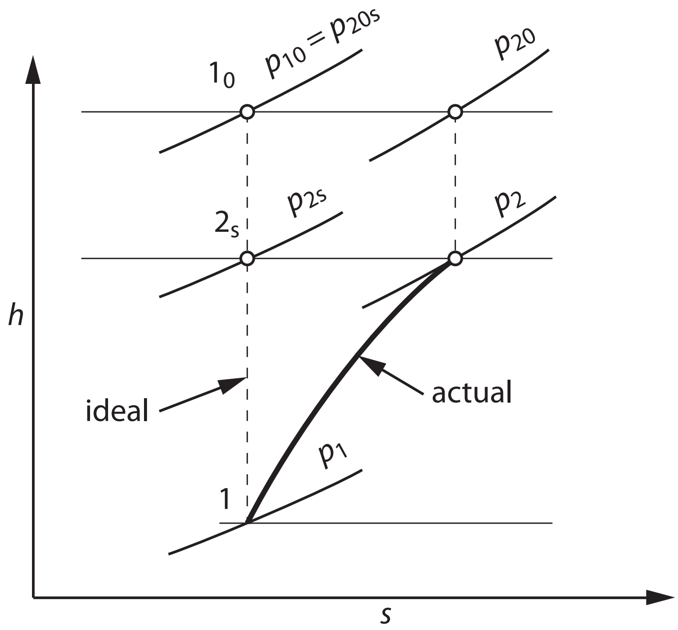

Figure 2.11: h-s diagram of an actual diffuser. [46, fig. 5.13]

put in relation to the ideal pressure rise. [46, p. 134]

$$\eta_d = \frac{p_2 - p_1}{p_{2s} - p_1} \tag{2.47}$$

2.2.9 Fanno flow

Fanno flow describes the compressible adiabatic flow through a constant-area duct where friction is considered. Friction has been neglected previously, as this is an adequate assumption in nozzles and short ducts, but when dealing with long ducts, the friction from the walls becomes relevant. The Fanno flow model is described by a set of differential equations that can be easily solved if a dimensionless friction factor is known and assumed to be constant over the length of the duct.

As seen in fig. 2.12, the Mach number along the flow path of a subsonic flow increases in a duct when friction is considered. At the same time the static pressure decreases. In a supersonic flow the reverse is true, the Mach number decreases while the static pressure increases. This is made more clear when looking at the Fanno line, which is a depiction of the flow process on a T-s diagram as shown in fig. 2.13. As is stated by the second law of thermodynamics, the entropy in a closed system can only increase. For the entropy to increase, in fig. 2.13 the temperature

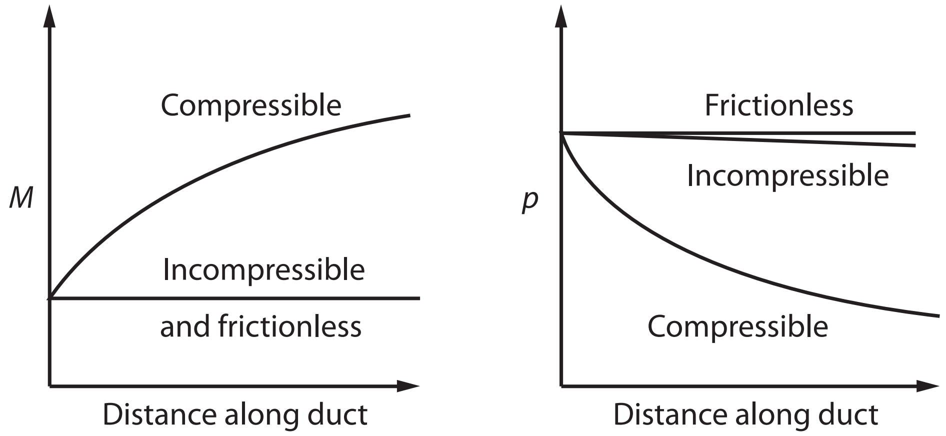

Figure 2.12: Influence of friction on the Mach number and the static pressure in a duct when considering subsonic flow. [29, fig. 9.1]

of a subsonic Fanno flow has to decrease, while it has to increase for a supersonic flow. This means that any Fanno flow eventually reaches sonic velocity. The change of the flow variables relative to their value at sonic velocity is shown in fig. 2.14.

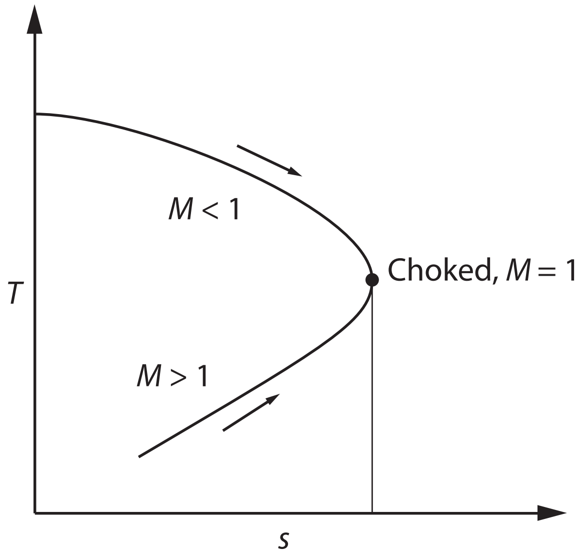

Figure 2.13: Change in temperature and entropy depending on the Mach number of the flow. The line depicted is called Fanno line. [29, fig. 9.5]

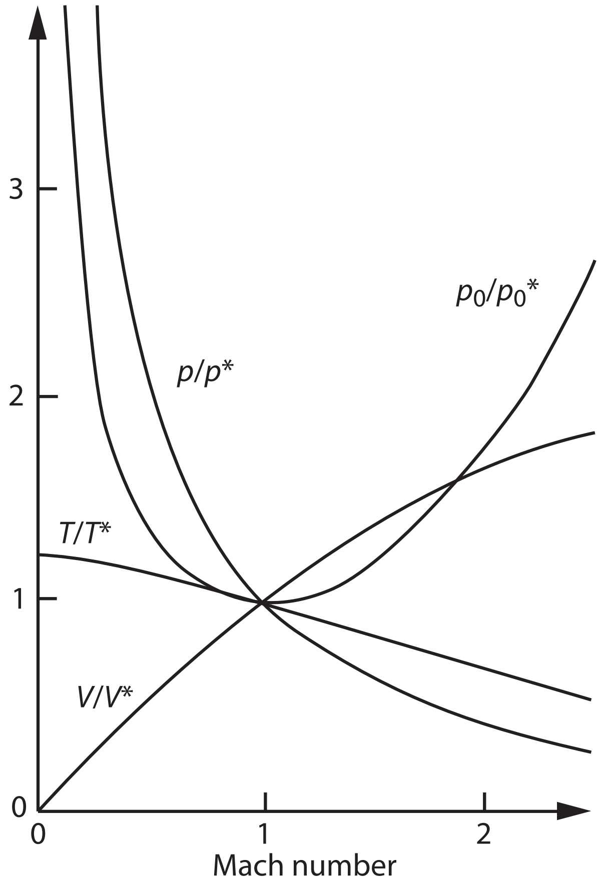

Figure 2.14: Change in state variables relative to their critical value at $M = 1$ in a fluid with $\gamma = 1.4$. [29, fig. 9.6]

2.3 Gas/gas ejectors

Ejectors, also known as jet pumps, use a high pressure primary stream to increase the pressure of a secondary stream. This is done by converting the pressure energy of the primary stream to kinetic energy through a nozzle and using this stream to entrain and accelerate the secondary flow in the same direction. When both streams are mixed, the combined stream gets re-compressed in a diffuser to reach a higher pressure level than the secondary flow has at the inlet. [35]

Ejectors were originally developed to replace pumps for the boilers of steam engines by H. Giffard in 1858 [20]. In his work the motive flow was high pressure steam that entrained cold water, making it a liquid/gas ejector. In this work only ejectors that use gases as primary and secondary fluids, gas/gas ejectors, are discussed.

2.3.1 Geometry and notation

A schematic of an ejector can be seen in fig. 2.15. The high pressure *primary stream* or *motive stream* enters the primary pipe (0) and accelerates in the converging section of the nozzle until it reaches sonic flow at the throat (T). In supersonic ejector nozzles the stream gets further depressurized in a diverging nozzle section to increase the velocity of the stream (1). The *secondary stream* or *entrained stream* enters the secondary pipe (0) and joins the primary flow in the suction chamber (1). Here the secondary flow gets accelerated by the high velocity primary stream and they enter the mixing chamber (2). In the mixing chamber the two streams mix, resulting in a chemically homogeneous stream with a fully developed velocity profile (3). In the diffuser the mixed flow decelerates and its static pressure increases before entering the outlet pipe (4).

2.3.2 Performance parameters

The performance of an ejector is quantified by two parameters, the entrainment ratio and the compression ratio. The entrainment ratio ω is the ratio of the entrained secondary flow to the primary mass flow:

$$\omega = \frac{\dot{m}_s}{\dot{m}_p} \tag{2.48}$$

The compression ratio describes the increase in pressure by dividing the static pressure of the mixed stream after the diffuser P_4 by the static pressure of the secondary

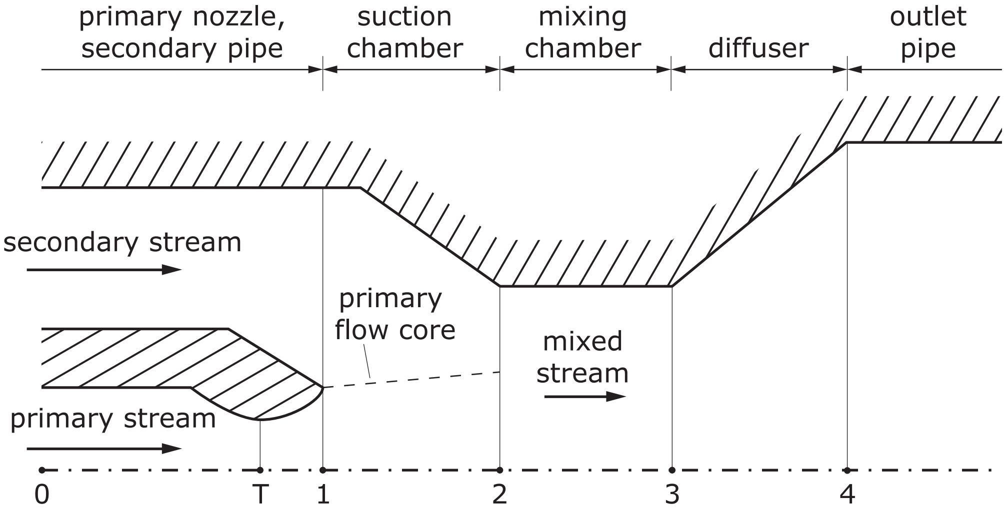

Figure 2.15: Schematic diagram of a constant-pressure ejector.

flow at the inlet P_{s0}:

$$CR = \frac{P_4}{P_{s0}} \tag{2.49}$$

Instead of the compression ratio the *suction pressure*

$$\Delta p = P_4 - P_{s0} \tag{2.50}$$

is also commonly used. A higher entrainment ratio lowers the amount of suction pressure that can be achieved.

2.3.3 Types of ejectors

Ejectors are commonly classified in two categories depending on the nozzle position relative to the mixing chamber. If the primary nozzle exit is at the beginning or inside of the mixing chamber, the mixing of the two streams occurs in a constant-area section and the ejector is known as a *constant-area ejector* (shown in fig. 2.16). If the nozzle exit is located before the mixing chamber exit in the suction chamber, the mixing is assumed to occur at constant static pressure and the ejector is thus referred to as a *constant-pressure ejector* (shown in fig. 2.15) [17]. In literature the constant-pressure ejector is widely regarded as the superior design with better performance [16] [17] [19] [22, p. 141]. C. Liao found in his parametric study that the constant area ejector might have superior performance for certain operating conditions, but this prediction was not tested in an experiment [22, p. 74].

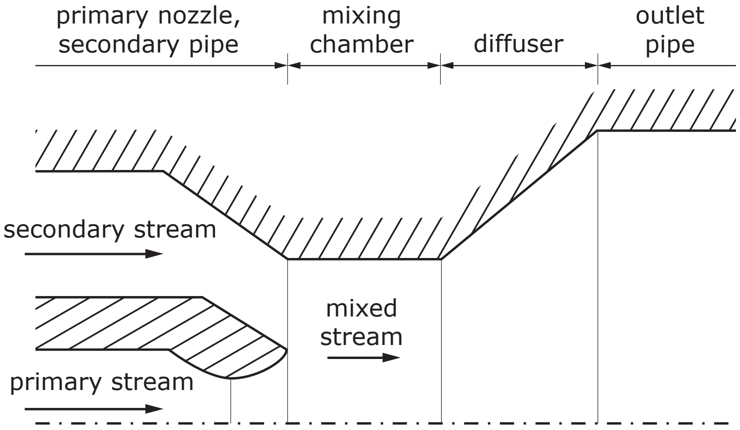

Figure 2.16: Schematic diagram of a constant-area ejector.

Not all ejectors use a converging-diverging nozzle. If a supersonic nozzle is used depends on the medium and the primary pressure available. In ejectors that are deployed in PEMFC applications for example, subsonic nozzles are used to prevent freezing of water due to the temperature drop, and to reduce sound and physical wear [7].

In ejectors that are developed for low entrainment ratios and high compression ratios, the pressure in the suction chamber is commonly lower than the secondary inlet pressure to accelerate the primary flow further. This is achieved by a converging secondary flow path (the secondary nozzle), where the secondary flow gets accelerated and thus depressurized before entering the suction chamber at almost $M = 1$. In the suction chamber both streams combine to a mixed supersonic stream, which decelerates through a shock in the mixing chamber before entering the diffuser at subsonic condition. [14] [16] [17]

2.3.4 Operating modes

When using an ejector at a fixed suction pressure, three distinct operational modes can be seen by increasing the primary pressure as shown in fig. 2.17. At a primary pressure lower than the exit pressure p_e the ejector operates in *back flow mode*. The increased primary pressure increases the primary mass flow, but the kinetic energy of the primary stream in this case is not enough to overcome the pressure difference between the outlet and secondary inlet. At a primary pressure above p_e, the secondary stream becomes entrained and reaches the static pressure at the outlet.

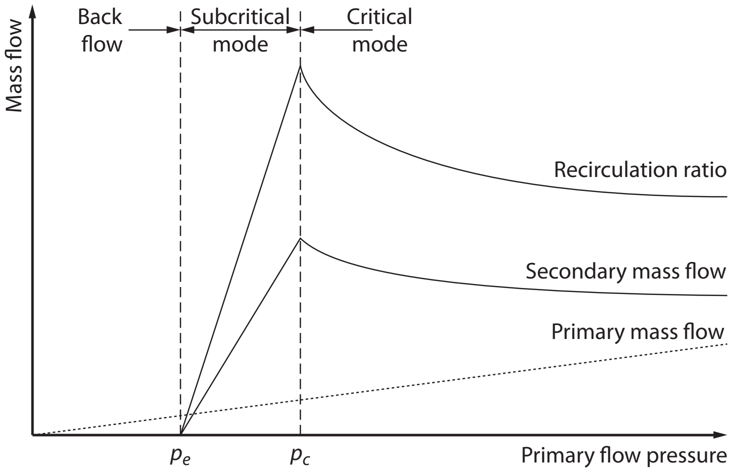

Figure 2.17: Operating modes of ejectors depending on the primary pressure. [10, fig. 1]

With increasing primary pressure the amount of entrained secondary flow in this *subcritical mode* increases together with the primary flow until the critical primary pressure p_c is reached. At this critical point the highest secondary mass flow and entrainment ratio are reached [10]. Any increase of the primary pressure above this value reduces the secondary mass flow and the entrainment ratio. The secondary flow in this case is often described as *choked* even if it does not reach $M = 1$, because it reaches almost constant values at higher primary pressures [7].

2.3.5 Literature on ejector design models

The first 1-D model for ejector design was published by Keenan and Neumann in 1950. They developed the constant-area and constant-pressure mixing models for gas/gas ejectors where they use one-dimensional continuity, momentum and energy equations to find an optimal pressure compression ratio for a given entrainment ratio. In this model based on ideal gas dynamics they required the primary and secondary stream to have the same molecular weight and specific heat ratio. They also neglected diffuser and nozzle efficiencies and frictional effects. It should be noted that the ejectors used for validation in this paper use entrainment ratios lower than 0.15. [19]

It is often mentioned that the 1-D model of Keenan and Neumann is not very accurate and produces higher performance values than experimental results. Its advantage is however that it avoids the use of experimentally determined constants.

[22, p. 6] [35]

Liao remarks in his doctoral thesis that Keenan and Neumann expressed their opinion that the constant-area model agreed with experimental results, but that it was difficult to obtain an agreement between the theoretical and experimental results for the constant-pressure ejector flow model. He goes on to note that the ideal constant-pressure design model should provide information on the flow channel, but that it was impossible to determine a general optimal shape, as a different operating point would require a different shape. In his opinion it is not practical to design a gas ejector with the constant-pressure mixing model. [22, p. 74-75]

In 1958 Fabri and Sienstruck showed in Schlieren photographs that the primary stream emerging from the nozzle remains an identifiable stream for some distance downstream [11]. Munday and Bagster postulated in 1977 that the primary stream emerging from the nozzle fans out, which acts as a converging duct for the secondary stream [27]. This effect has been called the *aerodynamic throat* [22] or *hypothetical throat* [14] [17].

In 1999 Huang et al. developed a 1-D ejector model that uses the hypothetical throat to design ejectors at critical operation mode. In his model the geometry is that of a constant-pressure ejector, but he assumes that the unmixed primary stream extends into the mixing chamber, where constant-pressure mixing starts. His model uses isentropic efficiency ratios that scale the nozzle and mixing chamber, and loss coefficients that account for losses in the nozzle and the mixing of the two streams. To evaluate these coefficients, experimental results are needed. This 1-D model was only validated for relatively low entrainment ratios ($\omega < 0.5$). [16]

Liao developed a generalized 1-D model in 2008 that shows the relationship between constant-pressure and constant-area 1-D models. His model is very complex compared to other 1-D models and not easily applicable. His model also uses efficiency coefficients for the nozzle and diffuser that have to be determined by experiments. [22]

All of the models discussed up to this point assumed a constant velocity of the secondary stream in the choked condition. This is not valid for ejectors with large entrainment ratios, as the high secondary volume stream results in a non-uniform velocity distribution. While the inside of the secondary stream reaches a high velocity during the mixing, the velocity quickly reduces further away from the center. A non-uniform velocity distribution was first suggested by Y. Zhu in [44] and further adapted in [45] for ejectors in SOFC applications. The ejector development approach by Zhu is discussed in more detail in section 5.2.

In summary, the 1-D design models of ejectors have not changed considerably since the first model was introduced by Keenan [19]. They all rely on efficiency or loss coefficients obtained by simulation or testbed results to predict the ejector performance at a given operating point. The main difference between them is in how they attempt to find the optimal diameter of the mixing chamber d_{MC}. While the early models do not try to optimize d_{MC}, later models attempt to find the optimal value by calculating the secondary flow in a choked condition at the mixing chamber inlet. As has been shown by Zhu in [44], this is not valid for ejectors with a high entrainment ratio.

3 General ejector analysis

In the beginning of this chapter the problem of carbon deposition and an evaluation of its threat is presented. Next some basic calculations are performed that are necessary to define the boundary and input values for the CFD simulations. In the end of this chapter the performance of an ideal ejector is computed using traditional 1-D ejector design methods.

3.1 Carbon deposition in the primary nozzle

Concerns were raised on the clogging of the nozzle when high temperature natural gas is used. The decomposition of hydrocarbons could lead to a blocked nozzle due to carbon formation in the throat area of the nozzle. The steel currently used for the nozzle is 1.4841, a high nickel alloy steel ($\approx 20\%$ mass as seen in [39]). This could be problematic, as nickel is a catalyst for the cracking of methane [42]. It can not be assumed that a thin layer of carbon would deactivate the Ni working as a catalyst, as Ni diffuses to the surface in carbon formation reactions [18]. It has to be kept in mind that a catalyst does not change the point of equilibrium, it only speeds up the rate at which equilibrium is attained (p.210 in [30]).

For an evaluation of the threat of carbon deposition, it is assumed that the natural gas reaches a thermodynamic equilibrium before the throat area, and all C-Atoms deposit on the throat. Using the online equilibrium calculator of the University of Colorado [6], the equilibrium for the natural gas mix of Graz (see table 3.1) is calculated for various temperatures and pressures.

As seen in fig. 3.1, the mass fractions of C-atoms decrease with an increase of pressure, as is expected by Le Chatelier's principle [30, p. 210]. Furthermore, higher temperature increases the amount of C-atoms drastically. At primary temperature levels below 800 K, the amount of C-Atoms is lower than the lowest possible output of the equilibrium calculator.

To evaluate the danger of nozzle clogging, a worst case scenario for carbon deposition is calculated. The total mass of C after 20 years of operation at a constant

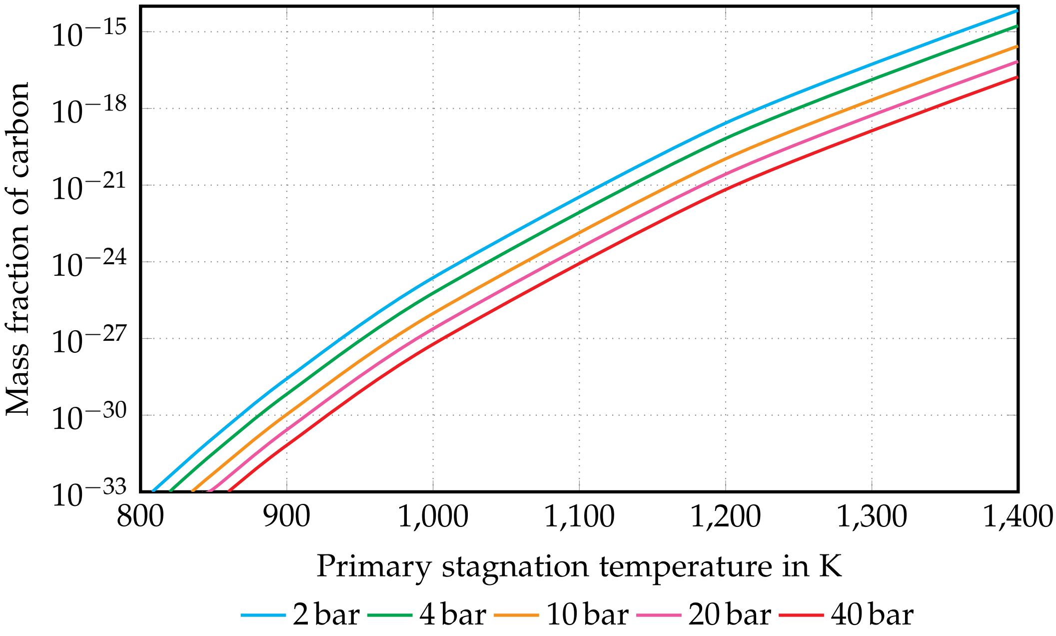

Figure 3.1: Mass fraction of Carbon in natural gas at thermodynamic equilibrium.

mass flow rate of $\dot{m} = 0.2\,\mathrm{g/s}$ depends on the carbon mass fraction μ_C.

$$m_C = \mu_C\,\dot{m} \cdot 60 \cdot 60 \cdot 24 \cdot 365 \cdot 20 \tag{3.1}$$

With the density of graphite at $\rho_C = 220\,\mathrm{kg/m^3}$, the total volume of the deposited carbon V_C is then given by

$$V_C = m_C \cdot \rho_C. \tag{3.2}$$

It is assumed that the total amount of C is deposited as graphite in a pipe of $D = 0.5\,\mathrm{mm}$ diameter and $L = 1\,\mathrm{mm}$ length. The resulting thickness t of the carbon layer can be seen in fig. 3.2 and is calculated by

$$t = \frac{D - \sqrt{D^2 - \frac{4\,V_C}{L\,\pi}}}{2}. \tag{3.3}$$

In this worst case scenario, the total deposition of carbon is negligible below mass fractions of $\mu_C = 10^{-19}$, which corresponds at low primary pressure to a maximum primary temperature of $\sim 1\,200\,\mathrm{K}$ according to fig. 3.1. This temperature is higher than any primary temperature used in the simulations and higher than any heat source available in the SOFC, which could be used to heat up the primary flow. Additionally the throat is the location of high velocities and low local temperature, making a problematic rate of deposition unlikely even at higher temperatures.

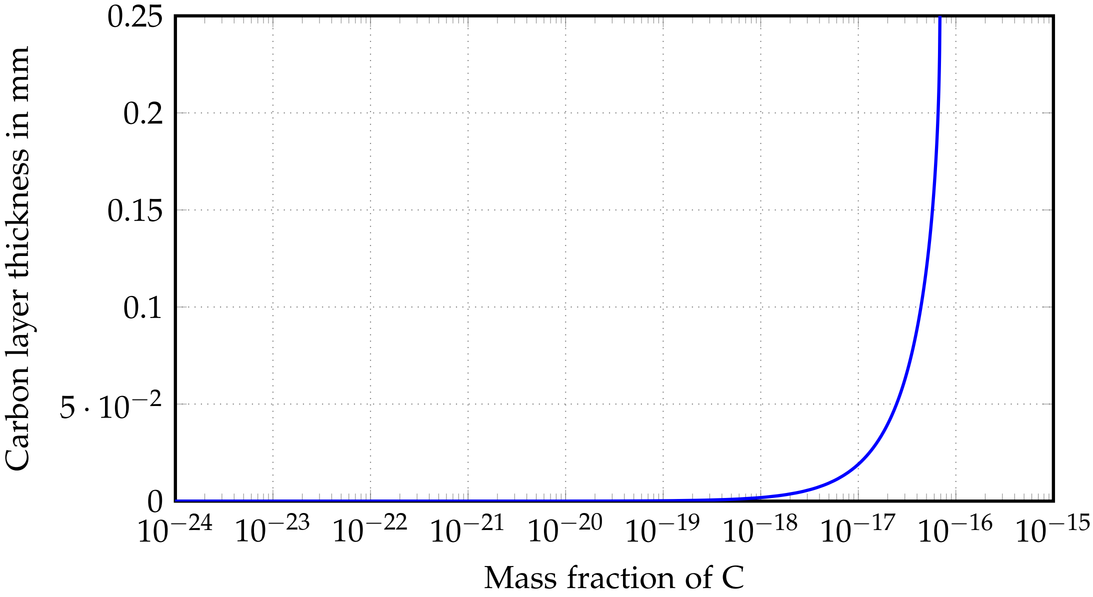

Figure 3.2: Carbon layer thickness at a mass flow of 0.2 g/s after 20 years, assuming all carbon deposits in a pipe of 0.5 mm diameter and 1 mm length.

3.2 Gas composition and properties

For the primary stream the natural gas composition in Graz is used. The secondary flow composition for the desired operating point is given by the AVL Fuel Cell Department, both can be seen in table 3.1. To get the heat capacity ratio γ for further calculations, the specific heat coefficient c_p and the gas constant R for each composition are needed.

For the individual molecular gases the molar heat capacity $C_{mpi}(T)$ at a temperature T is given by the Shomate equation in [5] as a polynomial of the form

$$C_{mpi}(T) = A + B\frac{T}{1000} + C\frac{T^2}{1000^2} + D\frac{T^3}{1000^3} + E\frac{1000^2}{T^2}. \tag{3.4}$$

The heat capacity of a gas mixture g is found by summing up all individual heat capacities multiplied by their molar fractions ν_i present in the gas mixture.

$$C_{mp,g}(T) = \sum_{i=1}^{n} \nu_i \cdot C_{mpi}(T) \tag{3.5}$$

In the same way, the molar mass M_g of a gas composition g is found by

$$M_g = \sum_{i=1}^{n} \nu_i \cdot M_i. \tag{3.6}$$

Table 3.1: Primary and secondary gas compositions. Primary is the natural gas composition in Graz and secondary is given by the AVL Fuel Cell Department for $\omega = 10.5$ (ID560-55).

Gas	**Chemical formula**	**Primary** in % mol	**Secondary** in % mol
Hydrogen	H2	0.00	8.66
Methane	CH4	93.91	0.00
Ethane	C2H6	1.43	0.00
Propane	C3H8	0.43	0.00
Butane	C4H10	0.14	0.00
Pentane	C5H12	0.03	0.00
Hexane	C6H14	0.02	0.00
Nitrogen	N2	0.8	0.22
Carbon monoxide	CO	0.00	4.68
Carbon dioxide	CO2	0.23	29.15
Steam	H2O	0.00	57.29

With the ideal gas constant $R = 8.314\,459\,\mathrm{J\,mol^{-1}\,K^{-1}}$, the heat capacity ratio γ_g is then given by

$$\gamma_g = \frac{C_{mp,g}}{C_{mv,g}} = \frac{C_{mp,g}}{C_{mp,g} - R}. \tag{3.7}$$

The specific gas constant of a gas composition g is found by dividing the ideal gas constant by the molar mass of the composition.

$$R_g = \frac{R}{M_g} \tag{3.8}$$

The mass fractions μ_i of a gas composition g are found by dividing the mass per mol of an individual gas by the mass per mol of the total gas composition:

$$\mu_i = \frac{M_g \nu_i}{\sum_{i=1}^{n} M_g \nu_i} \tag{3.9}$$

The mass specific values of the heat capacity coefficient $c_{p,g}$ of a gas composition g are found by dividing through the molar mass:

$$c_{p,g} = \frac{C_{mpi,g}}{M_g} \tag{3.10}$$

3.3 Output values for a heat exchanger

If a higher temperature for the primary stream is desired, the necessary energy to reach it can be supplied by the secondary stream through a heat exchanger as shown in fig. 3.3. The inlet temperatures of the heat exchanger (3) are given by the AVL Fuel Cell Department for the operating point at $\omega = 10.5$. The outlet temperatures of the heat exchanger have to be found by using the energy equation:

$$H_{p,out} + H_{s,out} = H_{p,in} + H_{s,in} \tag{3.11}$$

$$m_{p,out}h_{p,out} + m_{s,out}h_{s,out} = m_{p,in}h_{p,in} + m_{s,in}h_{s,in} \tag{3.12}$$

As the mass flow at the inlet is the same as at the outlet, eq. 3.12 can be written as

$$m_p \left(h_{p,out} - h_{p,in}\right) + m_s \left(h_{s,out} - h_{s,in}\right) = 0. \tag{3.13}$$

By dividing through m_p, the fraction of the masses is equal to the entrainment ratio $\frac{m_s}{m_p} = \omega$.

$$\left(h_{p,out} - h_{p,in} +\right) + \omega \left(h_{s,out} - h_{s,in}\right) = 0 \tag{3.14}$$

$$\Delta h_p + \omega \Delta h_s = 0 \tag{3.15}$$

The specific enthalpy differences in eq. 3.15 can be calculated by integrating the specific heat ratio c_p:

$$\Delta h = \int_1^2 c_p \, dT \tag{3.16}$$

For a gas mixture, the change in specific enthalpy is equal to the mass weighted sum of all the individual changes in specific enthalpy:

$$\Delta h = \sum_{i=1}^{n} \left(\mu_{pi} \cdot \int_1^2 c_{pi} \, dT \right) \tag{3.17}$$

Considering temperature dependant specific heat ratios $c_p\left(T\right)$ in eq. 3.17, eq. 3.15 transforms to

$$\sum_{i=1}^{n} \left(\mu_{pi} \cdot \int_1^2 c_{pi,p}\left(T\right) \, dT \right) + \omega \sum_{i=1}^{n} \left(\mu_{si} \cdot \int_1^2 c_{pi,s}\left(T\right) \, dT \right) = 0 \tag{3.18}$$

Using an integration of the Schomate equation (eq. 3.4), eq. 3.18 is only a function of the outlet temperatures T_{p2} and T_{s2}. By defining T_{p2} as $T_{s2} - \Delta T$, where ΔT is the difference between the temperatures at the outlet of the heat exchanger, eq. 3.18 can be solved iteratively for T_{s2}. With a primary stagnation temperature of 293.15 K and a secondary stagnation temperature of 865 K, the outlet temperatures calculated by eq. 3.18 are both 782.3 K at $\omega = 10.5$, assuming a perfect heat exchanger with $\Delta T = 0$.

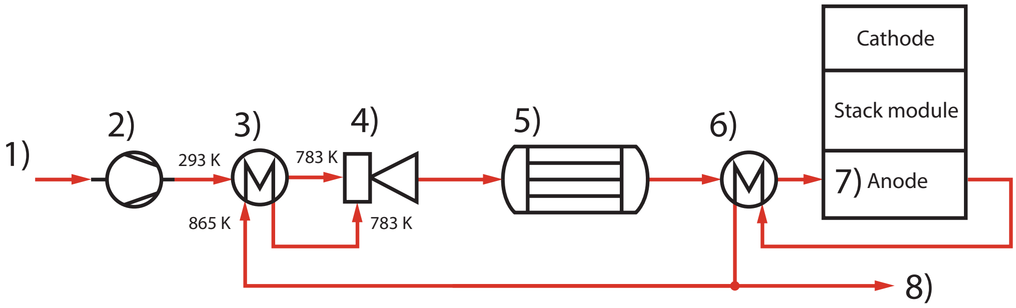

Figure 3.3: Flowsheet of the anode-gas flow. Components shown are the inlet of the natural gas (1), the external compressor (2), the ejector heat exchanger (3), the ejector (4), the pre-reformer (5), the pre-heater (6), the anode of the fuel cell (7) and the outlet (8) to the oxicat.

3.4 Boundary conditions

For the CFD simulation of the ejector, two sets of boundary conditions are used, with either a fixed entrainment ratio or a fixed suction pressure. For either of them the temperatures at the inlet have to be defined. For the desired operating point, the primary stagnation temperature is 293.15 K and the secondary 865 K, as seen in table 3.2. If a higher primary temperature is used, the calculations in section 3.3 are performed to find the secondary temperature after a heat exchanger.

The primary inlet boundary condition is defined with a fixed mass flow. The primary pressure adjusts itself according to the nozzle throat diameter calculated in section 3.5. At the boundary conditions for a fixed entrainment ratio, the secondary

Table 3.2: Boundary conditions and load constraints at $\omega = 10.5$ and 100 % fuel cell load. (AVL Fuel Cell Department calculation ID560-55)

Parameter	Name	Value	Unit
Primary inlet temperature	T_{p0}	293	K
Secondary inlet temperature	T_{s0}	865	K
Primary mass flow	$\dot{m}_p$	0.186 9	g/s
Secondary mass flow	$\dot{m}_s$	1.967 2	g/s
Secondary inlet pressure	p_{s0}	94 410	Pa
Diffuser outlet pressure	p_4	98 179	Pa
Suction pressure	Δp	3 770	Pa

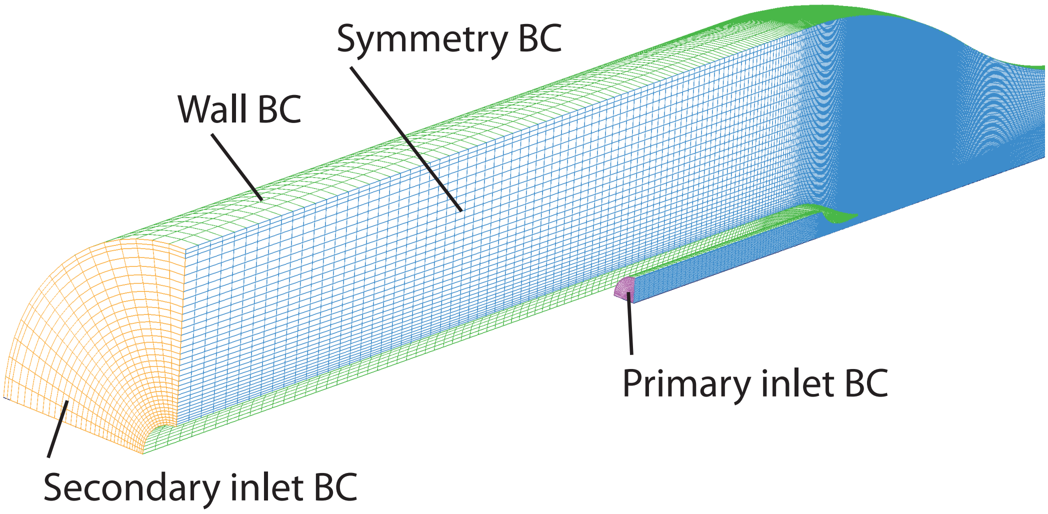

Figure 3.4: Boundary conditions applied on the inlet side of the structured mesh.

inlet boundary condition is also given as a fixed mass flow with $\dot{m}_s = \omega \cdot \dot{m}_p$. The outlet boundary condition in this case is a static or total pressure boundary condition. Both give similar results, as the flow velocity at the outlet is relatively low. The total pressure boundary condition in AVL Fire^{TM} does not use the stagnation pressure, but the pressure from

$$p_{total} = p_{stat} + \rho \frac{v^2}{2} \tag{3.19}$$

as if the medium was incompressible. This does, however, not change the results, as the velocities are relatively low at the outlet. The value for the static or total pressure is given by the AVL Fuel Cell Department as $p_4 = 98\,179\,\mathrm{Pa}$ for the operating point at $\omega = 10.5$.

In the case of fixed suction pressure, the secondary inlet boundary condition is changed to a static or total pressure boundary condition with a value of $p_{s0} = 94\,410\,\mathrm{Pa}$. The entrainment ratio can then be found through the mass flow over the secondary inlet boundary condition surface.

In all cases the walls are modelled as adiabatic and symmetry boundary conditions are used at the cut surfaces. The applied boundary conditions can be seen in fig. 3.4 for the inlets and fig. 3.5 for the outlet. Not visible in these figures is the second symmetry boundary condition which is applied on the face on the bottom of the mesh.

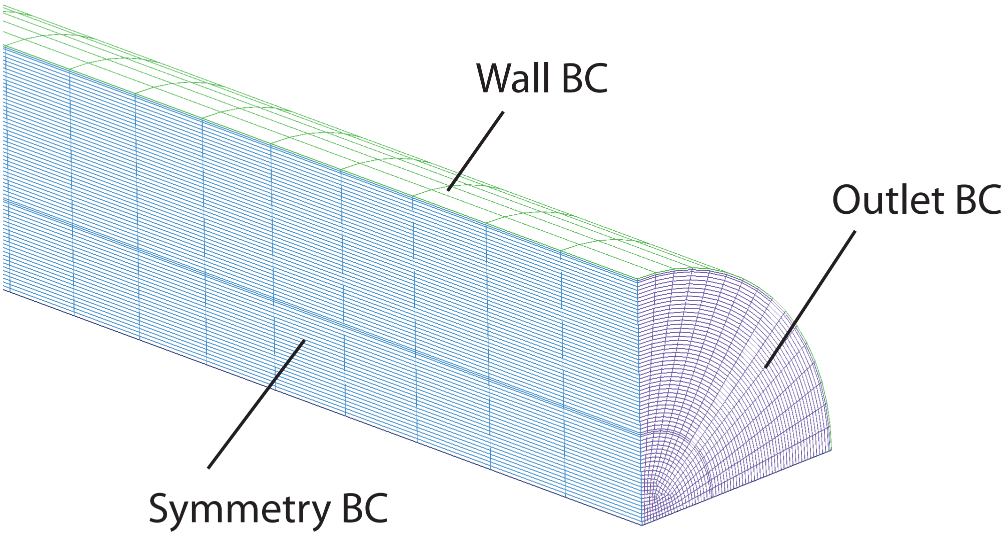

Figure 3.5: Boundary conditions applied on the outlet side of the structured mesh.

3.5 Nozzle design approach

The geometry of the nozzle defines not only the state of the flow at the nozzle exit, but also the pressure prior to the nozzle when the mass flow and temperature are given as boundary conditions. By using gas dynamic equations, the nozzle throat diameter and nozzle exit diameter can be calculated for a desired maximum primary pressure.

At the throat the primary flow reaches a choked condition, where the velocity is equal to the sonic speed c_T, which can be calculated with eq. 2.10 for the given stagnation values at the primary inlet. With the density at the throat ρ_T according to eq. 2.31 the throat area A_T can be calculated from the continuity equation

$$A_T = \frac{m_p}{\rho_T c_T} \cdot \sqrt{\eta_N}. \tag{3.20}$$

where η_N is the nozzle efficiency. This gives the throat diameter

$$d_T = \sqrt{\frac{4A_T}{\pi}} \tag{3.21}$$

When designing a nozzle for the first time, the efficiency η_N is assumed as an arbitrary value between 0.9 and 1. For this guessed efficiency the nozzle geometry is calculated and the resulting primary stagnation pressure obtained using a CFD simulation. With eq. 2.30 to eq. 2.31 the sonic velocity and density at the throat can be calculated using the primary stagnation pressure of the simulation. This gives the simulated nozzle efficiency as

$$\eta_N = \left(\frac{m_p}{\rho_T c_T A_T} \right)^2 . \tag{3.22}$$

This gives an accurate efficiency when the nozzle operates at a pressure level close to the simulated one.

The nozzle exit diameter D_{ne} is chosen in a way that the stream is neither strongly over- nor underdeveloped. For this the primary static pressure at nozzle exit p_{pne} has to be equal to the secondary static pressure p_{sc} at the beginning of the suction chamber. As the losses in the secondary flow path are insignificant (see section 5.3), the secondary pressure in the suction chamber is assumed to be equal to the secondary inlet stagnation pressure, as the secondary velocity is relatively low.

$$p_{pne} = p_{s0} \tag{3.23}$$

With eq. 3.23, the Mach number at nozzle exit M_{p1} can be found through eq. 2.30 by an iterative process. The nozzle exit diameter d_{NE} is then found through the nozzle exit area A_{NE} given by

$$A_{NE} = \frac{A_T}{M_{p1}\sqrt{\eta_N}} \left(\frac{2 + (\gamma_p - 1) M_{p1}^2}{\gamma_p + 1} \right)^{\frac{\gamma_p+1}{2(\gamma_p-1)}} \tag{3.24}$$

$$d_{NE} = \frac{4\sqrt{A_{NE}}}{\pi} \tag{3.25}$$

where η_N is the previously calculated nozzle efficiency [9]. For the calculated Mach number at the nozzle exit, the state variables are found by applying eq. 2.28, eq. 2.30 and eq. 2.31.

3.6 Available primary pressure

For the SOFC the natural gas is supplied by the local pipeline network, where the positive pressure is only in the mbar range. For the motive gas to reach the desired pressure, a compressor is necessary. This compressor should not have a power consumption much larger than the current blower in the SOFC. The blower is designed to work at an efficiency of 10 %, where it would require an electric power of up to 250 W. An offer for an ATEX (explosive atmosphere) membrane compressor with a power requirement of 250 W was inquired from GUT GmbH. The characteristic curve for the relative pressure available at a certain normal volume flow for this compressor is shown in fig. 3.6.

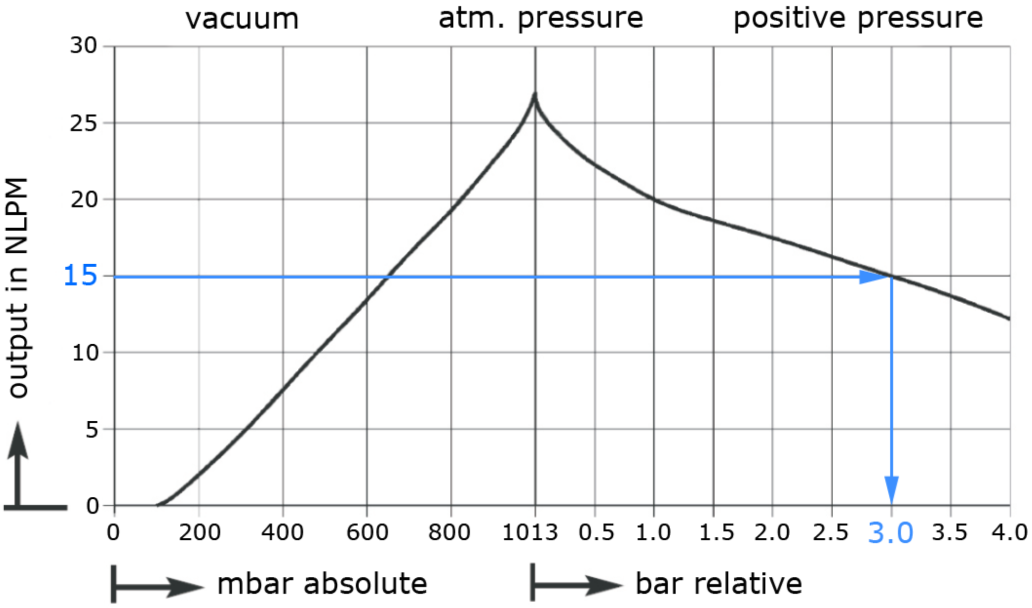

Figure 3.6: The relative pressure the ATEX compressor can achieve for a given normal volume flow.

To calculate the normal volume flow, the natural gas composition of table 3.1 is taken at a mass flow of $\dot{m}_p = 1.82\,\mathrm{g/s}$. The normal conditions according to DIN 1343 are $T_n = 273.15\,\mathrm{K}$ and $p_n = 1.013\,25\,\mathrm{bar}$. The volume flow in normal litre per minute is calculated by the ideal gas law

$$\dot{V}_n = \frac{\dot{m}_p R_p T_n}{p_n} = 14.73\,\mathrm{NLPM} \tag{3.26}$$

where the gas constant $R_p = 500.36\,\mathrm{J/kg\,K}$ is calculated by eq. 3.6 and eq. 3.8. For this normal volume flow, the compressor can supply the natural gas at 3 bar positive pressure, or 4 bar absolute pressure when assuming the ambient pressure at 1 bar.

3.7 1D-model of an ideal ejector

The goal of this section is to evaluate the influence of the inlet parameters on an ideal ejector and identify theoretical boundaries. If the ideal ejector can not reach

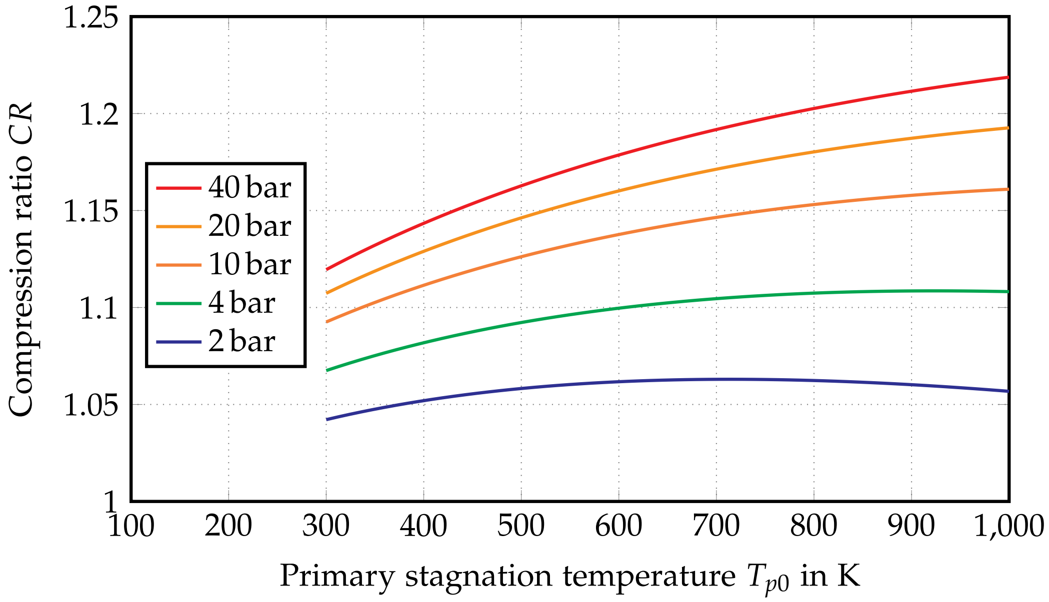

Figure 3.7: Temperature influence on the compression ratio of an ideal ejector using Huang's design method, calculated for various primary stagnation pressures p_{p0}.

the desired performance, optimization of a real ejector can't produce this performance either. Assuming frictionless and adiabatic flow, ideal mixing and a single shock of the mixed gas flow in the model of Huang [17], the resulting compression ratio is plotted for various inlet conditions while the entrainment ratio is fixed at 10.5. For the desired operating point, seen in table 3.2, the compression ratio has to be at least

$$CR = \frac{p_4}{p_{s0}} = \frac{98179}{94410} \approx 1.04. \tag{3.27}$$

In the first variation, seen in fig. 3.7, the primary stagnation temperature is varied from 300 K to 1 000 K. For primary pressures at 10 bar and higher, an increase in primary temperature always increases the achieved compression ratio in the considered temperature range. Pressures below 10 bar show a maximum in the compression ratio at temperatures below $1000\,K$ which shifts to lower temperatures, the lower the pressure is. All the ideal ejectors reach compression ratios of 1.04 or higher in this temperature range for primary pressures above 2 bar.

The variation of the primary pressure at fixed primary inlet temperatures, as seen in fig. 3.8, always results in an increase of the compression ratio when the primary

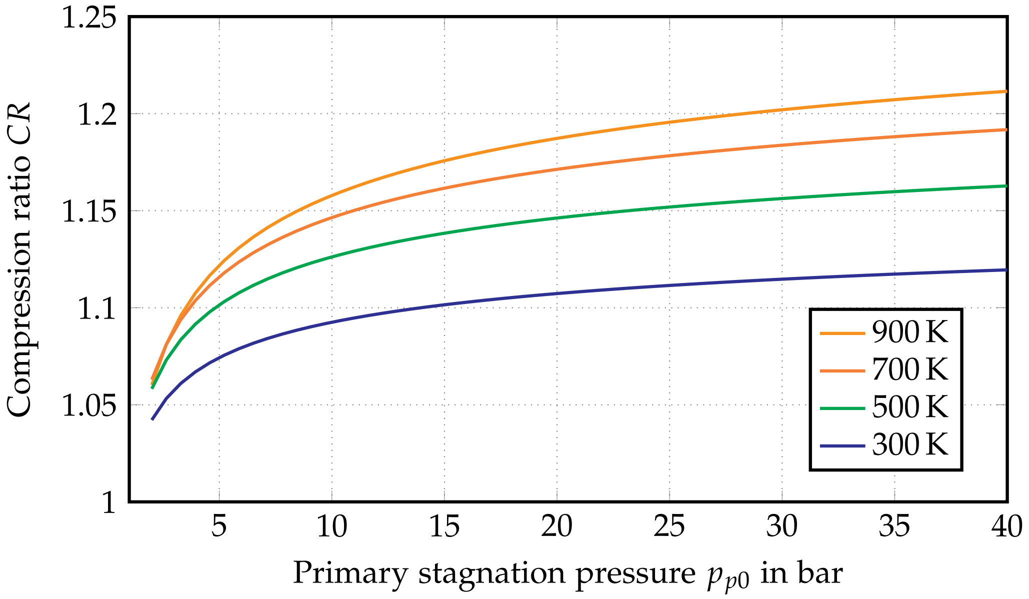

Figure 3.8: Pressure influence on the compression ratio of an ideal ejector using Huang's design method. Calculated for various primary stagnation Temperatures T_{p0}.

pressure is increased. An increase of the primary pressure below 10 bar shows a stronger positive effect than an increase at higher pressure levels.

The results show that the operating point can be achieved by an ideal ejector at primary temperatures above 300 K and primary pressures above 2 bar. This does, however, not mean that such a performance can be achieved by an actual ejector.

A review of ejector efficiencies in various ejector systems by F. Liu [23] analysed the efficiency coefficient of the primary nozzle, the secondary nozzle (the secondary flow path), the mixing and the diffuser used in literature. Nozzle efficiencies were found to generally be between $\eta_N = 0.8$ and 0.9, the mixing efficiency between $\eta_M = 0.85$ and 0.95 and the diffuser efficiencies between $\eta_D = 0.75$ and 0.85. Similar efficiencies for the nozzle and the diffuser can be expected for the ejector in this work. The mixing efficiency is expected to be lower for the following reason: The ejector literature analysed by Liu only discussed ejectors in applications where the entrainment ratio is below unity. This differs from SOFC applications, where the entrainment ratio has to be higher ($\omega > 8$).

Ksayer [21] found that the mixing efficiency depended on the ratio of the mixing chamber area A_{MC} to the nozzle throat area A_{NT} and developed a formula to predict it in a range of $\eta_M = 0.9$ to 0.98. The formula resulted in lower mixing efficiencies for higher area ratios and was validated for a maximum area ratio of 3.5, where the lowest efficiency with 0.9 was found. Considering that the area ratios in this work are generally above 10, a lower mixing efficiency has to be expected.

4 CFD model validation

In this work CFD simulations are used to evaluate the ejector performance. To validate the mesh sizes and solver settings used in these simulations, testbed results are required for a comparison.

4.1 Testbed results

As a basis for this validation, the testbed results generated by D. Bischof for his master thesis [3] are used. Bischof evaluated two different nozzle designs and two different mixing chambers in various combinations. Early in the work of Bischof it was discovered that the nozzle design B in table 4.1 had a higher performance than nozzle design A for both mixing chamber designs. Nozzle design A was thus discarded and only the combination of the nozzle design B with the two mixing chamber designs was evaluated in detail. This section also only discusses the testbed results of the nozzle design B.

An overview of the performance of the ejector with nozzle design B can be seen in fig. 4.1. Both mixing chamber designs were tested with four different primary mass flows. While the primary mass flow was at a fixed rate, the throttle of the recirculation path seen in fig. 4.2 was closed over the span of a minute. This way the pressure loss in the recirculation path slowly increased from the point with the highest possible entrainment ratio and lowest suction pressure until the highest possible suction pressure at an entrainment ratio of zero was reached. All tests

Table 4.1: Main parameters of the ejector designs tested by D. Bischof [3]. Nozzle design A was discarded and not evaluated in detail.

		Design A	**Design B**
Nozzle throat diameter	d_{NT}	(0.80 mm)	0.58 mm
Nozzle exit diameter	d_{NE}	(0.87 mm)	0.91 mm
Ejector mixing chamber diameter	d_{MC}	10.50 mm	6.00 mm
Ejector mixing chamber length	l_{MC}	70.40 mm	67.09 mm

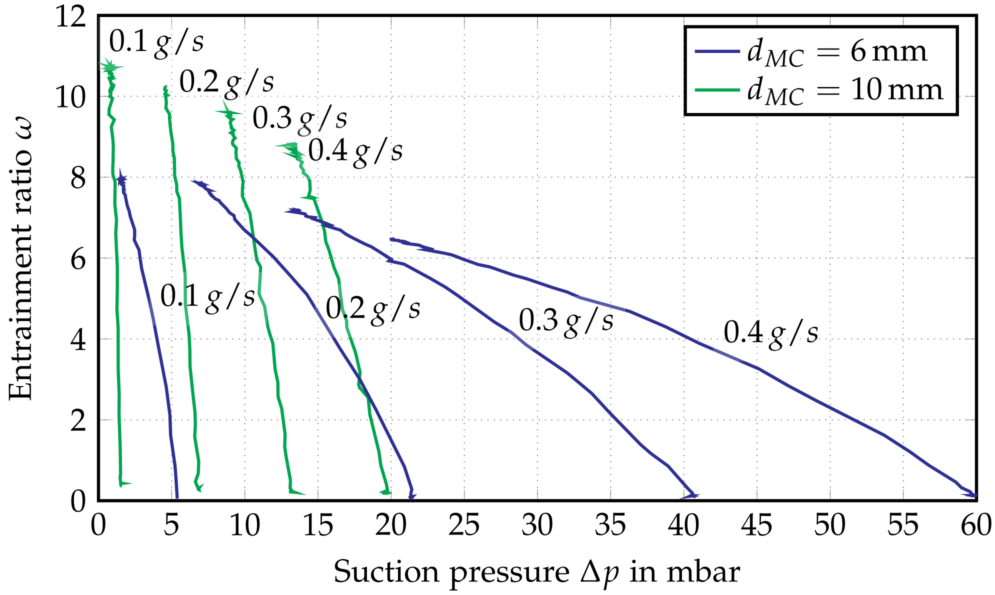

Figure 4.1: Test bed results for air at various primary mass flows. Redrawing of figure 6.29 in [3].

used dry air at room temperature for the primary and secondary stream.

The mixing chamber diameter of 10 mm showed higher maximum entrainment ratios but lower maximum suction pressures compared to the 6 mm mixing chamber. Furthermore higher primary mass flows lead to lower maximum entrainment ratios. All those effects can be explained by higher friction losses at higher gas velocities. As higher primary mass flows lead to higher total volume flows for the same entrainment ratios, the average velocity increases and thus the friction losses increase as well.

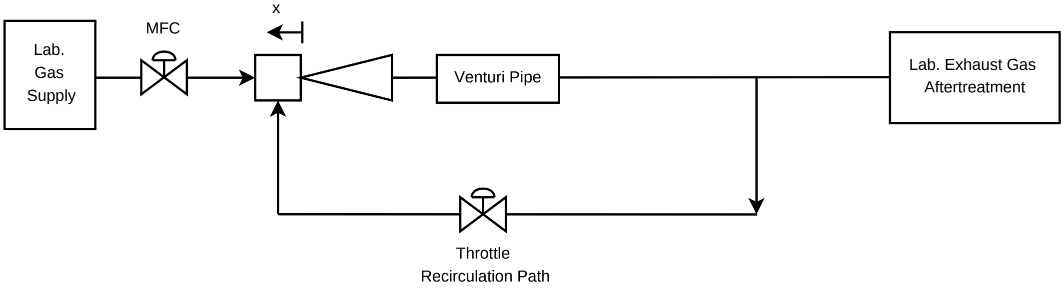

Figure 4.2: Ejector test bed setup, taken from figure 6.2 in [3].

4.2 Ejector configuration and boundary conditions

During testing D. Bischof used three different nozzle positions in regard to the mixing chamber. For the validation in this work, the default nozzle position POS1 (see [3, p. 45]) is used, where the exit of the nozzle aligns with the start of the mixing chamber, making the ejector a constant-area ejector. This position is used even though other positions showed better performance, as the performance of the ejector is not of interest for the validation. For the mixing chamber, design A with the larger mixing chamber diameter of 10 mm is used, since it was previously used in the thesis of M. Tkaucic [26] to validate the CFD simulation and can thus show the influence of the CFD setup changes on the results. A list of the main geometry parameters and their value can be seen in table 4.2.

On the testbed, dry air was used for both the primary and secondary stream. For the CFD simulation the molar fractions seen in table 4.3 are used for dry air at 293.15 K.

The primary and secondary inlet conditions are both defined with a fixed mass flow. While the primary mass flow is a fixed value, the secondary mass flow is dependent on the given entrainment ratio as $\dot{m}_s = \omega \cdot \dot{m}_p$. As the simulations do not result in the lines seen in fig. 4.1, but only in a single value for the suction pressure at a given entrainment ratio, five entrainment ratios are evaluated to reduce the simulation effort. For the primary stream the case with a mass flow of 0.2 g/s was chosen originally. During simulation it became apparent that the primary flow did not maintain supersonic velocity until the end of the diverging nozzle section as can be seen in fig. 4.3. This meant that the pressure ratio in the simulations with $\dot{m}_p = 0.2\,\mathrm{g/s}$ was above the critical value and the nozzle thus overdeveloped. For this reason a second case with a mass flow of 0.4 g/s is also simulated on five entrainment ratios, to ensure that the calculations are also valid when the nozzle

Table 4.2: Main geometry parameters used for the CFD simulation.

Parameter	Name	Value	Unit
Suction chamber length	l_{SC}	0	mm
Nozzle throat diameter	d_{NT}	0.58	mm
Nozzle exit diameter	d_{NE}	0.91	mm
Ejector mixing chamber diameter	d_{MC}	10.50	mm
Ejector mixing chamber length	l_{MC}	70.40	mm

Table 4.3: Molar fractions used for dry air in the validation simulations.

Gas	Chemical formula	Molar fraction
Nitrogen	N_2	0.780 8
Oxygen	O_2	0.209 5
Argon	Ar	0.009 3
Carbon dioxide	CO_2	0.000 4

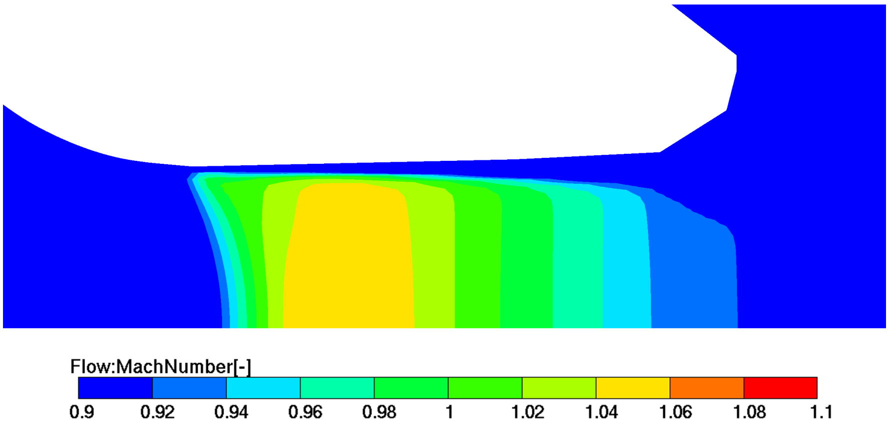

Figure 4.3: Mach number in the nozzle design B shows that the flow does not sustain supersonic velocity to the nozzle exit at a mass flow of 0.2 g/s.

operates in a supersonic condition (see fig. 4.4).

For the outlet a static pressure boundary condition of 101 325 Pa is used. This is no measured value, but only the difference in pressure between the outlet and the secondary inlet, the suction pressure Δp, is of interest and not the absolute value of the secondary inlet pressure. The influence of this changed pressure level on the pressure difference is assumed to be insignificant. A summary of the values applied at the boundary conditions is given in table 4.4. Also required for the simulations are boundary conditions at the walls and the cut surfaces. The walls are modelled as *adiabatic wall boundary conditions* and at the cut surfaces *symmetry boundary conditions* are used.

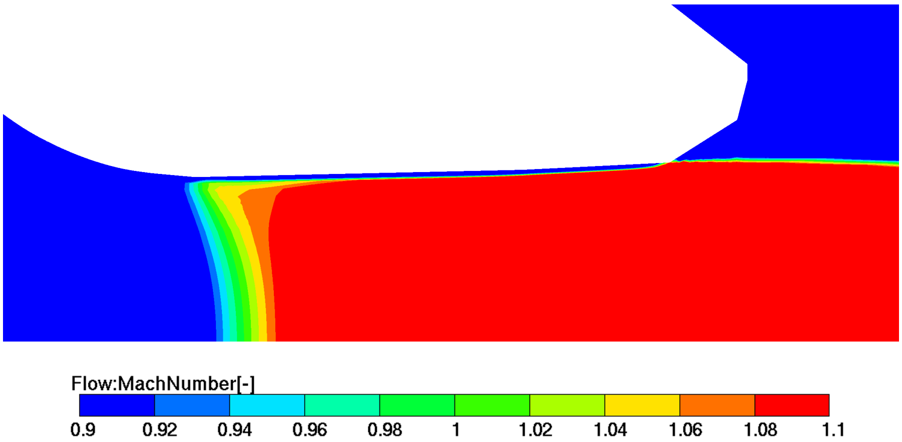

Figure 4.4: Mach number in the nozzle design B maintains supersonic velocity until the nozzle exit at a mass flow of 0.4 g/s.

Table 4.4: Boundary conditions used for the validation CFD simulations.

Parameter	**Name**	**Value**	**Unit**
Primary inlet temperature	T_{p0}	293	K
Primary inlet mass flow	$\dot{m}_p$	0.2 or 0.4	g/s
Primary gas composition	-	dry air	
Secondary inlet temperature	T_{s0}	293	K
Secondary inlet mass flow	$\dot{m}_s$	$\dot{m}_p \cdot \omega$	g/s
Secondary gas composition	-	dry air	
Outlet pressure	p_4	101 325	Pa

4.3 CFD solver settings

All simulations are performed in AVL Fire$^{\text{TM}}$, a commercial CFD software developed by AVL List GmbH. Fire$^{\text{TM}}$ uses a general fluid flow solver based on the finite-volume method. Here the dependent variables are stored at the center of the control volumes while at boundaries they are stored at the center of the boundary faces.

Previous work on ejector simulations at AVL found better results with structured meshes and timestepping instead of steady simulations done on polymeshes. For the turbulence model the k-zeta-f model is used as the default model in AVL-Fire$^{\text{TM}}$. In literature, most CFD simulations of ejectors were done in Ansys Fluent, where the standard k-ϵ-model, realizable k-ϵ-model, the RNG k-ϵ and the SST k-ω-model were used [14][25]. For details on the k-zeta-f model see *A robust near-wall elliptic-relaxation eddy-viscosity turbulence model for CFD* by Hanjalic et al. [15] and for the other models see *Turbulence modeling for CFD* by Wilcox et al. [40].

For the flux discretisation the TVD scheme MINMOD relaxed (see [36, ch. 5.10.2]) is used to calculate the discontinuities at the shock waves with high accuracy at a reasonable grid size. This scheme can be blended with a first order upwind scheme, which is a simpler and robuster scheme, by using a blending factor. Blending combines two different flux calculation methods by multiplying each with a weighting factor and adding them together. At a blending factor of 1, AVL-Fire$^{\text{TM}}$ only uses the MINMOD relaxed scheme for the calculation of the fluxes, at a blending factor of 0 only the first order upwind scheme is used. Even though a high blending factor is preferred, it is only possible to realize with very high cell densities [12]. The simulations of the 0.4 g/s primary mass flow cases with a blending factor of 1 are unstable and diverge when the shock train structure starts to form. For this reason a blending factor of 0.8 is used. A blending factor of 0.6 is also simulated to see the influence of the increased numerical diffusion on the suction pressure.

A summary of the solver settings can be seen in table 4.5.

Table 4.5: Settings used for the CFD simulations performed in AVL Fire$^{\mathrm{TM}}$.

Name	**Setting**
Run mode	Timestep
Turbulence model	k-zeta-f
Energy equation	Yes
Viscous heating	Yes
Pressure work	Yes
Two stage pressure correction	Yes
Wall treatment	Hybrid wall treatment
Heat transfer model	Standard wall function
Compressibility	Compressible
Discretization	Simple/Piso
Calculation of derivatives	Least sq. fit
Differencing	
Momentum scheme	MINMOD relaxed
Continuity scheme	MINMOD relaxed
Turbulence scheme	Upwind
Energy scheme	Upwind
Scalar scheme	Upwind
Linear solver type	
Solver for momentum	GSTB
Solver for continuity	AMG
Solver for turbulence	GSTB
Solver for pressure	GSTB
Solver for scalar	GSTB
Underrelaxation factors	
Momentum	0.6
Pressure	0.1
Turbulent kinetic energy	0.4
Turbulence dissipation rate	0.4
Energy	0.95
Mass source	1
Viscosity	1
Scalar	0.8

4.4 Model simplifications

Multiple model simplifications are made to reduce the computational simulation effort. The influence of heat losses over the walls is ignored and no solid material is modelled. The secondary pipe is modelled without the bending seen in fig. 4.5, because the velocities are small in this section and no significant losses are expected. The struts that held the nozzle inside the secondary pipe are removed because they also did not show significant losses in previous simulations and removing them simplifies the generation process of the mesh significantly. These simplifications enable the use of symmetry boundary conditions as the model is now rotationally symmetric. 90° are modelled, so the cells at the center line are orthogonal, as shown in fig. 4.6. This reduces the total amount of cells and thus the amount of CPUs needed to perform the simulation in the same time as a simulation of the full model.

The small size of the nozzle made the production of the rounding at the end of the diverging nozzle section (see fig. 4.7) difficult. An investigation of the manufactured nozzle with an incident light microscope found the ending of the nozzle not to be in the rounded shape as in the shop drawing but in a conic shape. Due to this the nozzle ending was also modelled conic as seen in fig. 4.7, which is advantageous for the mesh quality, as the rounding would have led to highly skewed cells in this area.

The final structured mesh that is used for the validation simulations can be seen in fig. 4.8.

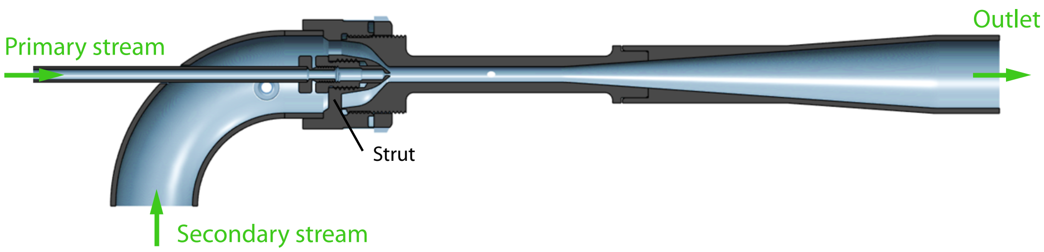

Figure 4.5: CAD model of the ejector used for the testbed validation by D. Bischof.

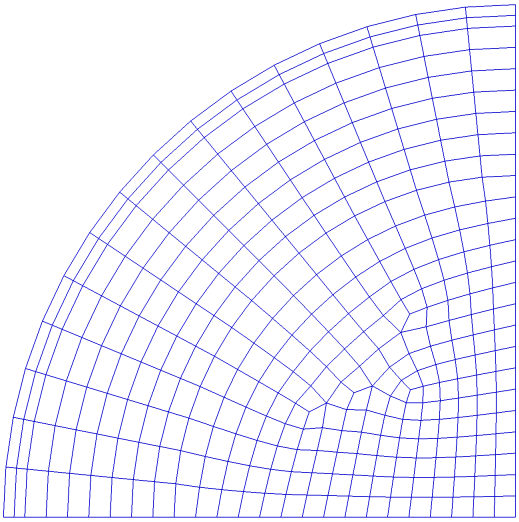

Figure 4.6: Mesh of the primary inlet when using symmetry boundary conditions.

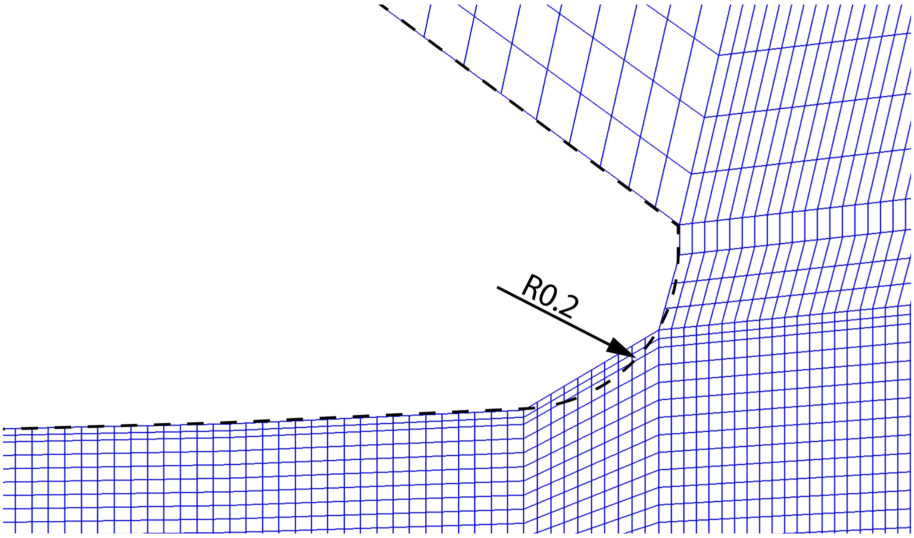

Figure 4.7: Mesh at the nozzle exit with an indication on the original geometry in the shop drawing.

Figure 4.8: Structured mesh used for the validation simulations. Only part of outlet pipe is shown.

4.5 Model validation results

A comparison of testbed and CFD simulation results is shown in fig. 4.9. As dis- ussed before, two different primary mass flows were simulated, one where the stream through the nozzle remains subsonic ($\dot{m}_p = 0.2\,\mathrm{g/s}$) and one where the stream in the nozzle exited at supersonic conditions ($\dot{m}_p = 0.4\,\mathrm{g/s}$). The simulations for $\dot{m}_p = 0.2\,\mathrm{g/s}$ used a blending factor b of 1, while the simulations with $\dot{m}_p = 0.4\,\mathrm{g/s}$ required a blending factor lower than unity, as the shock waves after the nozzle caused the simulations to diverge when it was chosen too high. As expected, the results for the blending factor $b = 0.6$ were smaller than for $b = 0.8$, because of the increased numerical diffusion at lower values for b. At $\omega = 2$ the reduction in suction pressure from $b = 0.8$ to $b = 0.6$ is $\sim 1\,\%$ and increases until it reaches $\sim 2\,\%$ at $\omega = 10$. Overall it can be said that a lower blending factor does not change the outcome of the simulation significantly and is thus acceptable to use in ejector simulations.

The obtained CFD results with timestepping and a structured mesh display a far better agreement to the testbed results than the steady calculation with a polymesh performed by M. Tkaucic in a previous thesis [26]. Additionally, the use of arithmetic multigrid for the continuity equations reduced calculation time, while the symmetry boundary conditions reduced the number of CPUs needed.

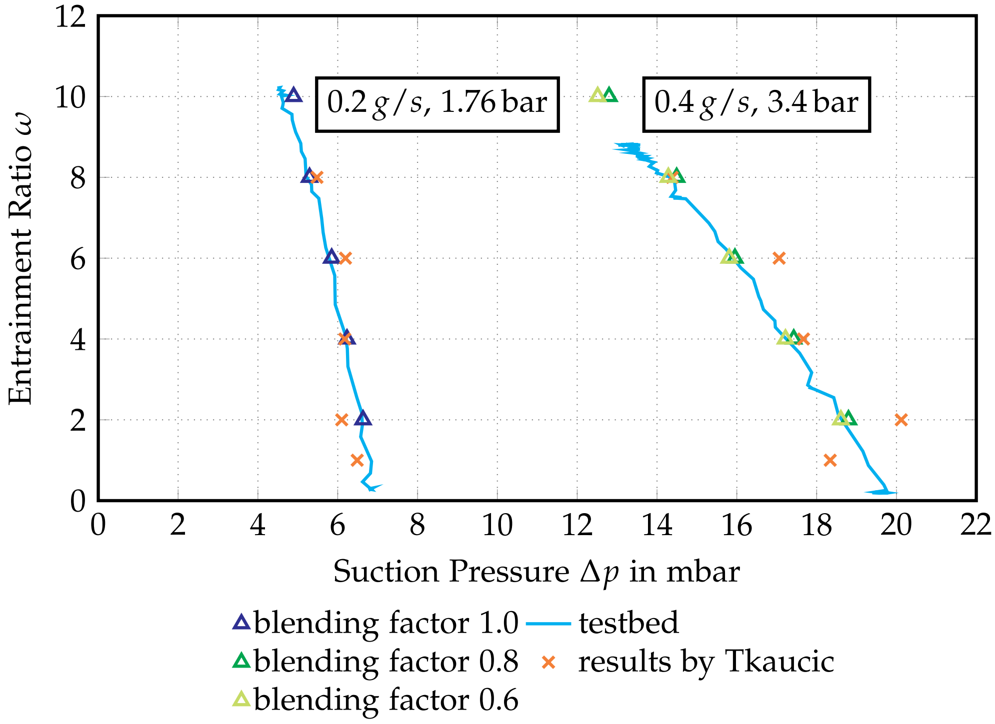

Figure 4.9: Comparison of the testbed results with the CFD results obtained for various blending factors. The primary mass flow and the corresponding primary pressure are shown for the two operating points that were used for validation. Also the validation results obtained by M. Tkaucic in his thesis [26] are shown, where he performed steady simulations on a polymesh.

5 CFD analysis

Multiple parameter variations require a large change in the model, so a new mesh has to be created each time. To speed up the mesh generation, MATLAB is used to create a cross section of a geometry according to given parameters. For this the nozzle throat and exit diameters will be calculated according to section 3.5, while other geometry parameters are chosen freely.

Prior to the analysis on the influence of various parameters, a systematic ejector design approach was taken according to the model by Zhu [43].

5.1 Model design in the matlab model

As each change of a parameter requires that part of the mesh or the whole mesh is generated anew, it is necessary to create a way to speed up this process. To this end a preprocessing tool was created in MATLAB.

The preprocessing tool finds the desired input temperatures according to section 3.3 and calculates the nozzle throat and exit diameter according to section 3.5 from the thermodynamic input data shown in table 5.1. This ensures that the primary pressure reaches the desired value for a given mass flow. Apart from these two computed diameters, all geometry parameters shown in fig. 5.1 have to be given as input. The outer contour of the suction chamber is defined by a third-order curve whose gradient at the inflection point is α_3, and whose lengths before and after the inflection point are defined by the angles α_1 and $alpha_2$. A list of these parameters can also be seen in table 5.2. Additionally the length of the grid cells in direction of the x-axis has to be given for all transitions between sections (e.g. for the transition from the suction chamber to the mixing chamber), the grid separations in radial direction at the inlets and the outlet, and the number of rotational grid separations are required.

The length of the diverging nozzle section is calculated only if the desired type is the parallel jet nozzle, for which it is defined by gasdynamic equations (see section 5.4.3) according to the method of Foelsch [13] to produce a nozzle as short as

Table 5.1: Input data required for the thermodynamic preprocessing.

Input	**Description**
Primary pressure	Stagnation pressure at the primary inlet
Secondary pressure	Stagnation pressure at the secondary inlet
Primary temperature	Primary stagnation temperature before the heat exchanger
Secondary temperature	Secondary stagnation temperature before the heat exchanger
Gas composition	Mass fractions at the primary and secondary inlet
Inlet temperature difference	Temperature difference between the primary and secondary stream after the heat exchanger
Entrainment ratio	Ratio of secondary to primary mass flow
Primary mass flow	Mass flow at the primary inlet
Nozzle efficiency coefficient	Specifies the change in performance of the actual nozzle to the calculated one
Nozzle shape	Shape of the nozzle: conic, quadratic or parallel jet design

possible.

The geometry of the diffuser is defined by

$$A\left(x\right)=\frac{A_{min}}{\frac{A_{min}}{A_{max}}+\left(1-\frac{A_{min}}{A_{max}}\right)\left(1-\frac{x}{L}\right)} \tag{5.1}$$

which ensures the same amount of pressure recovery per change in x for the whole length. Such a diffuser is often termed a *trumpet diffuser* because of its shape.

For this input data the tool generates a set of polylines, which are lines defined by multiple coordinate points, of the cross section as text files which can be read by AVL Fire$^{\text{TM}}$. These polylines contain the information of cell sizes and enable a fast generation of a new structured mesh.

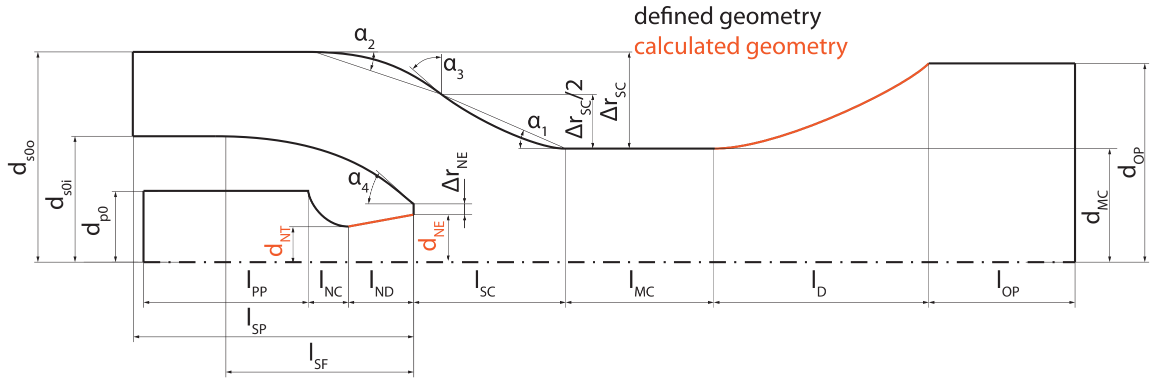

Figure 5.1: Diagram of required geometry input data.

Table 5.2: Geometry input data.

Name	Description
d_{p0}	Diameter of the primary pipe
d_{s0i}	Inner diameter of the secondary pipe
d_{s0o}	Outer diameter of the secondary pipe
d_{NT}	Diameter at the nozzle throat
d_{NE}	Diameter at the nozzle exit
d_{MC}	Diameter of the mixing chamber
d_{OP}	Diameter of the outlet pipe
l_{PP}	Length of primary pipe
l_{SP}	Length of secondary pipe
l_{SF}	Length of the curved inner section of the secondary pipe
l_{NC}	Length of the converging nozzle section
l_{ND}	Length of the diverging nozzle section
l_{SC}	Length of the suction chamber
l_{MC}	Length of the mixing chamber
l_D	Length of the diffuser
l_{OP}	Length of the outlet pipe
Δr_{NE}	Height of the nozzle nose
α_1	Inner angle of the suction chamber contour
α_2	Outer angle of the suction chamber contour
α_3	Suction chamber contour inflection angle
α_4	angle at the end of the curved inner section of the secondary pipe

5.2 Systematic ejector design approach by Zhu

A systematic approach for the design of ejectors for SOFC applications was proposed by Zhu in 2009 [43]. Because of the high entrainment ratios usually needed to avoid carbon deposition in SOFC applications, traditional 1D-models cause large errors. Zhu first suggested a non-constant velocity distribution in the mixing chamber in 2007, which lead to lower but more accurate entrainment ratios [44]. In [43] he adapted this non-constant velocity function v_r as dependent on the radius r inside the mixing chamber to the form

$$v_r = \begin{cases} v_{p2} & 0 \leq r \leq r_{p2} \\ v_{p2}\left(\frac{r_2 - r}{r_2 - r_{p2}}\right)^{n_v} & r_{p2} < r \leq r_2 \end{cases} \tag{5.2}$$

for higher entrainment ratios, as seen in fig. 5.2. v_{p2} is the velocity of the primary stream at the entry of the mixing chamber when the stream is fully expanded (static pressure equals secondary static pressure). r_{p2} is the radius of the primary stream at the entry of the mixing chamber and r_2 the radius of the mixing chamber. The velocity function exponent n_v is of the form

$$n_v = A_1\, exp\left(\frac{\beta_p}{0.05}\right) + A_2\, \beta_d + A_3 \tag{5.3}$$

where $\beta_p = \frac{p_s^{0.8}}{p_p^{1.1}}$ and $\beta_d = \frac{d_{MC}}{d_{NT}}$. Both β factors were found by Zhu by performing a data regression from multiple ejector tests. By integrating the velocity function multiplied by the average density

$$\bar{\rho} = \frac{p_{s0}}{RT_s} \tag{5.4}$$

over the area at the mixing chamber entry, the mean mass flow rate of the secondary flow can be calculated as:

$$\dot{m}_s = \int_{r_{p2}}^{r_p} \bar{\rho} v_r dA \tag{5.5}$$

$$= \frac{2\pi v_{p2}\left(r_2 - r_{p2}\right)\left(r_2 + r_{p2} + n_v r_{p2}\right)}{\left(n_v + 1\right)\left(n_v + 2\right)} \tag{5.6}$$

For any simulation or testbed result with a fixed CR the resulting $\dot{m}_s$ can be used to find n_v iteratively from eq. 5.6 by Newton's method:

$$f\left(n_v\right) = \frac{2\pi v_{p2}\left(r_2 - r_{p2}\right)\left(r_2 + r_{p2} + n_v r_{p2}\right)}{\left(n_v + 1\right)\left(n_v + 2\right)} - \dot{m}_s \tag{5.7}$$

$$n_{v,n+1} = n_{v,n} - \frac{f\left(n_{v,n}\right)}{f'\left(n_{v,n}\right)} \tag{5.8}$$

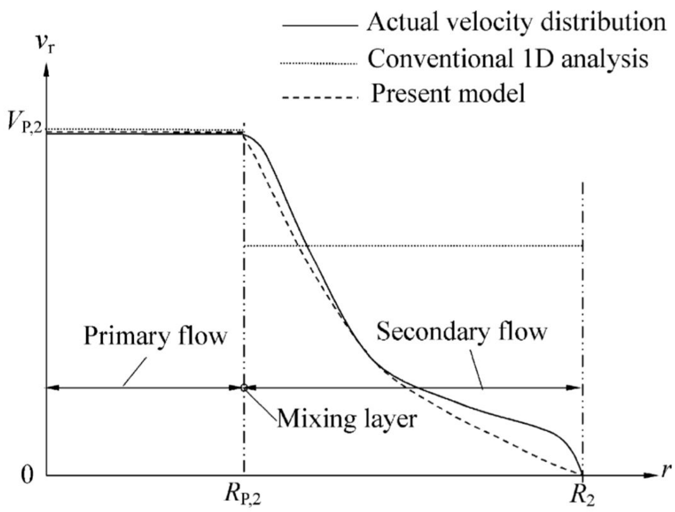

Figure 5.2: The velocity distribution at the entrance of the mixing chamber proposed by Zhu [43].

An initial guess of $n_{v,0} = 2$ is used and the algorithm repeated until $|f(n_v)| \leq 10^{-5}$. The coefficients A_1, A_2 and A_3 of eq. 5.3 can be calculated by solving a system of N linear equations of the form

$$\Psi \cdot X = \Gamma + \Delta \tag{5.9}$$

where Δ is the simulation error and Ψ, X, Γ are written as:

$$\Psi = \begin{bmatrix} exp\left(\frac{\beta_{p1}}{0.05}\right) & \beta_{d1} & 1 \\ exp\left(\frac{\beta_{p2}}{0.05}\right) & \beta_{d2} & 1 \\ \vdots & & \\ exp\left(\frac{\beta_{pN}}{0.05}\right) & \beta_{dN} & 1 \end{bmatrix}; \quad X = \begin{bmatrix} A_1 \\ A_2 \\ A_3 \end{bmatrix}; \quad \Gamma = \begin{bmatrix} n_{v1} \\ n_{v2} \\ \vdots \\ n_{vN} \end{bmatrix} \tag{5.10}$$

An initial set of $N = 6$ simulations with different primary pressures and diameter ratios β_d, as seen in table 5.3, is evaluated. Each simulation has the same suction pressure of 40 mbar and inlet temperatures of 782.3 K for the primary and secondary stream. By solving eq. 5.9 with the least squares method for X, the velocity function exponent n_v is found as

$$n_v = 0.03\,\exp\left(\beta_p/0.05\right) + 0.3523\,\beta_d + 0.2169. \tag{5.11}$$

Plotting this function for the three different pressures, as seen in fig. 5.3, shows that Zhu's equation for n_v wrongly assumes a pressure independent gradient when

Table 5.3: Variation of primary pressure and mixing chamber diameter at a constant suction pressure of 40 mbar

p_{p0} in bar	d_{MC} in mm	l_{SC} in mm	l_{MC} in mm	ω -
4	4	10	50	3.345 6
4	6	10	50	4.237 0
7	4	10	50	3.863 5
7	6	10	50	5.453 9
10	4	10	50	4.093 0
10	6	10	50	5.832 6

varying the mixing chamber diameter. In the simulation results the gradient of n_v when varying the diameter ratio is different for different primary pressures.For this reason in this work eq. 5.3 was changed to

$$n_v = A_1\, exp\left(\frac{\beta_p}{0.05}\right) + A_2\, \beta_d \beta_p^{0.7} + A_3 \tag{5.12}$$

to take into account the influence of the pressure ratio on the gradient of the n_v function when varying the diameter ratio. When solving the set of linear equations for eq. 5.12, the velocity function exponent n_v is found as

$$n_v = -0.016737\, exp\left(\frac{\beta_p}{0.05}\right) + 2.1775\, \beta_d \beta_p^{0.7} + 0.57688. \tag{5.13}$$

This leads to a better agreement with the simulation results, as seen in fig. 5.4.

Using eq. 5.13, the predicted change in entrainment ratio when varying the mixing chamber diameter for a fixed $\Delta p = 40\,\text{mbar}$ for various primary pressures is shown in fig. 5.5. A clear trend to use larger mixing chamber diameters for higher entrainment ratios is visible.
A set of simulations with a larger mixing chamber diameter of 8 mm shows, unlike the model prediction, a negative influence on the entrainment ratio for larger mixing chamber diameters at all the simulated primary pressures as seen in fig. 5.6. It is clear from these results that the required geometry can not be found by only varying the primary pressure and mixing chamber diameter. A closer look on the influence of different geometry parameters is needed. Although this section showed that the Zhu model should not be used to predict ejector performance outside of the data range provided by simulation or testbed results, it can be a useful tool to predict ejector performance between simulated or tested operating points.

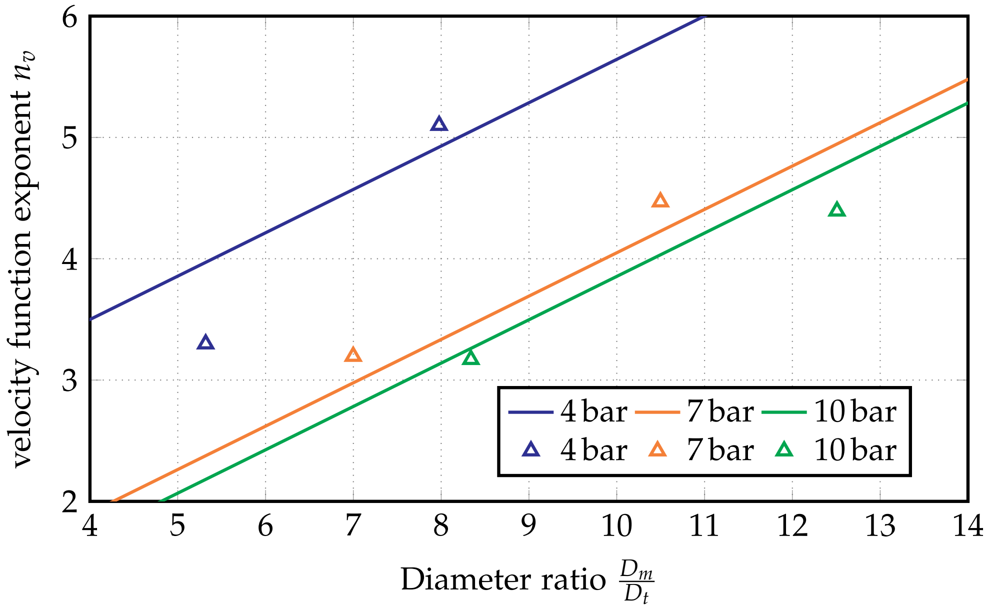

Figure 5.3: Value of the velocity function exponent n_v for three different primary pressures plotted as lines, compared to the required n_v to reach the entrainment ratio of the CFD simulation results (triangles).

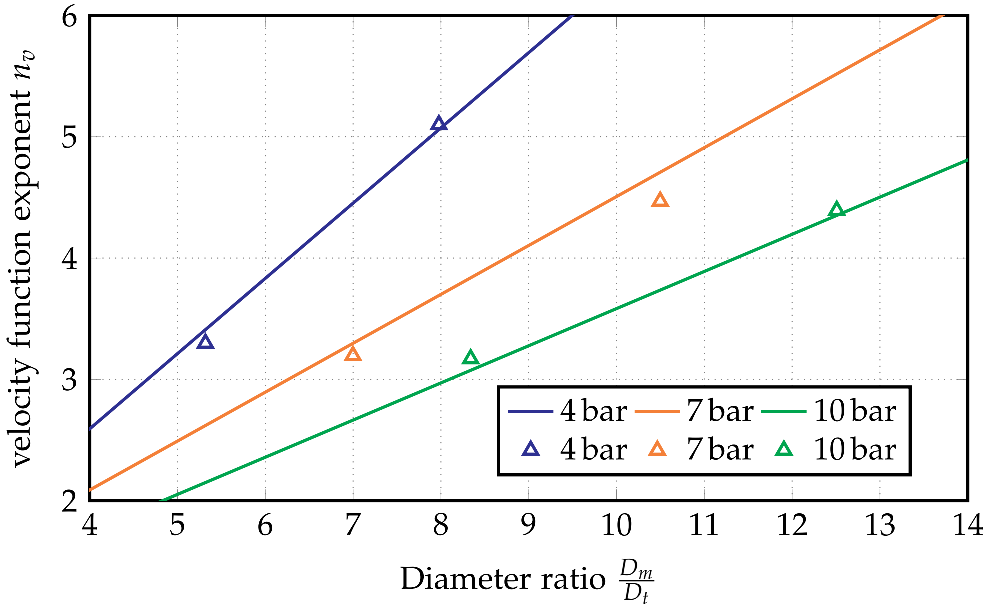

Figure 5.4: Modified n_v function for three different primary pressures plotted as lines, compared to the required n_v of the simulation results (triangles).

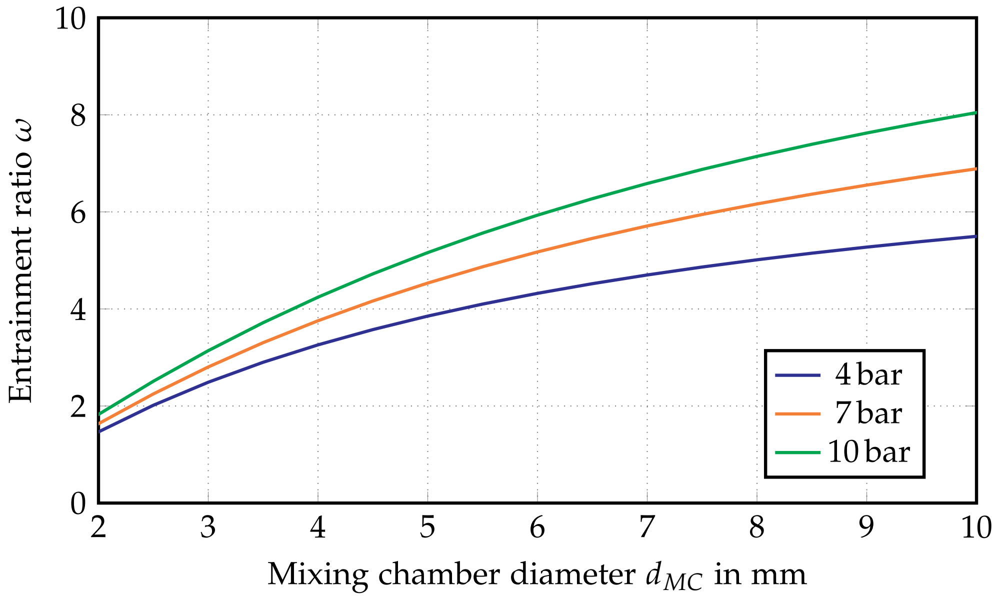

Figure 5.5: Predicted entrainment ratio by the Zhu model ([43]) with a modified n_v function (eq. 5.13).

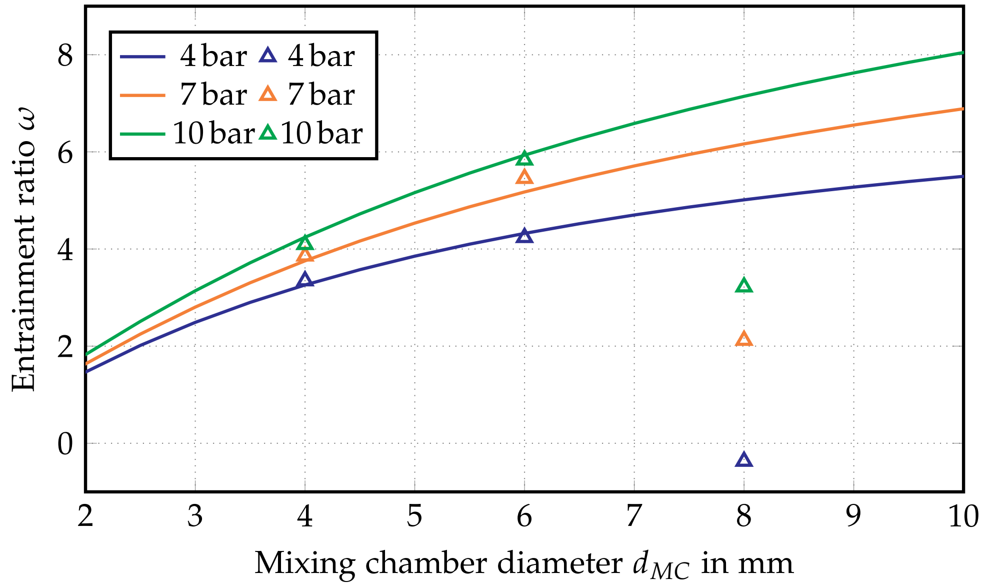

Figure 5.6: Predicted ER by the Zhu model ([43]) with a modified n_v function (eq. 5.13) compared to simulation results.

5.3 Friction loss analysis

In frictionless and adiabatic flow the stagnation pressure (see section 2.2.4) remains unchanged. In the sections of the ejector where the gas composition is homogeneous (fully mixed gas), the change in stagnation pressure along the flow path can thus be used to analyse friction losses.

The stagnation pressure p_0 along the x-Axis is evaluated on plane cuts of the ejector by calculating the mass-flow-weighted stagnation pressure over the plane. The mass flow over a cell face is calculated by multiplying the density ρ at the face by the face normal vector $\vec{f_n}$, whose magnitude is the face area, and the velocity vector $\vec{v}$ at the face. For a plane that cuts N cells the average stagnation pressure is:

$$p_0\left(x\right) = \frac{\sum_{i=1}^{N}\left(p_{0i}\,\rho_i\,\vec{f}_{ni}\cdot\vec{v}_i\right)}{\sum_{i=1}^{N}\left(\rho_i\,\vec{f}_{ni}\cdot\vec{v}_i\right)} \tag{5.14}$$

Friction losses are expected to be higher the higher the mean velocity of a flow is. For a fixed pipe diameter and a fixed mass flow, the density of the flow determines the average velocity according to the continuity equation.

$$\overline{v} = \frac{\dot{m}}{\overline{\rho}A} \tag{5.15}$$

The lowest density and thus highest velocity is obtained at a low pressure and high temperature according to the ideal gas law. Thus the loss of total pressure is also expected to be higher in these cases. Figure 5.7 shows an example of the total pressure along the primary flow path from the inlet to the nozzle exit in a CFD simulation with $\dot{m}_p = 0.182\,\mathrm{g/s}$, $p_{p0} = 4\,\mathrm{bar}$ and $T_{p0} = 783.2\,\mathrm{K}$. In the models the nozzle exit is always at $x = 0$. As can be seen, there are no significant losses in the primary pipe section, even though a relatively low pressure and high temperature were chosen. The losses in the nozzle section are discussed in section 5.4.3.

A list of the losses in total pressure for the primary, secondary and outlet pipes evaluated at various operating points, can be seen in table 5.4. Even though losses per meter are high in the primary pipe compared to the others, the absolute pressure is also at higher level. It can be said that the losses in all these cases are negligible, and the diameters of the pipes show no potential for optimization.

Table 5.4: Total pressure losses for $\dot{m}_p = 0.182\,\mathrm{g/s}$ and $\omega = 10.5$ in the primary, secondary and outlet pipe for various inlet conditions.

Section	$\mathbf{p_0}$ in bar	$\mathbf{T_0}$ in K	$\mathbf{d_{outer}}$ in mm	$\mathbf{d_{inner}}$ in mm	$\mathbf{\Delta p/l}$ in mbar/m
Primary pipe	3.8	782.30	3	-	65.65
Primary pipe	3.8	293.15	3	-	14.21
Primary pipe	20	782.30	3	-	7.69
Secondary pipe	0.95	865.00	26	4.8	0.86
Secondary pipe	0.95	782.30	26	4.8	0.68
Outlet pipe	0.95	782.30	20	-	0.23

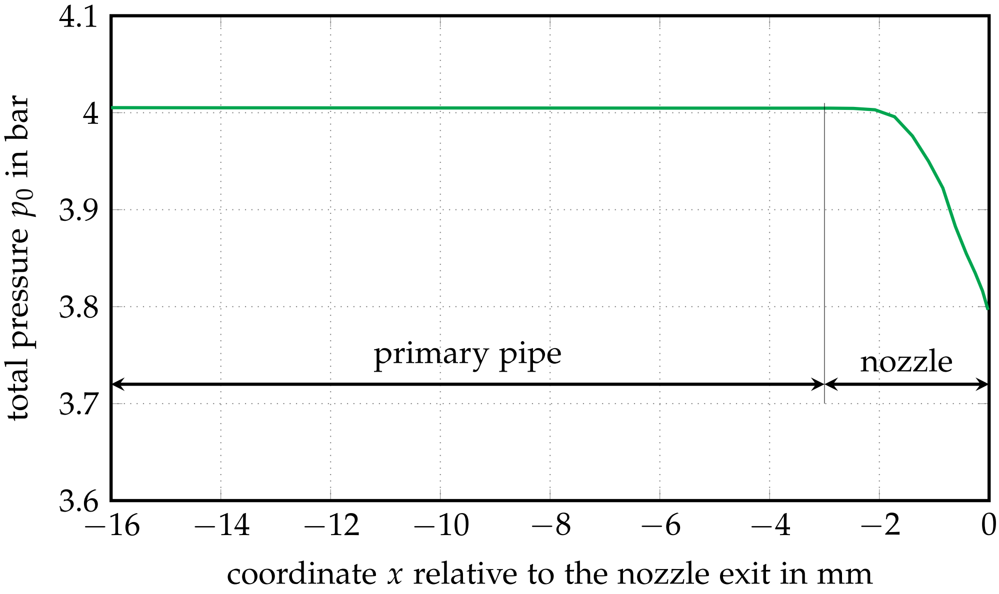

Figure 5.7: Stagnation pressure in the primary flow path for 4 bar

An exception occurs when the suction chamber length is so short that the area available to the secondary flow prior to the suction chamber is reduced and it significantly accelerates. An example of this is shown in fig. 5.8 for an ejector with $l_{SC} = 0$ (=constant area mixing), and a relatively low opening angle into the suction chamber. The losses in secondary stagnation pressure in this case are shown in fig. 5.9. Here the total pressure losses along the secondary flow path up to $x = 0$ are 2.48 mbar and are no longer insignificant. A larger opening angle α_1 (see fig. 5.1) or longer suction chamber would avoid the strong acceleration and thus help to reduce these unnecessary losses.

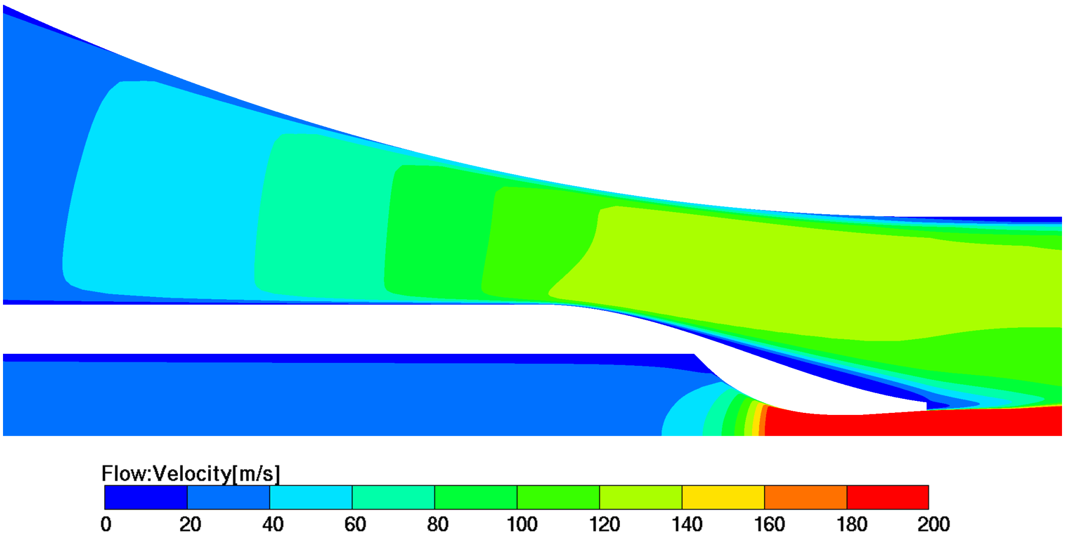

Figure 5.8: An example of a converging secondary flow path accelerating the stream in front of the suction chamber.

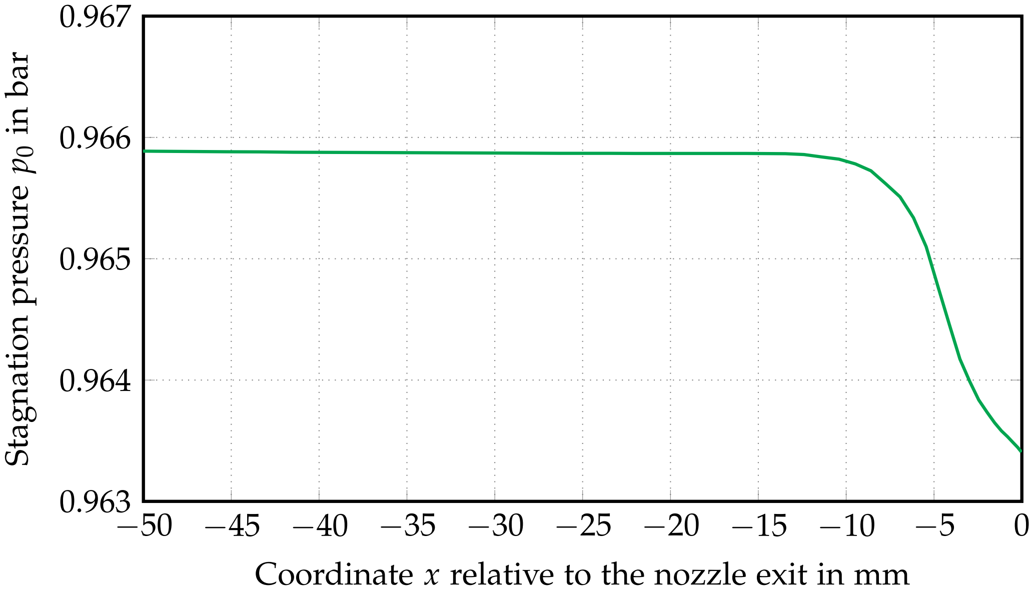

Figure 5.9: Stagnation pressure in the secondary flow path when the flow becomes significantly accelerated in front of the nozzle exit.

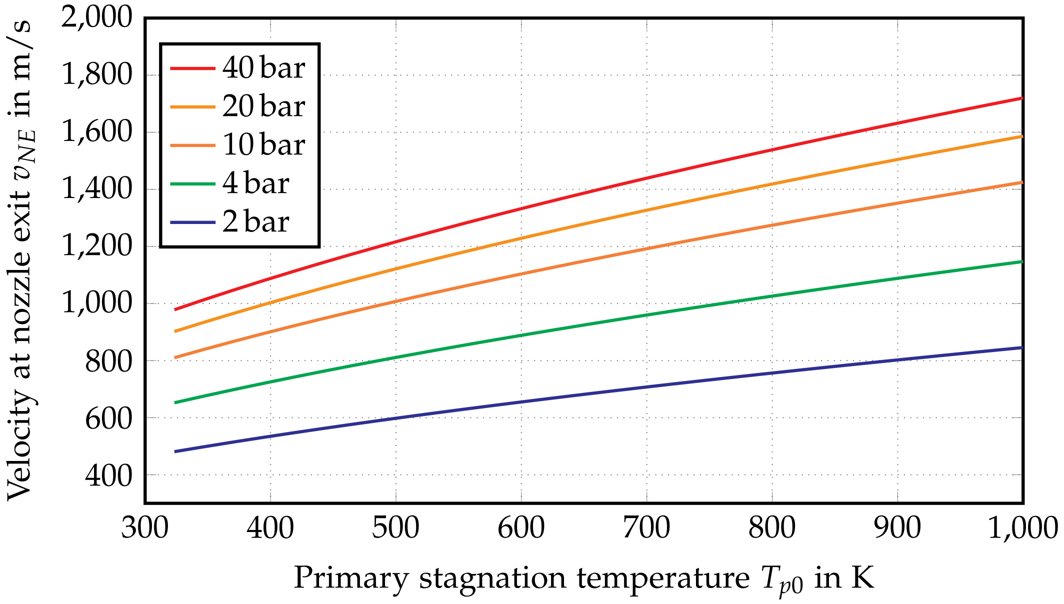

Figure 5.10: Temperature influence on the velocity at the nozzle exit for various primary stagnation pressures p_{p0}.

5.4 Parameter influence

In this section the influence of multiple parameters on the ejector performance is evaluated.

5.4.1 Primary inlet temperature

When applying the equations in section 3.5 on the nozzle for various primary stagnation temperatures and pressures, the trend in fig. 5.10 can be seen. At higher temperatures the velocity at the nozzle exit is higher. This increases the velocity of the mixed gas and leads to a higher realizable static pressure at the outlet.

To show this advantage of higher primary stream temperatures, the same ejector geometry is simulated with two different nozzles. Both nozzles are designed for a primary pressure of 3.8 bar, but for different primary temperatures, 293.15 K (*cold*) and 782.3 K (*hot*) respectively. The temperature for the *hot* case is calculated in section 3.3 for a case where it is heated by the secondary stream, thus lowering its temperature. As seen in table 5.5, the nozzle with the higher primary inlet temperature produced a 40 % higher entrainment ratio at a fixed suction pressure of 40 mbar. The two nozzles are shown in fig. 5.11. Both reach similar Mach numbers, as they expand over the same pressure ratio. The Mach number for the cold case is

Table 5.5: Comparison of two ejectors with the same primary mass flow at the same primary pressure for two different inlet temperature boundary conditions

Parameter	Name	Unit	Hot case	Cold case
Primary inlet temperature	T_{p0}	K	783.20	293.15
Secondary inlet temperature	T_{s0}	K	783.20	865.00
Primary inlet pressure	p_{p0}	bar	3.8	3.8
Secondary inlet pressure	p_{s0}	bar	0.944 1	0.944 1
Suction pressure	Δp	mbar	40	40
Entrainment ratio	ω	-	4.49	3.22

slightly higher, as the stream in the hot nozzle detached from the outer walls, but when looking at the velocity in the nozzles, the gas stream in the hot nozzle case reaches almost twice the value of the cold nozzle case. It can also be observed that the hot nozzle has a larger throat and exit diameter due to the lower density of the heated gas stream.

There are many different possibilities for how to heat the primary stream. For example, by using a counter-current heat exchanger, higher primary than secondary outlet temperatures are possible. The heat could also be supplied by the anode off-gas before the heat exchanger, or at other points in the fuel cell system with less or no influence on the secondary temperature. But for this evaluation it is assumed that the primary stream is heated by the secondary stream to thermal equilibrium as described. Thus for future simulations a primary and secondary temperature of 782.3 K is used, as it shows superior results.

5.4.2 Primary inlet pressure

Using the equations in section 3.5, the velocity at the nozzle exit can be calculated. As seen in fig. 5.12 there is a significant increase in nozzle exit velocity by increasing the pressure in the lower ranges (<10 bar), but at higher pressures the effect decreases. At higher pressures, the ideal gas law is no longer valid, and section 3.5 can not accurately predict the theoretical nozzle exit velocity.

In fig. 5.13 three different geometries are simulated with various pressures between 4 and 40 bar. In every model the suction pressure increases when the primary stagnation pressure is increased. As expected by the analysis of the nozzle exit velocity, the increase in suction pressure per pressure increment is higher, the lower the absolute value of the primary pressure is.

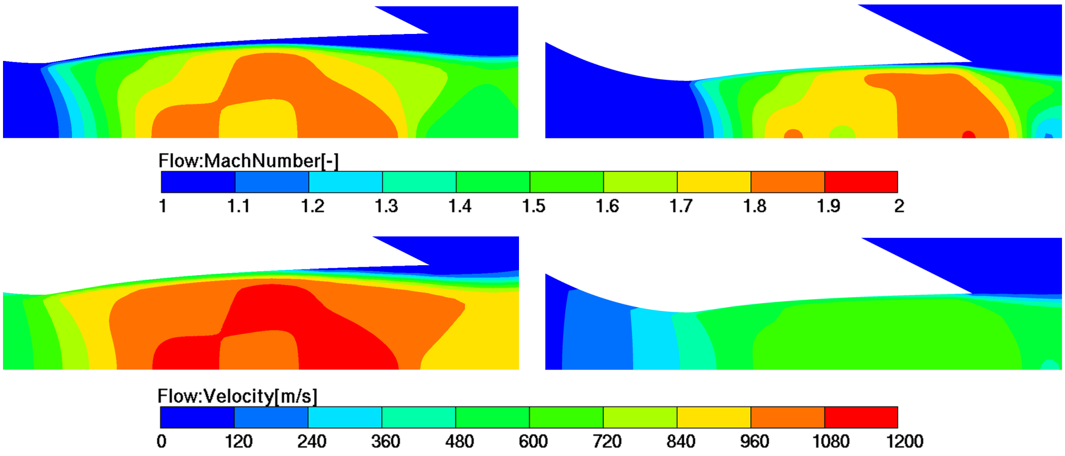

Figure 5.11: Comparison of the velocity in two *jet* style nozzles, one for hot primary gas (left) and one for cold primary gas (right) with the same primary pressure of 3.8 bar

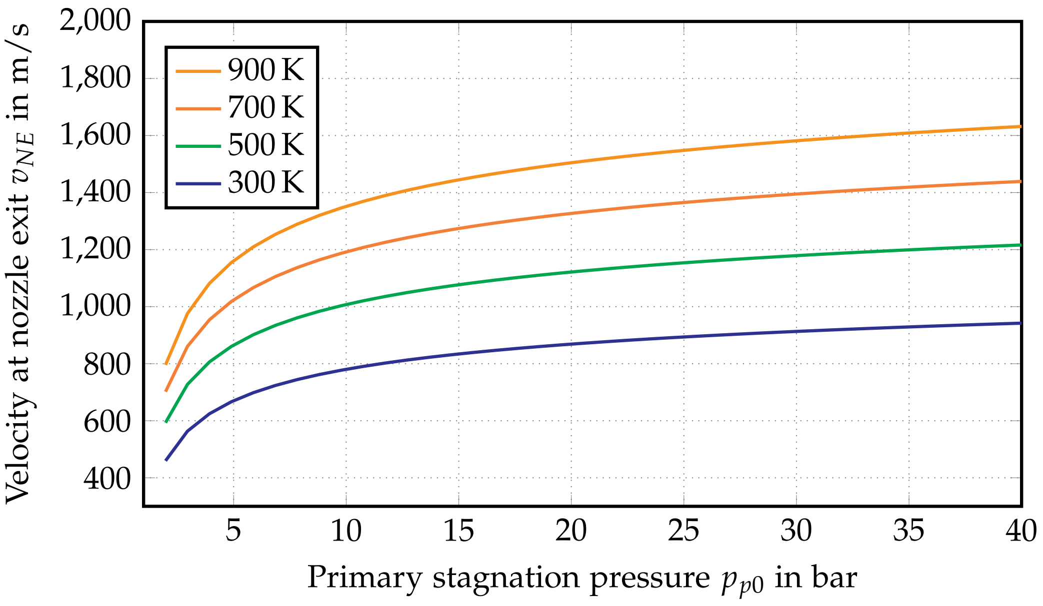

Figure 5.12: Influence of the primary stagnation pressure on the nozzle exit velocity v_{NE} at a constant nozzle exit pressure of $p_{NE} = 94410\,Pa$.

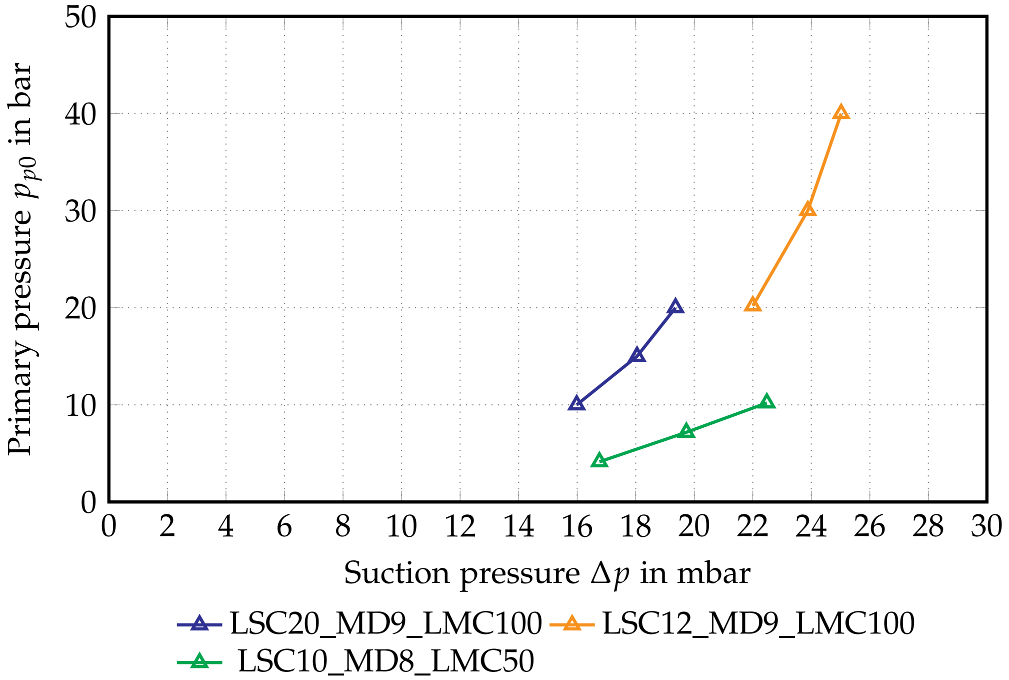

Figure 5.13: Influence of primary pressure on the suction pressure at an entrainment ratio of 10.5.

5.4.3 Nozzle geometry

Evaluation of the primary stagnation pressure in different nozzle geometries showed minor losses of primary pressure in the converging part of the nozzle and more significant losses in the diverging part as seen in fig. 5.14. In this section only the diverging geometry is discussed.

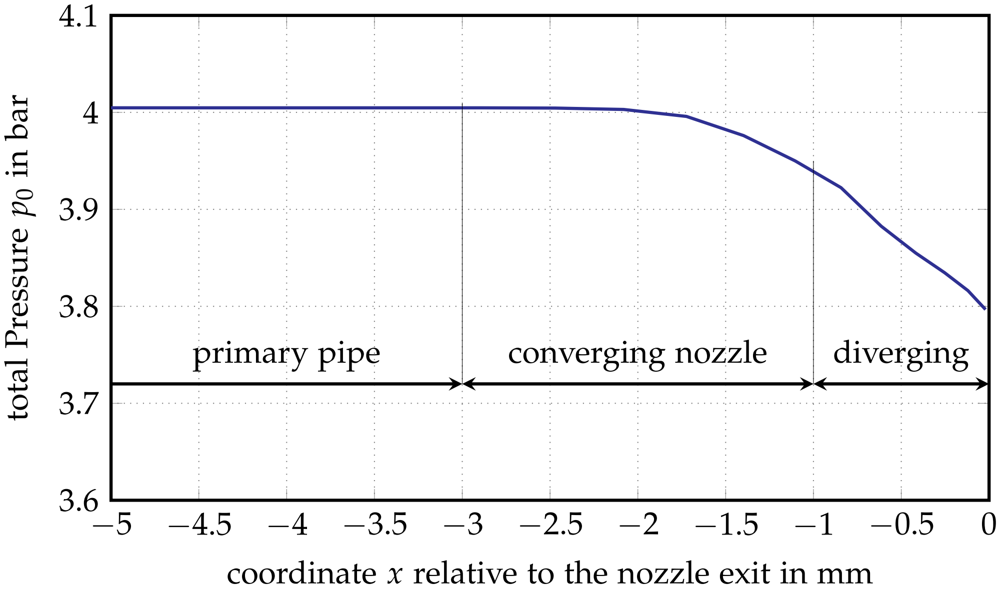

Figure 5.14: Change of total pressure in a conic nozzle for $p_{p0} = 4\,\text{bar}$.

The four key characteristics of the diverging nozzle are its throat diameter, the exit diameter, its length and the shape with which the geometry transitions between the throat and the exit. The nozzle throat links the primary mass flow to the primary pressure. If both of those values are defined for a simulation, then the throat diameter has to be computed as described in section 3.5.

The nozzle exit diameter has shown only minor influence on the ejector performance in a variation by M. Schwager [32], where conic geometries were evaluated. Overexpanded nozzles showed worse performance, as the stream separates from the walls and turbulence increases. For all the nozzles in this section, the exit diameter is calculated so that the static pressure at the nozzle exit is equal to the static pressure in the nozzle section (see section 3.5). The build up of the boundary layer in each nozzle geometry is different, which slightly changes the area available to the stream. Due to this the static pressure at the nozzle exit does not exactly equal the suction chamber pressure, but the nozzle is neither strongly over- nor underdeveloped and losses due to shock waves are assumed to be small.

The shape of the diverging section can be modelled in many different ways, three of them are shown in fig. 5.15. The conic nozzle increases in diameter by a linear function, forming a cone. The transition from the converging section to a conic diverging section is usually modelled with a radius to ensure a smoother

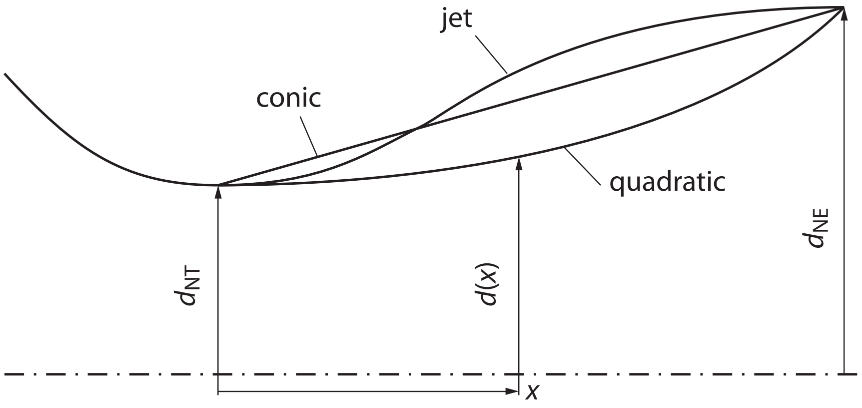

Figure 5.15: Example of different nozzle geometries.

transition. The quadratic nozzle geometry uses a quadratic function

$$d(x) = \left(\frac{x - x_{NT}}{x_{NE} - x_{NT}}\right)^2 (d_{NE} - d_{NT}) + d_{NT} \tag{5.16}$$

to define the diverging geometry. The parallel jet nozzle uses a shape that results in a parallel and uniform jet at the nozzle exit in order to minimize the energy losses in the nozzle [24]. An analytic way to design such a parallel jet nozzle was first published by K. Foelsch in 1949 [13]. The nozzle, as seen in fig. 5.16, first expands the supersonic stream in a conic section. The transition from the throat to the conic section is modelled with a radius. After the conic section a straightening section deflects the radially expanding flow into a uniform parallel flow. The length of the parallel jet nozzle is calculated so that the nozzle is as short as possible.

In table 5.6, three comparisons of different nozzle geometries are shown. When comparing two nozzles, not only the change in total pressure has to be compared, but also the influence on the total performance, as losses due to shock waves occur outside of the nozzle. In the first comparison, the parallel jet nozzle has higher losses inside of it than the conic nozzle and also results in a 1.2 % worse entrainment ratio. As seen in the pressure contours of fig. 5.17, the shock train structure is also much more pronounced in the parallel jet nozzle, leading to more losses due to shock waves. The second comparison again shows the positive effect of a higher primary temperature. While the losses inside the nozzle are 12 % higher, the entrainment ratio is increased by more than 53 %. The third comparison shows the influence of the nozzle length on two conic nozzles. The conic nozzle with $l_{ND} = 1\,\mathrm{mm}$ has 18 % less losses inside the nozzle and a 1 % higher entrainment ratio than the nozzle with $l_{ND} = 2\,\mathrm{mm}$.

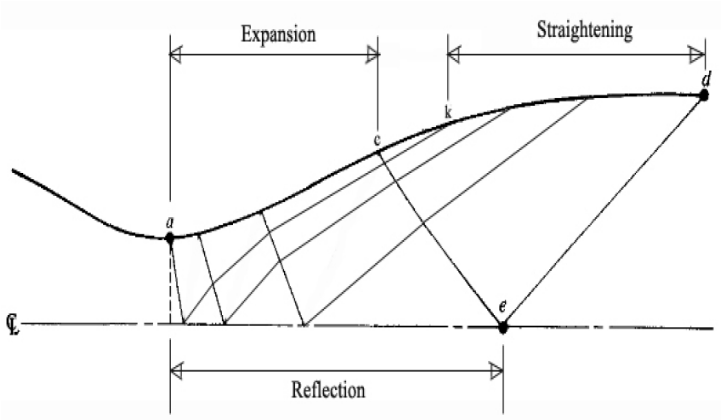

Figure 5.16: Diagram of a parallel jet nozzle from [1]. It shows the design of the parallel jet nozzle by the method of characteristics.

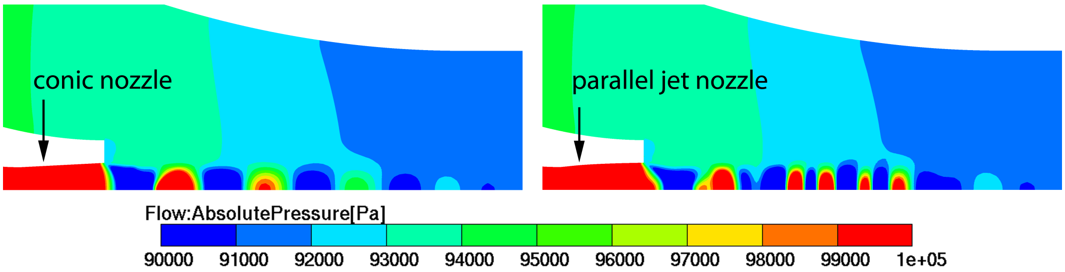

Figure 5.17: Comparison of the shock pattern in a conic nozzle and a parallel jet nozzle.

Table 5.6: Comparison of nozzle geometries. Each set of nozzles only differed by the stated parameters, but can not be compared with nozzles from other sets, as they change in multiple parameters. All simulations were done with a fixed suction pressure of 40 mbar.

Nozzle shape	$\mathbf{p_0}$ in bar	$\mathbf{T_0}$ in K	$\mathbf{l_{ND}}$ in mm	$\mathbf{\Delta p_{loss}}$ in mbar	ω -
Conic nozzle	4	782.30	1.40	234.5	4.21
Parallel Jet nozzle	4	782.30	1.40	260.4	4.16
Parallel Jet nozzle	4	293.15	1.46	385.9	2.27
Parallel Jet nozzle	4	782.30	2	435.6	3.49
Conic nozzle	4	782.30	1	224.5	3.90
Conic nozzle	4	782.30	2	272.7	3.87

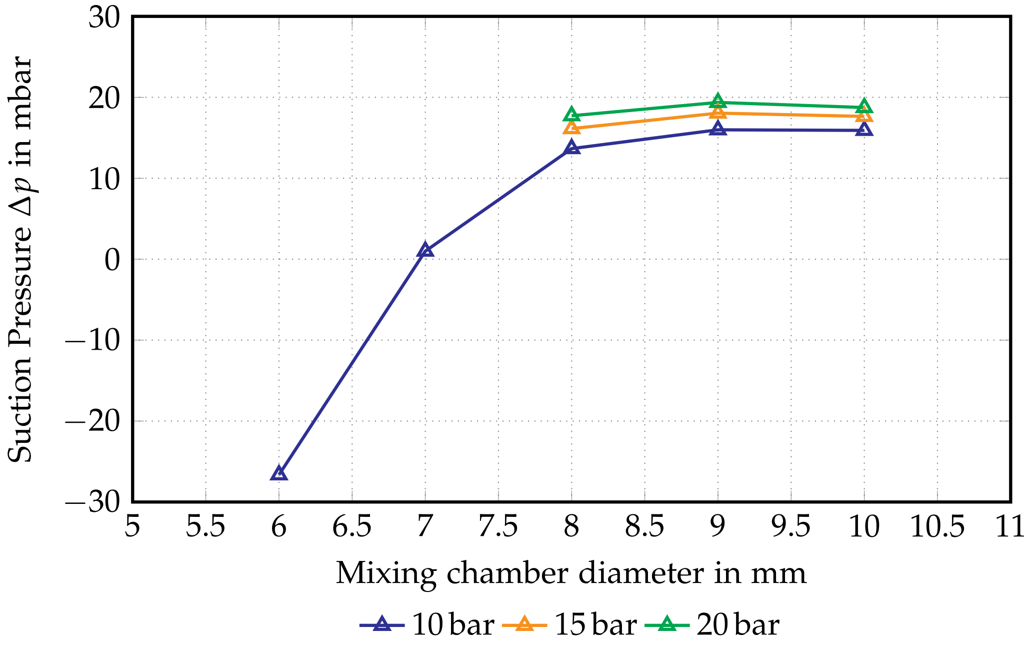

Figure 5.18: Influence of mixing chamber diameter on the suction pressure at an entrainment ratio of 10.5.

5.4.4 Mixing chamber diameter

The mixing chamber diameter determines the mean velocity of a given volume stream. In fig. 5.18, a variation of the mixing chamber diameter is performed for three different primary pressures. For the variation at 10 bar primary pressure, an increase of the mixing chamber diameter from 6 to 8 mm shows a highly positive effect on the suction pressure. From $d_m = 8$ to 9 mm, the suction pressure increases only slightly and decreases at 10 mm. This peak of the suction pressure at $d_m = 9$ mm is also visible for $p_{p0} = 15$ bar and 20 bar.

All these simulations show a flow separation in the mixing chamber, as seen in the velocity distribution in fig. 5.19. The flow separation reduces the effective area available to the mixed flow, creating a choke point or aerodynamic throat. After the choke point, the flow begins to reattach to the walls, forming an aerodynamic diffuser. The size of the flow separation increases with an increased mixing chamber diameter, as shown in fig. 5.20. But it is no indicator for the ejector performance, as the larger flow separation at $d_{MC} = 10$ mm and the smaller separation at $d_{MC} = 8$ mm both lead to a slightly worse performance compared to the $d_{MC} = 9$ mm case as seen in fig. 5.18. In fig. 5.21 the influence of the entrainment ratio on the flow separation is shown. As can be seen, the size of the flow separation

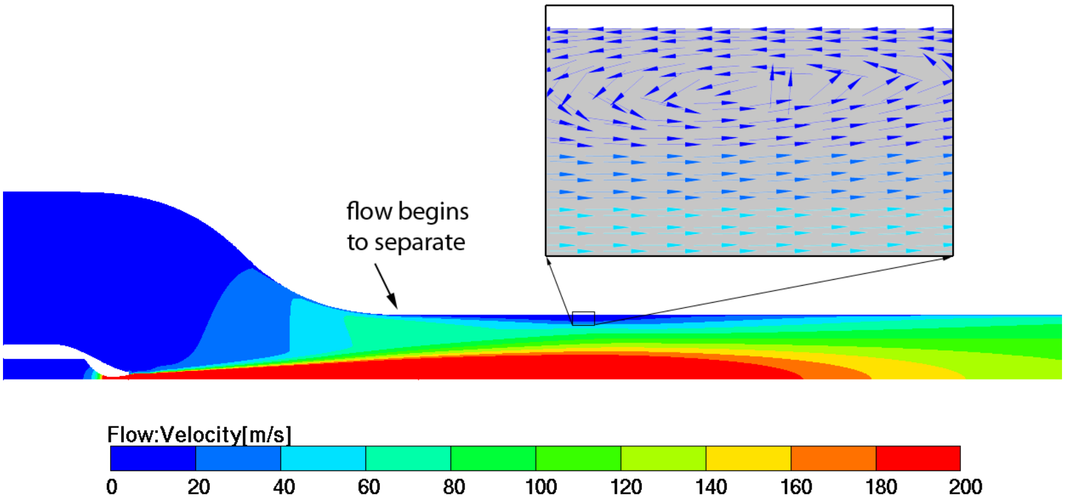

Figure 5.19: Velocity distribution in the mixing chamber, showing a flow separation. The detail shows the separation vortex with the use of equal length velocity vectors at the cell centers.

is reduced the higher the entrainment ratio and thus the volume flow is (primary mass flow is fixed in the simulations).

5.4.5 Mixing chamber length

The function of the mixing chamber is, as the name suggests, to accommodate the mixing of the two streams, so that the flow does not separate in the diffuser. The stream is mixed when the exchange of momentum is complete and the velocity profile over the radius is relatively constant in x-direction. Additionally the mixing chamber has to accommodate the shock pattern, if the mixed flow reaches supersonic velocity. Zhu [44] recommends a mixing chamber length of 5 to 8 times the mixing chamber diameter to accommodate the shock pattern. In the simulations there is only a shock pattern at the primary flow when exiting the nozzle, which is relatively short. The secondary and the mixed flow do not reach sonic velocity and thus no shocks occur. For this reason it is expected that lower values for the mixing chamber length than recommended by Zhu are feasible.

A simulation with 10 bar primary pressure and a mixing chamber diameter of 8 mm is taken as the basis for an initial investigation. The model has a relatively long mixing chamber of 100 mm in order to facilitate the evaluation of friction losses by total pressure analysis. In fig. 5.22, the mixing can be seen through the

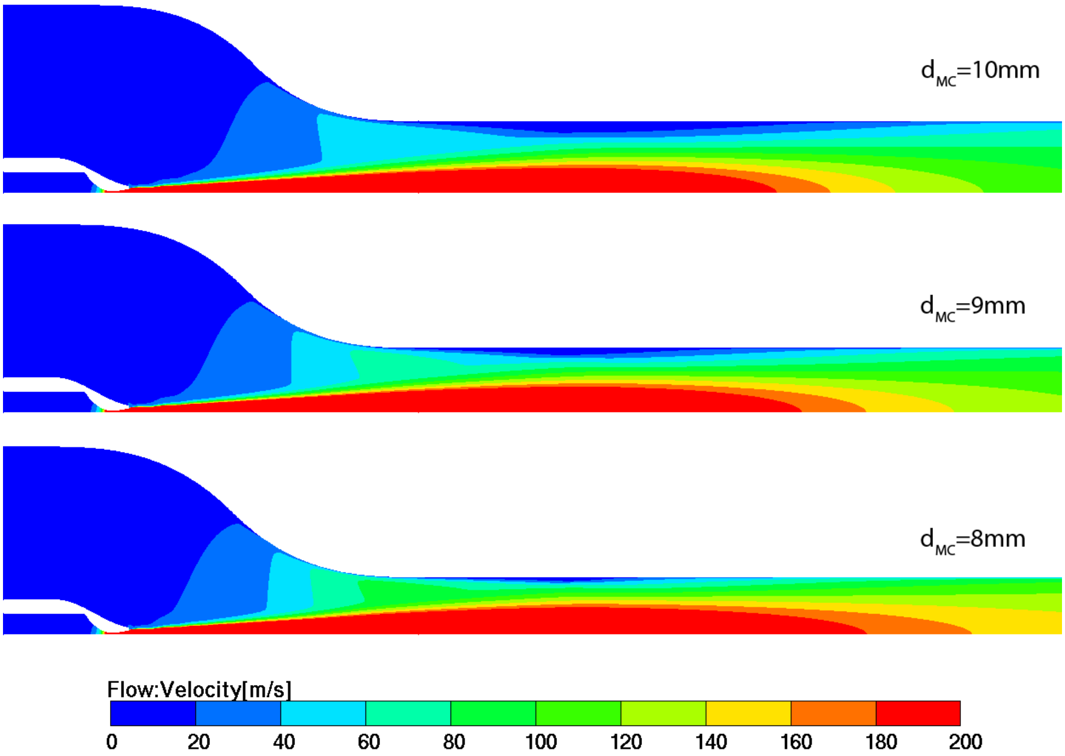

Figure 5.20: Influence of the mixing chamber diameter d_{MC} on the flow separation. Simulations at $\omega = 10.5$ and $p_p = 20\,\text{bar}$, as seen in fig. 5.18.

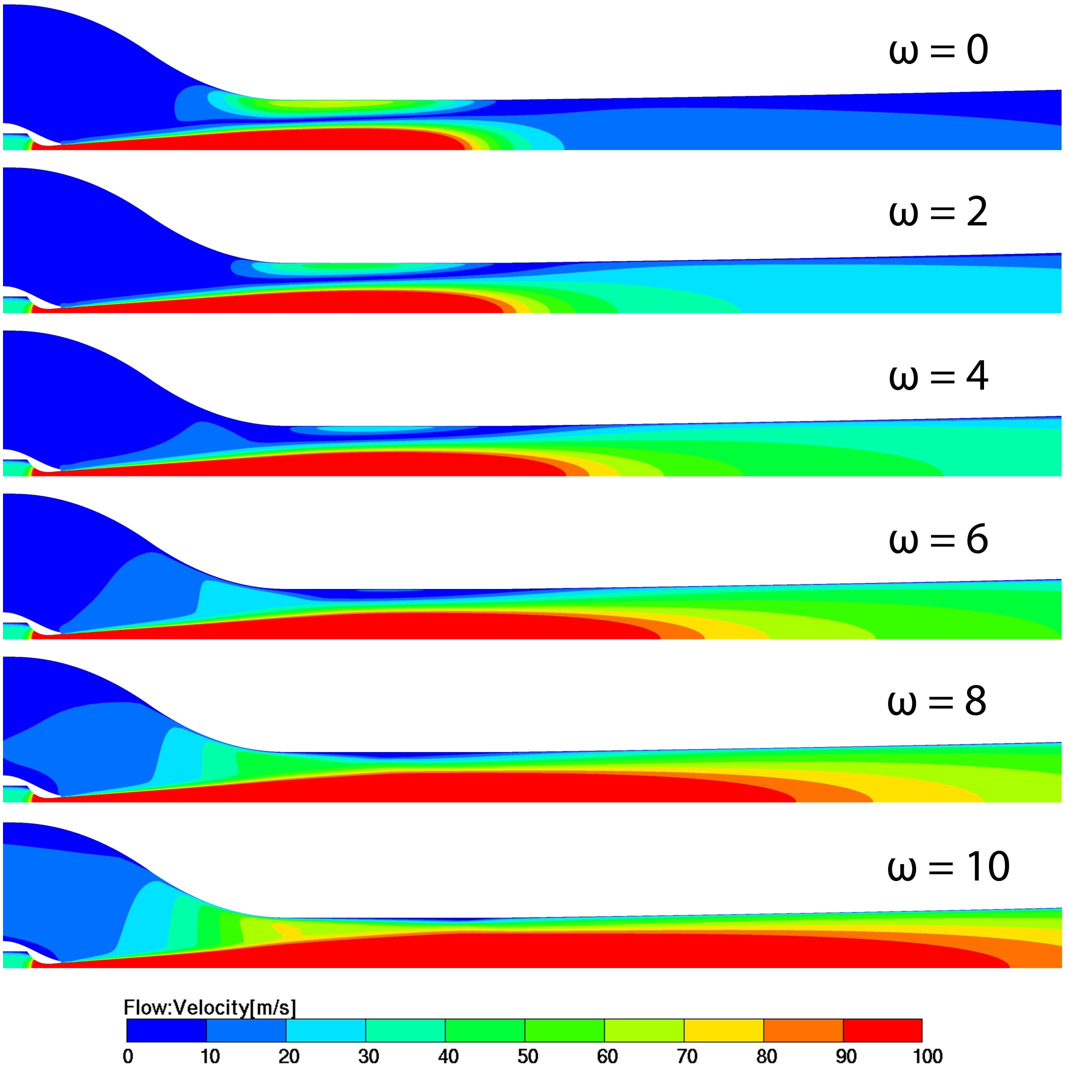

Figure 5.21: Influence of the entrainment ratio ω on the flow separation. All models use the same primary mass flow.

change in velocity, static pressure (=absolute pressure) and methane concentration. The static pressure reaches a first minimum after point (b), the end of the suction chamber. At this point the flows are not yet mixed, as can be seen by the difference in velocity and methane concentration close to the rotational axis. Between (b) and (c), the secondary stream detaches due to a free jet stream effect, the streams begin to mix chemically and the exchange in momentum increases, as the high velocity flow close to the primary stream becomes increasingly accelerated. In the choking point (c), the total mass flow has the lowest area available in the constant-area section, as the flow separation reaches its highest expansion. This point does not necessarily have to be at the same location as the vortex seen in fig. 5.19. It is more easily located by a kink in the static pressure seen in fig. 5.23. Afterwards the flow separation decreases in size and the combined flow begins to reattach to the walls. This increase in available area to the stream functions as a diffuser and is from now on referred to as *aerodynamic diffuser*. The static pressure increases until point (d), where the streams are fully mixed and the velocity profile is almost uniform. From this point on the flow scheme is referred to as Fanno flow (see section 2.2.9 and [29, chapter 9]). Fanno flow describes the compressible adiabatic flow through a constant-area duct where friction is considered. Due to the friction the stream becomes accelerated, decreases in static pressure and also total pressure. This means that the losses in total pressure, seen in fig. 5.23 between the points (d) and (e), are avoidable by reducing the length of the mixing chamber. At (e) the diffuser begins and the static pressure increases while the flow is decelerated until point (f). Between (f) and (g) is the outlet pipe, where no significant losses appear, as the mixed flow is relatively slow in this section.

The diffuser section shows significant losses in total pressure, which means that either the flow separated or that the diffuser is too long, and the friction of the high-velocity stream is the reason for the losses. As the flow did not separate in the diffuser, it can be assumed that a shorter diffuser would show superior results. Furthermore the trumpet-diffuser hardly separates in the beginning, as the area increases very slowly in this section. These diffusers have a higher chance of flow separation close to the end, as the diverging shape becomes increasingly steep. Due to the almost pipe-like section in the first third of this diffuser, it is reasonable to assume that the diffuser could begin prior to point (d) to reduce friction losses and increase the overall performance of the ejector.

To see the influence of the mixing chamber length, three shorter mixing chambers are simulated for the previously discussed model with $d_{MC} = 8\,\mathrm{mm}$. The results can be seen in fig. 5.24 and as expected, a shorter mixing chamber increases the suction pressure. Also in the model with $l_{MC} = 15\,\mathrm{mm}$, the diffuser begins prior to

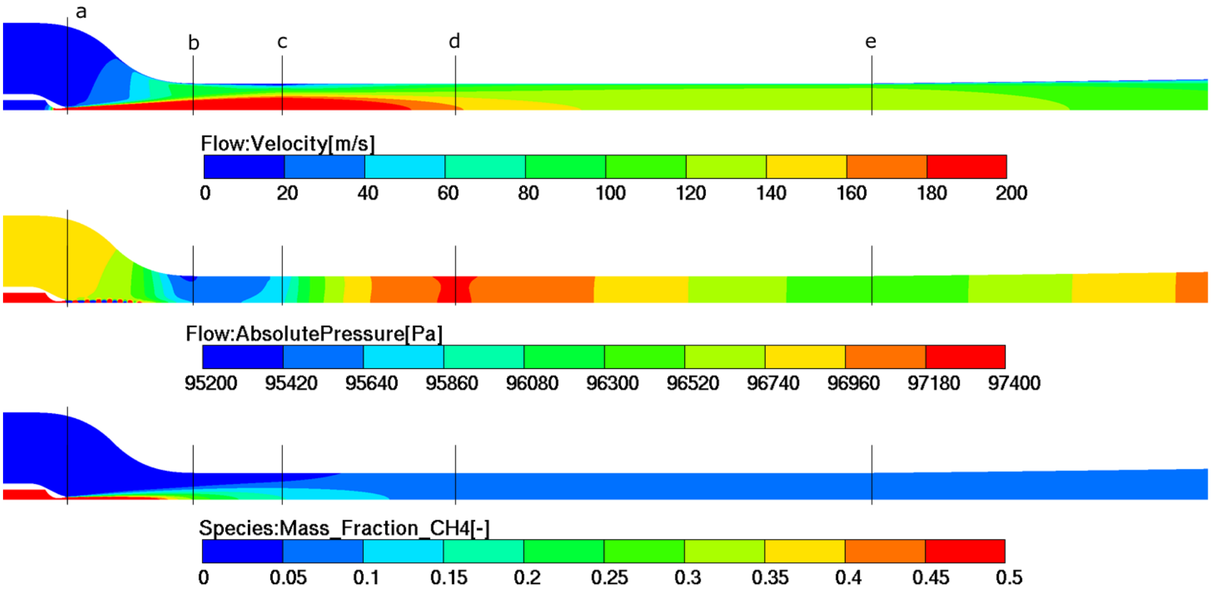

Figure 5.22: Analysis of the mixing in a model with $d_{MC} = 8\,\text{mm}$, $l_{MC} = 100\,\text{mm}$, $p_{p0} = 20\,\text{bar}$ and $\omega = 10.5$. (a) is the inlet of the suction chamber, (b) the end of the suction chamber, (c) marks the choking point, (d) the point of highest static pressure in the constant-area section and (e) the inlet of the diffuser.

(d), the end of the aerodynamic diffuser, and is still able to recover the total pressure without the flow separating inside the trumpet-diffuser. yet a shorter mixing chamber was not simulated for this case, as this would set the beginning of the diffuser close to or prior to the choking point, and other simulations had shown that this can lead to flow separation in the diffuser and does not increase the performance. An example for this is shown in fig. 5.25. In both cases, the diffuser begins prior to the choking point, and while the flow reattaches in the longer diffuser, its performance does not increase compared to ejectors where the choking point is in the constant-area section.

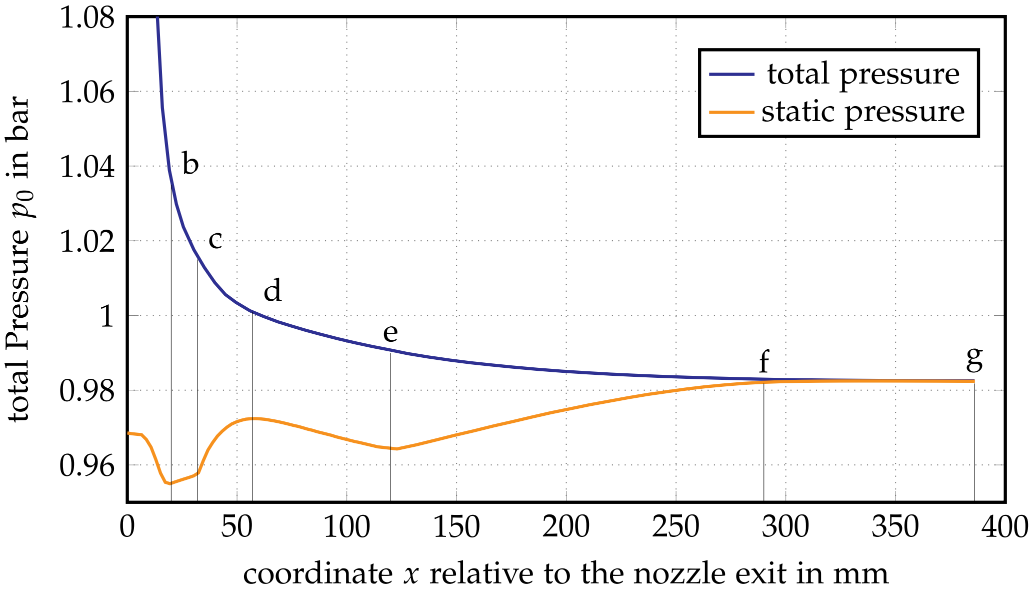

Figure 5.23: Comparison of the total pressure and the static pressure for the same case as in fig. 5.22. (b) is the end of the suction chamber, (c) marks the choking point, (d) the point of highest static pressure in the constant-area section, (e) the inlet of the diffuser, (f) the end of the diffuser and (g) the outlet.

5.4.6 Suction chamber length

Two variations of the suction chamber length are simulated for different mixing chamber lengths. The first variation is done in the same way the influence of the suction chamber length is evaluated on testbeds. There the nozzle is moved relative to the mixing chamber inlet and the influence on the entrainment ratio and suction pressure documented. The results for this first variation in fig. 5.26 show a decrease in suction pressure for larger suction chamber lengths. If the flow in the diffuser is not separated, as shown in fig. 5.25 when the nozzle exit is at the mixing chamber inlet, then the diffuser also works as intended when the nozzle is moved away from the mixing chamber inlet. This leads only to additional losses due to Fanno flow, the further the nozzle is moved away from the mixing chamber inlet.

In a second variation, the total distance of the nozzle exit to the diffuser inlet is held constant. For this the mixing chamber length is decreased when the suction chamber length is increased. The results, as seen in fig. 5.27, show only negligible change in the suction pressure when the suction chamber length is increased. The exception is when the suction chamber is so short that the secondary flow path

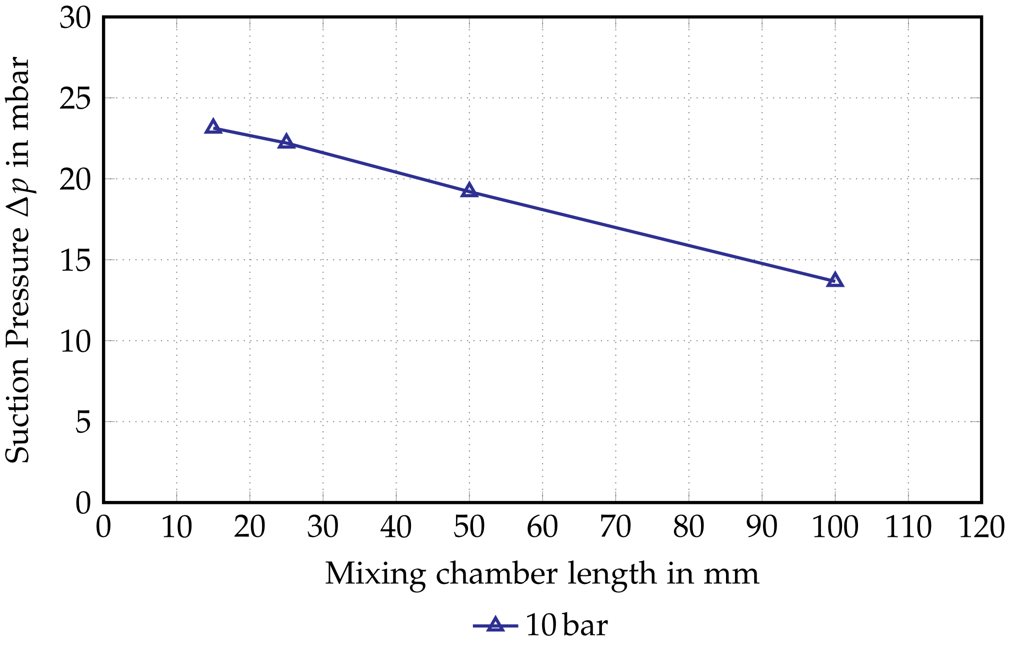

Figure 5.24: Influence of mixing chamber length on the suction pressure at an entrainment ratio of 10.5

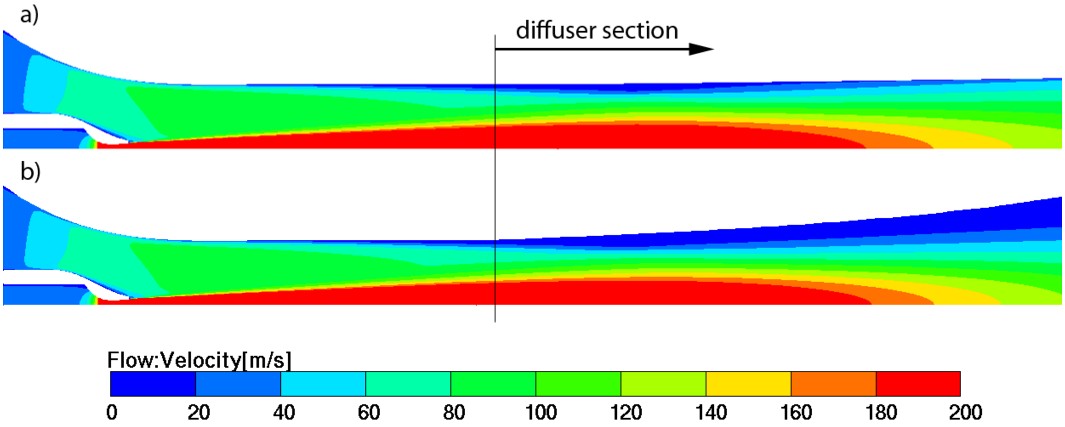

Figure 5.25: Example of diffusers starting prior to the choke point.

a) shows a 150 mm long diffuser where the flow reattaches and the suction pressure is $\Delta p = 16.81$ mbar.

b) shows a 50 mm long diffuser where the flow does not reattach and the suction pressure is $\Delta p = 8.95$ mbar.

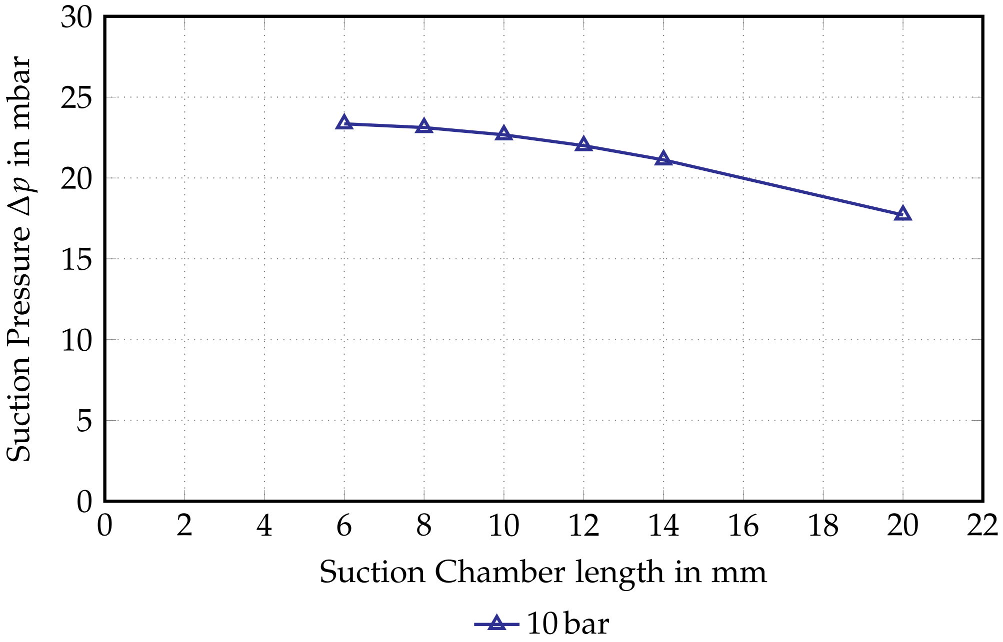

Figure 5.26: Influence of the suction chamber length on the suction pressure at an entrainment ratio of 10.5. In this variation, the length of the mixing chamber remained constant.

prior to the suction chamber is reduced in size as shown in fig. 5.28 for $l_{SC} = 0$. In these cases, the secondary flow is strongly accelerated like in a converging nozzle. This not only increases the losses due to friction, but also reduces the static pressure in the suction chamber, requiring a larger pressure recovery of the diffuser, which is always accompanied by additional losses.

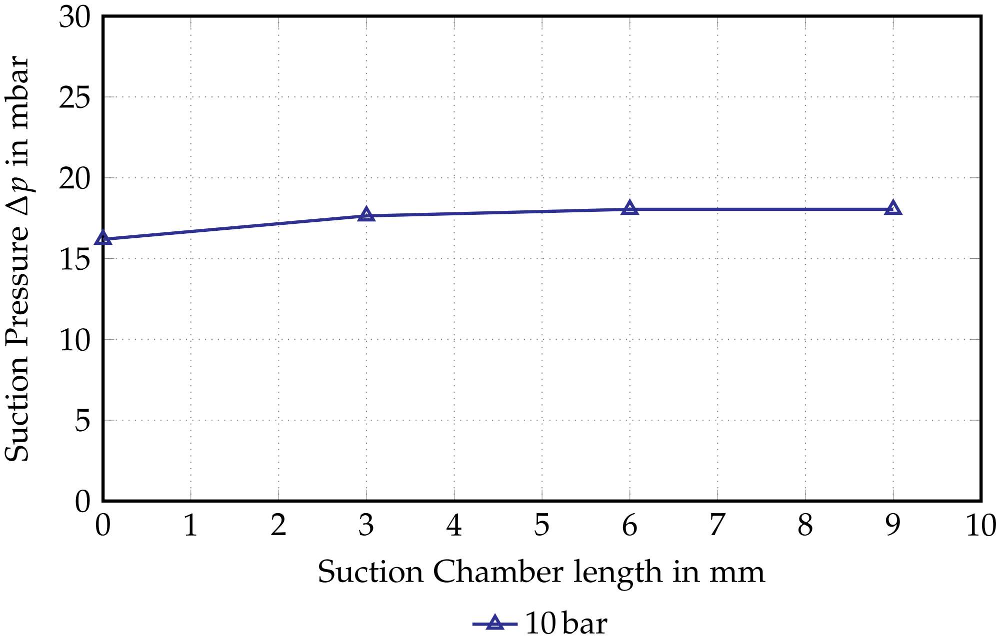

Figure 5.27: Influence of the suction chamber length on the suction pressure at an entrainment ratio of 10.5. In this variation, the distance of the nozzle exit to the diffuser inlet remained constant at 30 mm.

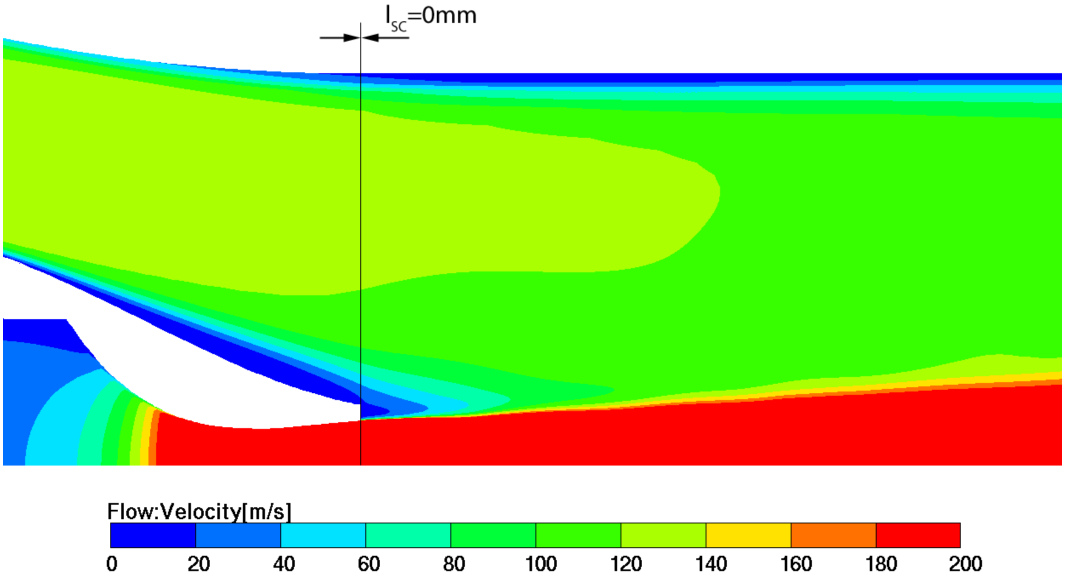

Figure 5.28: At the chosen suction chamber geometry, the secondary flow is accelerated prior to the nozzle exit when operating in constant area mode ($l_{SC} = 0$).

6 Discussion

The first part of this section contains a summary of the thesis and interpretation of the CFD results. In the second part the final optimized geometry is discussed and future potentials are evaluated.

6.1 Summary and discussion of the CFD analysis results

The goal of the AVL fuel cell department for their SOFC CHP system is to replace the blower with an ejector. For this ejector to have a similar electric power consumption, the maximum primary pressure provided by a compressor is evaluated in section 3.6 at 4 bar. The desired operating point is at a suction pressure of 40 mbar at an entrainment ratio of 10.5 (see table 3.2). Operating points at lower entrainment ratios are also possible, but this operating point is the initial goal.

CFD simulations were used to evaluate the performance of a given ejector geometry at specified thermodynamic inlet parameters. The CFD settings used for ejector simulations in AVL Fire^{TM} have been changed prior to this work, but they had not yet been validated experimentally. While previous simulation models had used a polymesh in a steady simulation, the new settings required a structured mesh and timestepping. The validation showed far better agreement to testbed results for the new settings as can be seen in fig. 4.9.

When changing the mass flow or temperature for a nozzle geometry, the resulting primary pressure changed. If this pressure should remain at a fixed value, the nozzle geometry has to be calculated by gas dynamic equations as described in section 3.5. Attempts to calculate the required geometry of the ejector in a similar way with 1-D ejector models as done in previous work at AVL failed, as ejectors designed this way showed a performance far below the required one when simulated in AVL Fire^{TM}. This can be seen in fig. 6.1, which shows the performance of the ejector that was used as the basis for the optimization simulated in the master thesis of M. Schwager [32]. This ejector is of the design B in table 4.1, where the

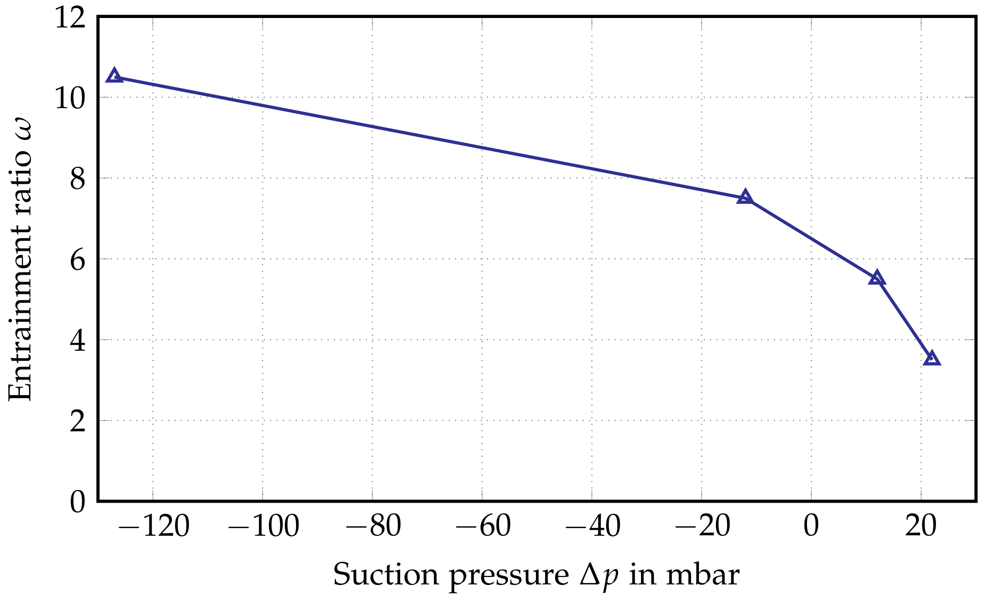

Figure 6.1: Simulation results for geometry design B in table 4.1 with a nozzle where $\dot{m}_p = 0.182\,\mathrm{g/s}$ leads to $p_{p0} = 3.8\,\mathrm{bar}$.

mixing chamber diameter of 6 mm is far too small to accommodate the volume stream.

This is because the geometry was designed with traditional 1-D models, which were made for applications where an entrainment ratio lower than unity is required (e.g. refrigeration). In these models a constant velocity distribution of the secondary flow in the mixing chamber is assumed, and often this secondary stream is calculated in a choked condition. In SOFC applications where anode gas recirculations are used, ejectors require very high entrainment ratios (ω>8) to avoid carbon deposition in the reformer. Due to this high ratio of secondary to primary stream, the velocity profile deviates strongly from the constant velocity distribution assumed in the models. This results in far lower performance values than the calculated ones when designing ejectors with traditional 1-D models by Keenan, Huang, and others. A newer model for ejectors in SOFC applications, developed by Y. Zhu [43], shows better agreement with experimental results [45]. In this model, simulation results are used to predict the influence of the primary pressure and the mixing chamber diameter. This model is applied in section 5.2 with the goal to find an ejector geometry that can reach the desired performance. The model quickly reached its limitations when it required a larger mixing chamber diameter for higher entrainment ratios, but the simulation results showed the opposite trend. A closer evaluation of the influence of each parameter was required to improve the ejector performance.

As each change of a geometry parameter requires that part of the mesh or the whole mesh is generated anew, it was necessary to find a way to speed up this process. The solution was to create a preprocessing tool in MATLAB that facilitates the mesh generation. The program calculates a nozzle geometry that leads to the required primary pressure for a given mass flow boundary condition. With this calculated geometry and the rest of the geometry defined through input data, the tool creates a cross section of the ejector geometry for AVL Fire$^{\text{TM}}$ which enables a fast mesh generation.

The parameter evaluation was performed on the thermodynamic inlet parameters of the primary stream and the main geometry parameters. An evaluation of the losses due to friction on the basis of total pressure losses showed that the inlet pipes and the outlet pipe do not need an optimization for the current geometry, as the losses are insignificant. The evaluation of the primary inlet temperature showed that an increase of the temperature leads to a significant increase in nozzle exit velocity. This increases the kinetic energy available to accelerate the secondary stream and thus the overall performance. The primary temperature can be increased through a heat exchanger which can be located at different points in the SOFC system. In this work only a temperature exchange with the secondary stream was evaluated. There the temperature equilibrium at $\omega = 10.5$ is at 782.3 K when the primary stream is initially at room temperature. For lower entrainment ratios the achievable primary temperature by such an exchange is reduced. A further increase in primary temperature is always advantageous, but an elaborate heat exchanger within the secondary flow path might increase the required suction pressure, as the pressure losses are increased.

The primary pressure always increases the nozzle exit velocity and thus also the ejector performance. It was shown that this positive effect decreases the higher the primary pressure level is. As mentioned previously, the primary pressure available is relatively low at 4 bar. An increase from $p_{p0} = 4$ bar to 10 bar in section 5.4.2 has shown a similar increase in suction pressure as one from 10 bar to 40 bar.

For the nozzle the throat and exit diameter were both calculated as described in section 3.5 to get the desired primary pressure for a given mass flow and to minimize the losses due to shock waves. The length of the diverging nozzle section was reduced to 1 mm as this increased performance. For the shape, a nozzle that leads to a parallel jet at the exit was evaluated, but was found to be inferior to conic nozzles, as the intensity of shock waves increased and thus performance decreased.

This has a positive side effect, as a parallel jet nozzle would be very difficult to manufacture compared to a conic nozzle. The nozzle is extremely small and the actual shape of a manufactured nozzle would be impossible to validate without the use of expensive x-ray or destructive measurement methods.

The analysis of the mixing chamber length showed that in all ejectors that work as intended, a flow separation on the walls occurs. This is due to the jet stream effect. The secondary stream becomes accelerated by the primary stream due to shear forces, and mass from the outer regions has to move closer to the center to satisfy the continuity equation.

At a certain distance from the nozzle exit the restricted area available to the stream due to the flow separation reaches a minimum, the choking point. It was observed that the distance of the choking point from the nozzle exit is influenced by the entrainment ratio, but it appears to be unaffected by the mixing chamber diameter or the suction chamber length. The primary pressure also showed only negligible influence on the location of the choking point, unless the primary pressure was chosen so low that the primary stream was unable to accelerate the secondary stream enough for the jet stream effect to lead to flow separation. After the choking point the stream reattaches to the walls in a section termed the *aerodynamic diffuser*, as this increase in area available to the stream has the same effect as a diffuser.

After the aerodynamic diffuser the flow is described as Fanno flow and only leads to unnecessary friction losses until the diffuser section begins. Considering this, for any ejector the mixing chamber should be as short as possible while still including the choking point. The smaller the aerodynamic diffuser section is, the earlier the diffuser can begin. It is not necessary for trumpet-diffusers to begin after the aerodynamic diffuser section, as the shape at the beginning of the diffuser is almost cylindrical and it can thus accommodate part of the aerodynamic diffuser.

The size of the flow separation is dependent on the mixing chamber diameter. The larger the mixing chamber diameter is, the larger the size of the flow separations are. Evaluation of the influence of the mixing chamber diameter on the ejector performance showed that an optimum exists for any geometry. When the diameter is chosen smaller than the optimum, the performance decreases due to friction losses of the high velocity mixed gas stream. In mixing chambers that were strongly underdimensioned, no flow separation was observed.

When varying the suction chamber length without changing the distance of the nozzle exit to the diffuser inlet, no significant influence was found. Only in cases, where the geometry of the suction chamber walls formed a converging section for the secondary flow prior to the nozzle exit, losses were observed.

6.2 Final ejector geometry and future potentials

Taking into account all the optimizations discussed previously, the Δp-ω lines for three final geometries were simulated and are shown in fig. 6.2. All geometries are equal apart from the mixing chamber diameter and the nozzle diameters. The parameter values for the model with $p_{p0} = 4\,\text{bar}$ and $d_{MC} = 8\,\text{mm}$ can be seen in table 6.1. It can be observed that the mixing chamber diameter of 8 mm performed better than $d_{MC} = 9\,\text{mm}$ in all the simulated cases. This appears to be in contradiction to the optimum at $d_{MC} = 9\,\text{mm}$ found in section 5.4.4. However, the analysis of the mixing chamber diameter in section 5.4.4 used models with a longer mixing chamber and a longer diffuser. Both lead to higher losses due to friction at smaller diameters, which lead to an optimum at a larger mixing chamber diameter.

The best ejector geometry found at $p_{p0} = 4\,\text{bar}$ and $T_{p0} = 782.3\,\text{K}$ could only achieve a suction pressure of 18 mbar at $\omega = 10.5$. This is a far lower suction pressure than the 37.69 mbar required at the operating point at $\omega = 10.5$.

This value can still be increased through further optimization of the diffuser, mixing chamber and suction chamber. Even though the suction chamber length has shown no significant influence on the ejector performance in the simulations performed, it has to be said that only minor changes in length were simulated and no extreme cases where the suction chamber is modelled so long that the mix-

Table 6.1: Key parameters of the final ejector geometry for $p_{p0} = 4\,\text{bar}$.

Parameter	Name	Value	Unit
Primary pressure	p_{p0}	4	bar
Primary temperature	T_{p0}	782.3	K
Nozzle shape	-	conic	-
Nozzle length	l_{ND}	1	mm
Suction chamber length	l_{SC}	9	mm
Mixing chamber length	l_{MC}	21	mm
Diffuser length	l_D	150	mm
Mixing chamber diameter	d_{MC}	8	mm

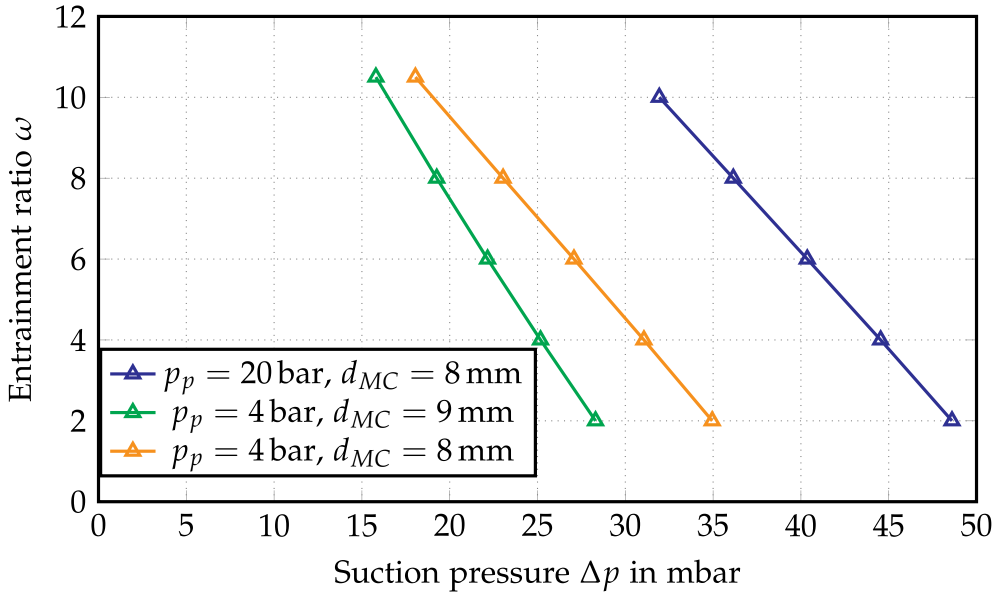

Figure 6.2: Performance of three ejector geometries with different primary pressures p_p and mixing chamber diameters d_{MC}.

ing chamber becomes obsolete were performed. It can be expected that friction losses due to high velocities close to the wall can be reduced by removing the mixing chamber and creating a shape that converges until the choke point is reached and the diffuser begins. The disadvantage of an ejector without a mixing chamber would be an inferior performance at partial load. As previously mentioned, the location of the choking point is influenced by the entrainment ratio. In partial load the change in volume flow would change the location of the choking point and result in a suboptimal angled flow into the diffuser as the aerodynamic diffuser changes its location and opening angle.

Additionally the trumpet diffuser introduced by M. Schwager [32] might not be superior to a conic diffuser in the current models. It showed far superior performance in models where the mixing chamber diameter was chosen too small, as its lower angle in the beginning is less prone to flow separation than a conic diffuser. The current models have a larger mixing chamber than the geometries evaluated by M. Schwager and flow separation could be avoided at the inlet of a conic diffuser when it is placed to be an extension of the aerodynamic diffuser. This would be advantageous, as the conic diffuser opens faster than a trumpet-diffuser of the same length, and thus the losses due to friction in the almost cylindrical section of the trumpet-diffuser could be avoided.

The nozzle itself shows only minor optimization potential. The influence of the nozzle length could be investigated in more detail, but it is not expected to yield a large performance improvement.

The primary temperature in the simulation was chosen at a relatively high level, of which it is still unclear if it can be achieved. Considering a lower primary temperature level and the low potential for optimization left, it is unlikely that an ejector geometry can be found for the operating point at $\omega = 10.5$.

According to the AVL Fuel Cell Department, alternative operating points are possible at lower entrainment ratios of at least $\omega = 8$. Such an operating point would have the added advantage of the total volume flow being lower, leading to lower velocities in the anode path and lower pressure losses. How much the required suction pressure would be lowered can not be said, as the exact values of the pressure loss in the anode path at certain volume flows are not yet known. The parameter with the most improvement potential left is the primary pressure. In fig. 6.2 it can be seen that an increase to a primary pressure of 20 bar increases the suction pressure by 12 mbar. Before the possibility of replacing the blower with an ejector can be ruled out, a closer look on the highest achievable primary pressure by a compressor system with the same power consumption as the current blower system is needed.

Even if it turns out that the ejector system can not replace the blower with the limited primary pressure available, it might still be possible to use it in an application where the pressure is available at higher values for free, e.g. automotive applications where high-pressure gas tanks are used.

Bibliography

[1] M.H. Ali et al. “Numerical Solution for the Design of Minimum length Supersonic Nozzle”. In: *Journal of Engineering and Applied Sciences* 7.5 (May 2012), pp. 605–612. ISSN: 1819-6608 (cit. on p. 74).

[2] John David Anderson and J Wendt. *Computational fluid dynamics*. Vol. 206. Springer, 1995 (cit. on pp. 10, 11).

[3] David Bischof. “Experimental Validation of an Ejector for a stationary Fuel Cell System”. MA thesis. Graz University of Technology, 2017 (cit. on pp. 2, 3, 45–47).

[4] Douglas A. Brunner et al. “Design and characterization of an electronically controlled variable flow rate ejector for fuel cell applications”. In: *International Journal of Hydrogen Energy* 37 (2012), pp. 4457–4466. ISSN: 0360-3199. DOI: `10.1016/j.ijhydene.2011.11.116` (cit. on p. 1).

[5] DR Burgess. “Thermochemical data”. In: *NIST Chemistry WebBook, NIST Standard Reference Database* 69 (2018) (cit. on p. 33).

[6] *Chemical Equilibrium Calculator*. URL: `http://grashof.engr.colostate.edu/tools/equil.html` (visited on 09/07/2018) (cit. on p. 31).

[7] Mohsen Dadvar and Ebrahim Afshari. “Analysis of design parameters in anodic recirculation system based on ejector technology for PEM fuel cells: A new approach in designing”. In: *International Journal of Hydrogen Energy* 39 (2014), pp. 12061–12073. ISSN: 0360-3199. DOI: `10.1016/j.ijhydene.2014.06.046` (cit. on pp. 26, 27).

[8] Coleman duD. Donaldson and Richard S. Snedeker. “A study of free jet impingement. Part 1. Mean properties of free and impinging jets”. In: *Journal of Fluid Mechanics* 45.2 (1971), pp. 281–319. ISSN: 0022-1120. DOI: `10.1017/s0022112071000053` (cit. on p. 16).

[9] Pierre van Eeden. “A Method for Prediction of Gas/Gas Ejector Performance”. In: *Impiantistica Italiana* (Sept. 2013) (cit. on p. 39).

[10] Maximilian Engelbracht et al. “Comparison of a fuel-driven and steam-driven ejector in solid oxide fuel cell systems with anode off-gas recirculation: Part-load behavior”. In: *Journal of Power Sources* 277 (2015), pp. 251–260. ISSN: 0378-7753. DOI: `10.1016/j.jpowsour.2014.12.009` (cit. on pp. 1, 27).

[11] J. Fabri and R. Siestrunck. “Supersonic Air Ejectors”. In: *Advances in Applied Mechanics*. Vol. 5. Elsevier, 1958, pp. 1–34. DOI: `10.1016/s0065-2156(08)70016-4` (cit. on p. 28).

[12] *Fire AST Software Documentation*. AVL List GmbH. 2018 (cit. on p. 50).

[13] Kuno Foelsch. “The Analytical Design of an Axially Symmetric Laval Nozzle for a Parallel and Uniform Jet”. In: *Journal of the Aeronautical Sciences* 16 (1949), pp. 161–166. ISSN: 1936-9956. DOI: `DOI:10.2514/8.11758` (cit. on pp. 57, 73).

[14] A. S. Hanafi et al. “1-D Mathematical Modeling and CFD Investigation on Supersonic Steam Ejector in MED-TVC”. In: *Energy Procedia* 75 (2015), pp. 3239–3252. ISSN: 1876-6102. DOI: `10.1016/j.egypro.2015.07.690` (cit. on pp. 26, 28, 50).

[15] K Hanjalić, M Popovac, and M Hadžiabdić. “A robust near-wall elliptic-relaxation eddy-viscosity turbulence model for CFD”. In: *International Journal of Heat and Fluid Flow* 25.6 (2004), pp. 1047–1051 (cit. on p. 50).

[16] B. J. Huang and J. M. Chang. “Empirical correlation for ejector design”. In: *International Journal of Refrigeration* 22 (1999), pp. 379–388. ISSN: 0140-7007. DOI: `10.1016/s0140-7007(99)00002-x` (cit. on pp. 25, 26, 28).

[17] B. J. Huang et al. “A 1-D analysis of ejector performance”. In: *International Journal of Refrigeration* 22 (1999), pp. 354–364. ISSN: 0140-7007. DOI: `10.1016/s0140-7007(99)00004-3` (cit. on pp. 25, 26, 28, 41).

[18] Rostrup-Nielsen Jens. “Mechanisms of Carbon Formation on Nickel-Containing Catalysts”. In: *Journal of Catalysis* 48 (1977), pp. 155–165. ISSN: 0021-9517. DOI: `10.1016/0021-9517(77)90087-2` (cit. on p. 31).

[19] Joseph Henry Keenan. “An investigation of ejector design by analysis and experiment”. In: *Journal of Applied Mechanics* 17 (1950), p. 299 (cit. on pp. 25, 27, 29).

[20] Strickland Landis Kneass. *Practice and Theory of the Injector*. Wiley, 1910 (cit. on p. 24).

[21] Elias Bou Lawz Ksayer. “Study and design of systems with improved energy efficiency operating with CO2 as refrigerant”. PhD thesis. École Nationale Supérieure des Mines de Paris, 2007 (cit. on p. 42).

[22] Chaqing Liao. "Gas Ejector Modeling for Design and Analysis". PhD thesis. Texas A&M University, Dec. 2008 (cit. on pp. 25, 28).

[23] Fang Liu. "Review on ejector efficiencies in various ejector systems". In: *International Refrigeration and Air Conditioning Conference*. 2014 (cit. on p. 42).

[24] H. C. Man, J. Duan, and T. M. Yue. "Design and Characteristic Analysis of Supersonic Nozzles for High Gas Pressure Laser Cutting". In: *Journal of Materials Processing Technology* 63 (1997), pp. 217–222. ISSN: 0924-0136. DOI: `10.1016/s0924-0136(96)02627-1` (cit. on p. 73).

[25] T Marynowski, P Desevaux, and Y Mercadier. "An Investigation of Ejector Design by CFD Modelling". In: *International Journal of Turbo and Jet Engines* 26.1 (2009), pp. 61–78 (cit. on p. 50).

[26] Matej Tkaucic. "CFD Simulation of an Ejector for an SOFC Cogeneration System". Master Thesis. University of Maribor, Sept. 2017 (cit. on pp. 2, 47, 54, 55).

[27] John T. Munday and David F. Bagster. "A new ejector theory applied to steam jet refrigeration". In: *Industrial & Engineering Chemistry Process Design and Development* 16.4 (1977), pp. 442–449 (cit. on p. 28).

[28] Ryan O'Hayre et al. *Fuel Cell Fundamentals*. John Wiley & Sons, 2016. DOI: `10.1002/9781119191766` (cit. on pp. 5, 6, 8).

[29] Patrick H Oosthuizen and William E Carscallen. *Introduction to Compressible Fluid Flow*. CRC press, 2013 (cit. on pp. 8–10, 13–16, 21–23, 79).

[30] Julio de Paula Peter Atkins. *Physical Chemistry, 8th ed.* 8th. W. H. Freeman, 2006. ISBN: 0716787598,9780716787594 (cit. on p. 31).

[31] Mirko Rossi. "Development of ejector based anode gas recirculation for a SOFC system". MA thesis. Università degli Studi dell'Aquila, 2017 (cit. on p. 2).

[32] Michael Schwager. "Efficiency Enhancement of Fuel Cell GPU Flow Passages by CFD-based Shape Optimization". MA thesis. Carinthia University of Applied Sciences, June 2018 (cit. on pp. 2, 3, 72, 85, 90).

[33] Subhash C Singhal and Kevin Kendall. *High-temperature solid oxide fuel cells: fundamentals, design and applications*. Elsevier, 2003 (cit. on p. 7).

[34] *Solid Oxide Fuel Cell*. URL: `https://commons.wikimedia.org/wiki/File:Solid_oxide_fuel_cell.svg` (visited on 11/06/2018) (cit. on p. 7).

[35] Da-Wen Sun and I. W. Eames. "Recent developments in the design theories and applications of ejectors". In: *Journal of the Institute of Energy* 68 (June 1995), pp. 65–79 (cit. on pp. 24, 28).

[36] Henk Kaarle Versteeg and Weeratunge Malalasekera. *An introduction to computational fluid dynamics: the finite volume method*. Pearson Education, 2007 (cit. on p. 50).

[37] Liso Vincenzo, Nielsen Mads Pagh, and Kær Søren Knudsen. "Ejector design and performance evaluation for recirculation of anode gas in a micro combined heat and power systems based on solid oxide fuel cell". In: *Applied Thermal Engineering* 54 (2013), pp. 26–34. ISSN: 1359-4311. DOI: `10.1016/j.applthermaleng.2013.01.021` (cit. on p. 8).

[38] Stefanie Wahl. "Verfahrenstechnische Optimierung und Leistungsskalierung eines Festoxid-Brennstoffzellensystems mit Hilfe multiphysikalischer Modellierung und experimenteller Daten". PhD thesis. University Stuttgart, Sept. 2015 (cit. on p. 8).

[39] *Werkstoffdatenblatt 1.4841*. URL: `https://www.dew-stahl.com/fileadmin/files/dew-stahl.com/documents/Publikationen/Werkstoffdatenblaetter/RSH/1.4841_de.pdf` (cit. on p. 31).

[40] David C Wilcox et al. *Turbulence modeling for CFD*. Vol. 2. DCW industries La Canada, CA, 1998 (cit. on p. 50).

[41] Jingzhou Yu et al. "Visualization and analysis of the characteristics of transitional underexpanded jets". In: *International Journal of Heat and Fluid Flow* 44 (2013), pp. 140–154 (cit. on pp. 16, 17).

[42] Tiejun Zhang and Michael D. Amiridis. "Hydrogen production via the direct cracking of methane over silica-supported nickel catalysts". In: *Applied Catalysis A: General* 167 (1998), pp. 161–172. ISSN: 0926-860X. DOI: `10.1016/s0926-860x(97)00143-9` (cit. on p. 31).

[43] Yinhai Zhu and Yanzhong Li. "New theoretical model for convergent nozzle ejector in the proton exchange membrane fuel cell system". In: *Journal of Power Sources* 191 (2009), pp. 510–519. ISSN: 0378-7753. DOI: `10.1016/j.jpowsour.2009.02.014` (cit. on pp. 57, 60, 61, 64, 86).

[44] Yinhai Zhu et al. "Fuel ejector design and simulation model for anodic recirculation SOFC system". In: *Journal of Power Sources* 173 (Aug. 2007), pp. 437–449. ISSN: 0378-7753. DOI: `10.1016/j.jpowsour.2007.08.036` (cit. on pp. 28, 29, 60, 76).

[45] Yinhai Zhu et al. "Numerical investigation of geometry parameters for design of high performance ejectors". In: *Applied Thermal Engineering* 29.5-6 (2009), pp. 898–905 (cit. on pp. 28, 86).

[46] Robert D Zucker and Oscar Biblarz. *Fundamentals of Gas Dynamics*. John Wiley & Sons, 2002 (cit. on pp. 8, 9, 19, 20).